DOI:10.14753/SE.2017.1972

Cell type-specific molecular anatomy of the endocannabinoid system at cortical synapses

Ph.D. thesis

Barna Dudok

Semmelweis University
János Szentágothai Doctoral School of Neurosciences

Supervisor: István Katona, DSc

Official Reviewers of the Ph.D. Dissertation: Zoltán Kisvárday, DSc
Zita Puskár, PhD

Members of the Final Examination Board: János Réthelyi, PhD
Alán Alpár, PhD
Ágnes Kittel,DSc

Budapest
2016

DOI:10.14753/SE.2017.1972

Table of Contents

DOI:10.14753/SE.2017.1972

DOI:10.14753/SE.2017.1972

List of abbreviations

- 2-AG 2-arahydonoylglycerol
- ABHD α/β-Hydrolase Domain Containing (protein)
- ACSF Artificial Cerebrospinal Fluid
- AF Alexa Fluor (a family of fluorescent dye molecules)
- BDI Bouton Distribution Index
- CA Cornu ammonis, hippocampus
- CBD Cannabidiol
- CCK Cholecystokinin
- CNS Central Nervous System
- COX Cyclooxygenase
- CV Coefficient of Variation
- Cy3 Cyanine3 (a fluorescent dye molecule)
- DMSO Dimethyl sulfoxide
- DPBS Dulbecco's Phosphate Buffered Saline
- DSI Depolarization-induced Suppression of Inhibition
- DtIN Dendritically-targeting interneuron
- EGFP Enhanced Green Fluorescent Protein
- EMCCD Electron-Multiplying Charge Coupled Device (camera)
- FAAH Fatty acid amide hydrolase
- GABA Gamma-Aminobutyric Acid
- GPCR G-protein coupled receptor
- HEK Human Embryonic Kidney (cell line)
- IgG Immunoglobulin G
- IQR Interquartile Range
- JZL JZL184, an inhibitor for monoacylglycerol lipase
- KO Knockout
- LP Localization Point
- LTD Long-Term Depression

- LTP Long-Term Potentiation
- MGL Monoacylglycerol Lipase
- NAE N-acyl-ethanolamine
- NAPE-PLD N-acyl-phosphatidylethanolamine-hydrolyzing phospholipase D
- NLP Number of Localization Points
- NMDA N-methyl-D-aspartate (type of glutamate receptor)
- PALM Photoactivated Localization Microscopy
- PB Phosphate Buffer
- PF PF3845, an inhibitor of fatty acid amide hydrolase
- PFA Paraformaldehyde
- PLC Phospholipase C
- PSD Postsynaptic density
- PSF Point Spread Function
- PtIN Perisomatically-targeting interneuron
- PV Parvalbumin
- RIM Regulating synaptic membrane exocytosis (protein)
- ROI Region of Interest
- SEM Standard error of the mean
- SIM Structured Illumination Microscopy
- SMLM Single Molecule Localization Microscopy
- SNR Signal to Noise Ratio
- SST Somatostatin
- STED Stimulated Emission Depletion Microscopy
- STORM Stochastic Optical Reconstruction Microscopy
- TBS Tris-Buffered Saline
- THC Δ^9-tetrahydrocannabinol
- TIRF Total Internal Reflection Fluorescence
- VGCC Voltage Gated Calcium Channel
- VIP Vasoactive Intestinal Polypeptide
- WT Wild Type

DOI:10.14753/SE.2017.1972

1. Introduction

The precise control of the strength of synaptic connections between neurons is the basis of the ability of the nervous system to produce adaptive, behaviorally relevant output. One of the most widespread means for synaptic depression, the negative regulation of synaptic strength, is endocannabinoid signaling. The endocannabinoid system consists of retrograde lipid messengers, most importantly 2-arachydonoyl-glycerol (2-AG) or anandamide, their respective synthetic and degradative enzymes, and cannabinoid receptors (Castillo et al. 2012). Activation of the CB_1 cannabinoid receptor leads to decreased neurotransmitter release due to the G-protein-mediated inhibition of voltage-gated Ca^{2+} channels and molecular constituents of the vesicle release machinery, and thus, CB_1 activity is an important regulator of network activity (Katona and Freund 2008). The endocannabinoid system regulates synaptic strength in a multitude of regions and cell types of the central nervous system (CNS) (Katona and Freund 2012), and its impaired function has been implicated in numerous severe pathological states, including epilepsy, neurodegenerative disorders and Fragile X mental retardation (Busquets-Garcia et al. 2013; Di Marzo et al. 2015; Katona and Freund 2008; Pacher et al. 2006; Soltesz et al. 2015). In each of the implicated pathologies, different sites of the brain circuits are involved, and thus the exact role of endocannabinoid signaling is also varied. Our general aim is to elucidate the molecular composition of endocannabinoid signaling at specific synapse populations.

Understanding molecular differences between particular cell types is required for understanding physiological and pathophysiological processes, but, in the immensely complex brain circuit, this has been an unresolved challenge for neuroscience (Lichtman and Denk 2011; O'Rourke et al. 2012). Therefore, we aimed to develop a method based on Stochastic Optical Reconstruction Microscopy (STORM) to allow cell-specific nanoscale imaging. STORM is a single molecule localization super-resolution microscopy method, capable of multichannel, 3-dimensional imaging of immunostaining at 10 nm lateral resolution (Bates et al. 2007; Huang et al. 2008b; Rust et al. 2006). While STORM has been used successfully to map the distribution of synaptic proteins in brain sections (Dani et al. 2010), existing methods did not visualize the cellular and subcellular context of the molecular localization data, and thus, did not

facilitate the cell type-specific analysis of such images. We have applied this method to resolve a paradox in endocannabinoid signaling at hippocampal GABAergic inhibitory synapses. Both perisomatically- and dendritically-targeting interneurons express presynaptic CB_1, but, for hitherto unknown reasons, synapses of the former cell type are more sensitive to cannabinoids and exhibit tonic endocannabinoid signaling, while synapses of the latter are less sensitive and don't express tonic signaling (Lee et al. 2010a; Lenkey et al. 2015).

In this chapter, I will introduce the molecular background of endocannabinoid signaling, the anatomical organization of the hippocampus and the CA1 region, the specific features of cannabinoid receptor-expressing hippocampal interneurons, and the recent advances in super-resolution microscopy methods.

1.1. Endocannabinoid signaling

1.1.1. Discovery of the endocannabinoid system

The *Cannabis sativa* plant has been used for medicinal and recreational purposes since ancient times. Its major psychoactive constituent, Δ^9-tetrahydrocannabinol (THC), was identified as early as the 1960s, however, the mode of action of this substance has remained elusive (Gaoni and Mechoulam 1964; Mechoulam et al. 1970). The discovery of the brain's endogenous cannabinoid system began with the identification of the molecular target of THC, CB_1, a G-protein coupled receptor (GPCR) of the rhodopsin family, which was found to be expressed throughout the brain at high levels (Devane et al. 1988; Herkenham et al. 1991; Herkenham et al. 1990; Matsuda et al. 1990). Soon after, endogenous ligands of CB_1 were also discovered, and, unlike most signaling molecules, endocannabinoids proved to be lipids (Devane et al. 1992; Mechoulam et al. 1995; Sugiura et al. 1995). The identification of endocannabinoids as retrograde messengers inhibiting neurotransmitter release at synapses was regarded as one of the most important discoveries in synapse research, and led to the birth of an exciting field of study (Ohno-Shosaku et al. 2001; Sudhof and Malenka 2008; Wilson and Nicoll 2001). Since then, various roles of the endocannabinoid system in the function of the central nervous system (CNS) have been uncovered, and it became evident that impairment of endocannabinoid signaling is involved in a plethora of brain disorders (Castillo et al. 2012; Katona and Freund 2012; Pacher et al. 2006). In the following

sections, I will briefly overview the molecular components of endocannabinoid signaling, and their role in controlling synapses.

1.1.2. Enzymatic pathways of the endocannabinoid system

The first endocannabinoid to be isolated from brain was N-arachidonoylethanolamine, also known as anandamide (Devane et al. 1992). Anandamide levels in the brain are two orders of magnitude lower than the concentration of 2-arachidonoylglycerol (2-AG), the second endocannabinoid discovered three years later (Sugiura et al. 1995). Anandamide and 2-AG share structural similarities, but also express fundamental differences. While both molecules contain arachidonic acid as their polyunsaturated fatty acid moiety, they have different efficacy on CB_1 (anandamide and 2-AG being partial and full agonists on CB_1, respectively), and their biosynthesis and degradation are regulated by distinct enzymatic pathways (Ahn et al. 2008). Blocking the biodegradation of both anandamide and 2-AG together mimics and occludes the physiological effect of THC, while blocking the degradation of only one mimics only some aspects of the response (Alger and Kim 2011).

Originally, cannabinoid receptors were considered as the endogenous molecular targets of anandamide, and the role of anandamide in certain forms of CB_1-mediated synaptic plasticity remains established (Ade and Lovinger 2007; Azad et al. 2003; Kim and Alger 2010; Lovinger 2007). However, after the emergence of decisive evidence for the involvement of 2-AG in numerous endocannabinoid-mediated paradigms (Tanimura et al. 2010), reports concentrate on effects through vanilloid receptors, making anandamide primarily an endovanilloid, not and endocannabinoid (Chávez et al. 2010; Grueter et al. 2010; Lee et al. 2015; van der Stelt et al. 2005). Anandamide is a member of the highly diverse family of N-acyl-ethanolamine molecules (NAEs) (Di Marzo et al. 1994; Schmid et al. 2002; Ueda et al. 2013). In the canonical pathway, these are synthesized by an N-acyl-phosphatidylethanolamine (NAPE)-hydrolyzing phospholipase D enzyme (NAPE-PLD) in a calcium-dependent manner, and degraded by fatty acid amide hydrolase (FAAH) (Cravatt et al. 2001; Cravatt et al. 1996; Okamoto et al. 2004). Interestingly, in NAPE-PLD-deficient mice, anandamide levels remain largely unchanged, while the level of long chain unsaturated (oleoyl- and

palmitoyl-) NAEs is decreased (Leung et al. 2006; Okamoto et al. 2007). These findings highlight the presence of alternative enzymatic pathways for anandamide metabolism (Rahman et al. 2014). While biochemical evidence suggests multiple synthetic routes through glycerophospho- or phospho-NAPE intermediates catalyzed by α/β-hydrolase domain containing (ABHD)-4 and glycerophosphodiesterase-1, or NAPE-phospholipase C and phospholipase B, respectively, it is not clear how these pathways contribute to brain anandamide levels (Ahn et al. 2008).

In situ hybridization against NAPE-PLD mRNA, and immunostaining against the enzyme revealed that NAPE-PLD is expressed in various populations of glutamatergic cells throughout the forebrain, with high levels in mossy fibers of granule cells of the dentate gyrus (Egertova et al. 2008; Nyilas et al. 2008). High-resolution immunogold labeling revealed that the enzyme is localized to intracellular membrane structures, resembling the cisternae of the smooth endoplasmic reticulum (Nyilas et al. 2008; Reguero et al. 2014). Presynaptic targeting of the enzyme can predict its role in anterograde signaling (Egertova et al. 2008), or in intracellular signaling within axons.

Unlike the elusive enzymatic pathways for anandamide synthesis, solid evidence supports that the major degradative enzyme of NAEs in the CNS is FAAH, as knockout (KO) mice exhibit a great increase in endogenous anandamide levels (Cravatt et al. 2001; Cravatt et al. 1996). Besides the degradation by FAAH, minor oxidative pathways catalyzed by cyclooxygenase (COX)-2, 15-lipoxygenase, and cytochrome p450 oxidases have also been described (Maccarrone et al. 2010). Oxidation of anandamide by COX-2 leads to the generation of prostamide E-2, a molecule with neuroprotective effects. FAAH was found to be expressed postsynaptically targeted to the endoplasmic reticulum, in weak association with the plasma membrane (Egertova et al. 2008; Gulyas et al. 2004). In FAAH KO mice, the proliferation of neural progenitors is increased, suggesting the role of anandamide in this process (Aguado et al. 2005).

The second major endocannabinoid, 2-AG, belongs to the family of monoacylglycerols. At least three distinct enzymes can produce 2-AG from its phosphatidylinositol bisphosphate precursor found in the lipophilic layer of the plasma membrane. The physiologically most relevant pathway is the two-step reaction catalyzed by phospholipase C (PLC) β and diacylglycerol lipase (DGL)-α, as indicated

by the abolishment of endocannabinoid-mediated synaptic plasticity in the brain of DGL-α KO mice (Bisogno et al. 2003; Gao et al. 2010; Jung et al. 2007; Tanimura et al. 2010). The synthesis of 2-AG is promoted by the activation of metabotropic ($G_{q/11}$-coupled) receptors and/or elevated intracellular calcium concentrations, leading to on-demand production of 2-AG from the precursor pool (Alger and Kim 2011; Jung et al. 2005). The receptors and enzymes required for 2-AG synthesis are precisely targeted to the perisynaptic nanodomain of synapses (termed the "perisynaptic machinery"), further indicating the direct connection between the site of production and site of effect (Katona and Freund 2008; Katona et al. 2006). However, this configuration does not explain every observation. It cannot be ruled out that multiple pools of 2-AG, or separate functional sites of DGL-α activity exist, due to some experiments showing different effects between chronic (genetic) or acute (pharmacological) blockade of synthesis, and between 2-AG release triggered by calcium or by metabotropic receptor activation (Edwards et al. 2006; Hashimotodani et al. 2005; Lerner and Kreitzer 2012; Zhang et al. 2011). Moreover, it was shown that the same synapse can release either 2-AG or anandamide contingent on the mode of metabotropic receptor activation or on stimulus protocol (Puente et al. 2011; Ramikie et al. 2014).

Alternative enzymatic pathways of 2-AG biosynthesis include DGLβ, which was shown to be important during development and immune response, but its physiological role in 2-AG production in the adult brain is not clear (Hsu et al. 2012; Williams et al. 2003). Lastly, 2-AG can be synthesized via phospholipase A and lyso-PLC enzymes, but the contribution of this pathway to brain 2-AG levels is not known (Ueda et al. 2013).

The degradation of 2-AG can occur via hydrolysis or oxygenation. Hydrolysis of 2-AG can be catalyzed by multiple enzymes, with monoacylglycerol lipase (MGL) being the most important regulator of brain 2-AG levels (Dinh et al. 2002; Taschler et al. 2011). The same reaction can also be catalyzed by ABHD6, ABHD12 and FAAH (Ahn et al. 2008). MGL was found to be expressed presynaptically, strategically positioned to terminate 2-AG signaling on CB_1 receptors, thus, MGL activity limits the duration of endocannabinoid signaling (Gulyas et al. 2004; Pan et al. 2011; Uchigashima et al. 2011). The oxidation of 2-AG, mediated by COX-2, leads to the

production of prostaglandin E_2 glycerol ester, a substance which has complementary effect on synaptic transmission compared to 2-AG. Thus, this pathway constitutes a molecular switch on the influence of endocannabinoid signaling on network activity (Katona and Freund 2012).

How lipophilic endocannabinoids can serve as messengers in the aqueous intracellular environment is a fundamental question of the field, however, lies outside the scope of this introduction. According to the general, albeit challenged view, endocannabinoids are not stored, but synthesized on demand, and degraded constitutively (Alger and Kim 2011; Min et al. 2010). Some interesting results suggest that, for anandamide at least, membrane channels and shuttle proteins regulate transport (Nicolussi and Gertsch 2015).

1.1.3. Cannabinoid receptors

The first studies identifying the receptor of psychoactive phytocannabinoids pinned down CB_1 and CB_2, G-protein coupled receptors of the rhodopsin family (Howlett et al. 1990; Matsuda et al. 1990; Munro et al. 1993). In the next decades, several receptors from all of the branches of the family were shown to be activated by phyto-, synthetic, and endocannabinoids (Brown 2007). However, the major behavioral effects of cannabinoids, also called the tetrad assay (hypolocomotion, hypothermia, analgesia, catalepsy), as well as the regulation of synapses by endocannabinoids are mediated by CB_1 (Kawamura et al. 2006; Wilson et al. 2001; Zimmer et al. 1999). Being one of the most abundant GPCRs in the brain, CB_1 is present in diverse cell- and synapse populations, and its multiple roles in the development and function of the CNS has been reviewed extensively (Alger 2012; Busquets-Garcia et al. 2015; Kano et al. 2009; Katona and Freund 2012). The involvement of CB_1 has been discovered in a number of disease conditions, such as epilepsy, addiction, mental- and neurodegenerative disorders (Di Marzo et al. 2015; Fattore 2015; Parsons and Hurd 2015; Soltesz et al. 2015; Volk and Lewis 2015). Presynaptic CB_1 receptors were first described on the axon terminals of specific hippocampal interneurons, but CB_1 expression is abundant throughout the brain, and presynaptic receptors are present on a number of cell types (Herkenham et al. 1990; Katona et al. 2001; Katona et al. 1999; Katona et al. 2006; Kawamura et al. 2006;

Uchigashima et al. 2007). While the number of receptors on an axon terminal ranges from barely detectable to several hundred between different synapse populations, CB_1-mediated synaptic plasticity is a robust physiological phenomenon throughout the brain (Heifets and Castillo 2009; Katona et al. 2006; Nyiri et al. 2005). What factors regulate the levels of presynaptic CB_1 receptors? How is the subcellular distribution of the receptor shaped, and how the abundance and positioning of receptors determine endocannabinoid-mediated signaling? Despite some emerging results, these questions remained largely elusive.

While a low level of receptors is detectable in the somatodendritic compartment of neurons, and there are functional implications for the role of somatodendritic receptors, the axonal enrichment of CB_1 is striking, especially in neurons expressing the receptor at high levels (Bacci et al. 2004; Bodor et al. 2005; Katona et al. 1999; Maroso et al. 2016). What mechanisms ensure the accumulation of CB_1 in axons and axon terminals? Synaptic proteins are often anchored to or trapped at nanodomains by specific scaffolding proteins in a highly organized manner (Choquet and Triller 2013; Südhof 2012; Tang et al. 2016). Although a cannabinoid receptor interacting protein (CRIP 1a) has been described, neither this, nor other binding partners of CB_1 were found to be required for axonal targeting of the receptor, or for phasic endocannabinoid signaling (Howlett et al. 2010; Niehaus et al. 2007; Smith et al. 2015). On the other hand, agonist-induced and constitutive internalization of the receptors emerged as major factors regulating CB_1 surface expression and distribution. Agonist application leads to rapid internalization of CB_1, followed by recycling (Coutts et al. 2001; Hsieh et al. 1999). However, the affinity of CB_1 for endocytosis appears to be different in the somatodendritic and axonal compartments, with augmented constitutive endocytosis in the somatodendritic membrane (Leterrier et al. 2006; McDonald et al. 2007). Interestingly, when CB_1 was overexpressed in cultured neurons, the striking axonal targeting was preserved irrespectively of the type of the transfected neuron, suggesting the autonomous preferential trafficking of the receptor without the presence of cell type-specific auxiliary molecules. In axon terminals, CB_1 diffusion is somewhat confined to the area of the bouton, as opposed to the free diffusion in connecting axonal segments (Mikasova et al. 2008). Brief treatment with CB_1 agonist resulted in desensitization of the receptors, coupled with exclusion from synaptic domains and decreased mobility,

which suggests the existence of some synapse- or axon terminal-specific interactions. In contrast, long-term exposure to agonists lead to loss of surface receptors in axons, accumulation of intracellular labeling, and transport to the cell body for degradation (Coutts et al. 2001; Thibault et al. 2013). Endocytosis is likely to happen in the boutons and not in the preterminal axonal segments, as also suggested by the higher relative density of receptors in the latter (Leterrier et al. 2006; Nyiri et al. 2005). Altogether, these observations suggest that CB_1 can diffuse freely in presynaptic membranes, but can probably interact with axon terminal-specific proteins.

An interesting property of CB_1 is its tonic activity. The application of antagonists/inverse agonists of CB_1 increases the release probability above baseline levels, uncovering presynaptic tonic endocannabinoid signaling (Losonczy et al. 2004; Neu et al. 2007). The existence of the CB_1 tone has been partially attributed to ambient levels of endocannabinoids (Katona and Freund 2012), and recent discoveries have shown that the molecular background of tonic and phasic endocannabinoid signaling is different (Földy et al. 2013; Lee et al. 2015). In particular, transsynaptic complexes formed by presynaptic neurexin and postsynaptic neuroligin have been shown to specifically modulate tonic endocannabinoid signaling (Anderson et al. 2015; Földy et al. 2013). In neuroligin-3 KO mice, synaptic transmission is enhanced by abolished tonic, but not phasic endocannabinoid signaling (Földy et al. 2013).

Apart from their function in regulating neuronal activity, the role of CB_1 and endocannabinoid signaling in the development of the CNS is also pivotal, regulating the proliferation, differentiation, migration and axonal growth of neurons. But these aspects are outside the scope of this chapter, and are reviewed in abundance (Gaffuri et al. 2012; Harkany et al. 2007; Harkany et al. 2008).

Among non-CB_1 cannabinoid receptors, CB_2 has been studied the most extensively. CB_2 is present on peripheral immune cells, and microglia and oligodendrocytes in the brain, and the therapeutic immune properties of cannabis are mediated through this close evolutionary relative of CB_1 (Dhopeshwarkar and Mackie 2014). Recently, convincing evidences for its neuronal expression and function have emerged (Li and Kim 2016; Stempel et al. 2016). Long-chain NAEs are known to be the endogenous ligands of peroxisome proliferator-activated nuclear receptors (PPAR-α), which are able

to regulate the excitability of neurons, and are co-expressed with NAPE-PLD in hippocampal neurons (Fu et al. 2003; Melis et al. 2008; Rivera et al. 2014). However, lipid messengers liberated in axon terminals are highly unlikely to reach nuclear receptors. Recently deorphanized GPCRs, GPR55 and GPR119 are also activated by NAEs, and GPR18 binds N-arachydonoylglycine, but, to date, very little is known about their physiological role (Godlewski et al. 2009). Endocannabinoids were shown to act on a number of targets in the brain, such as NMDA and glycine receptors, various transient receptor potential channels, T-type calcium and two-pore-domain potassium channels, but it is not known if these interactions in fact occur during physiological processes (Katona and Freund 2012).

1.1.4. Endocannabinoid-mediated synaptic plasticity

Retrograde endocannabinoid signaling acting on presynaptic CB_1 regulates neurotransmitter release in the majority of CNS synapses. In line with its widespread expression in various cell types, the downstream effectors of CB_1 signaling exhibit fundamental variability. The first example of such regulation was the discovery of depolarization-induced suppression of inhibition (DSI), a decrease in the strength of GABAergic inhibitory synapses after second-long depolarization of pyramidal cells (Pitler and Alger 1992). The link between DSI and endocannabinoids was revealed a decade later, with the demonstration of presynaptic CB_1 inhibiting voltage-gated calcium channels (VGCC) (Wilson et al. 2001; Wilson and Nicoll 2001). This inhibition occurs directly, via the βγ subunit of G proteins, and results in short-term synaptic plasticity not only in inhibitory synapses, but also excitatory synapses of the cortex and other brain areas (Castillo et al. 2012). Long-term effects of CB_1 are based on separate mechanisms, mostly the inhibition of the vesicle release machinery (Rab3B and RIM1α) via the α subunit of Gi/o proteins. This signaling is indirect, and involves the downregulation of adenylate cyclase and protein kinase A (Chevaleyre et al. 2007). Coincidently with CB_1 activation, presynaptic calcium influx and calcineurin activity are also necessary for the induction of long-term plasticity (Heifets et al. 2008). Importantly, blocking this second limb prevents LTD but leaves DSI intact, thus, molecular mechanisms of short- and long-term depression by CB_1 are indeed different. At cerebellar synapses, the downstream effect of CB_1 also involves the activation of G

protein-gated inwardly rectifying and other potassium channels, thus regulating the excitability of the presynaptic membrane (Daniel et al. 2004).

Endocannabinoid-mediated long-term depression (LTD) of excitatory or inhibitory (i-LTD) synapses can be induced with multiple protocols, including low-frequency stimulation of inputs, pharmacological activation of postsynaptic metabotropic receptors, or paired pre- and postsynaptic discharges (spike timing-dependent plasticity) with specific delays (Castillo et al. 2012). A recent study suggested that the direction of spike timing-dependent endocannabinoid-mediated depression or potentiation depends on the temporal dynamics of CB_1 activity (Cui et al. 2016). Endocannabinoid signaling does not always happen in a retrograde, homosynaptic manner. First, it is also an important player in neuron-glia interactions. In astrocytes, CB_1-induced glutamate release occurs via $G_{q/11}$ mediated signaling and rise in astrocytic calcium concentrations (Min and Nevian 2012). The resulting increase in extrasynaptic glutamate concentration could induce LTD by activating presynaptic NMDA and metabotropic glutamate receptors. Second, in inhibitory synapses, 2-AG liberated by a neighboring glutamatergic synapse can induce heterosynaptic i-LTD (Chevaleyre and Castillo 2003). Finally, postsynaptic CB_1 or CB_2 can influence the somatodendritic excitability of neurons (Bacci et al. 2004; Maroso et al. 2016; Stempel et al. 2016).

The role of endocannabinoid signaling has also been implied in metaplasticity (i.e. the plasticity of plasticity), and homeostatic plasticity. Metaplasticity has been described both as a potentiation of the magnitude of DSI after repetitive stimulation of Schaffer collaterals, or as an increased likelihood of LTP in the glutamatergic input synapses of a cell that undergone i-LTD at the GABAergic synapses (Chen et al. 2007; Chevaleyre and Castillo 2004; Edwards et al. 2008). The homeostatic regulation of GABAergic synaptic strength has been shown to occur via tonic endocannabinoid signaling mediated by ambient levels of anandamide (Kim and Alger 2010).

While KO mice lacking CB_1, DGL-α or MGL are viable, fine-tuning of synaptic strengths by endocannabinoids is important in several aspects. To conclude this chapter, I would like to highlight a few physiological and pathophysiological examples for the role of endocannabinoid signaling in brain function (Heifets and Castillo 2009). During sensory map formation, competition between inputs on neocortical principal cells

involves endocannabinoid-mediated LTD of the weakening inputs. Thus, CB_1 is required for both the reorganization following sensory deprivation, and for normal developmental map formation (Crozier et al. 2007; Deshmukh et al. 2007). The role of CB_1 in associative learning is underlined by the necessity of endocannabinoid signaling for the extinction of conditioned fear, which requires LTD in amygdala synapses, and the facilitation of fear extinction when endocannabinoid signaling is enhanced (Chhatwal et al. 2005; Lutz et al. 2015; Marsicano et al. 2002). In Parkinson's disease, reduced endocannabinoid production in the striatal medium spiny neurons of the indirect pathway contributes to increased corticostriatral excitability, and thus is an important aspect of the pathomechanism and also a therapeutic target (Kreitzer and Malenka 2007; More and Choi 2015). Endocannabinoid control of glutamatergic and GABAergic synapses is crucial for the balance of excitation and inhibition, and therefore in the pathogenesis of epilepsy (Soltesz et al. 2015). Accordingly, downregulation of CB_1 was described on excitatory, but not inhibitory synapses of human epileptic patients, and impaired endocannabinoid signaling in the lack of DGL-α leads to increased epileptogenesis in mice (Ludanyi et al. 2008; Sugaya et al. 2016). In a mouse model of Fragile X mental retardation, synaptic endocannabinoid signaling is reduced concurrent with a mismatch in the precise synaptic targeting of DGL-α at glutamatergic synapses. The change in localization manifested in mere 50 nm difference in the distance of DGL-α from synapses between healthy and impaired animals (Jung et al. 2012).

Together, these examples show that endocannabinoid signaling regulates synaptic strength in a multitude of brain regions and cell types, with considerable variability in its molecular organization and function. Gaining insight into how the involved receptors and enzymes participate in signaling at specific synapse populations thus leads to deeper understanding of the healthy and diseased brain.

1.2. Organization of the hippocampal circuit

1.2.1. Anatomical organization of the hippocampal formation

The hippocampal formation is a group of brain areas of archicortical developmental origin, formed in the medial wall of the telencephalic ventricle. It is part of the limbic system, and receives highly processed multimodal sensory input from a multitude of

brain regions, cortical and subcortical alike. It plays especially critical role in long-term memory storage and recall, as exemplified by the famous case of the patient H.M., who has developed severe memory impairment after surgical removal of the hippocampi (Squire 2009). Because the rodent hippocampus is one of the most widespread model systems of neuroscience, extensive literature is available to review its anatomy (Andersen 2007; van Strien et al. 2009). What differentiates the hippocampal formation from all other cortical brain areas is its unique organization of associational connections, resulting, in a simplified view, in unidirectional flow of information along its subregions, namely the dentate gyrus, the *sensu stricto* hippocampus, the subiculum, the pre- and parasubiculum and the entorhinal cortex. The hippocampus comprises three well-defined anatomical regions, the CA1, CA2 and CA3. While the name hippocampus, originating from the sea horse-like shape of this structure in the human brain, is commonly used to refer to the three regions together (and often including the dentate gyrus), the regions themselves are usually abbreviated CA, after *Cornu ammonis*, another historical name of the same formation. In rodents, the relative size of the hippocampus (especially the dorsal hippocampus) compared to the neocortex is especially large, due to its prominent role in spatial memory and navigation. Canonically, information flow through the hippocampus has been described as the trisynaptic circuit, in which superficial pyramidal cells of the entorhinal cortex innervate dentate granule cells through the perforant path, granule cells in turn innervate CA3 pyramidal cells via the mossy fibers, those then project to CA1 pyramidal cells through the Schaffer collaterals, and finally CA1 pyramidal cells project to the subiculum and back to the entorhinal cortex. The organization of principal cell somata in a single layer, and the strict laminar organization of inputs are also distinctive features of the hippocampus. Apart from the unidirectional trisynaptic pathway described above, the structure of the circuit is more complex, and regions of the hippocampal formation are extensively interconnected with other brain regions. First of all, the perforant path of entorhinal pyramidal cells projects directly to the CA1, also known as the temporoammonic pathway. The dentate granule cells massively innervate local interneurons, more so than CA3 pyramidal cells, and give rise to commissural afferents. The network of CA3 is characterized by the dense recurrent interconnection of its pyramidal cells, and the Schaffer collaterals also give rise to contralateral projections.

The hippocampal formation receives important subcortical, mostly modulatory input from the septum, supramamillary nucleus, locus coeruleus, ventral tegmental area and raphe, and many of these connections is reciprocal. Apart from the entorhinal and subicular cortices, CA1 pyramidal cells also innervate the retrosplenial cortex, amygdala and septum. In this study, I focus on local interneurons of the CA1, therefore in the next section I provide a brief overview of the specificities of the CA1 network.

1.2.2. Structure and connectivity in the CA1

The principal cell type of the CA1 is the pyramidal cell, probably the most studied cell type in the brain. These neurons exhibit remarkably homogenous dendritic morphology, and in rodents are organized into a single lamina of up to five cell layers thickness. Although pyramidal cells of the CA1 were originally considered a homogenous population based on their morphological uniformity, recent evidence shows the existence of several distinct populations of pyramidal cells, segregated by sublaminar localization, connectivity, neurochemical features, and transcriptome (Cembrowski et al. 2016; Lee et al. 2014; Mizuseki et al. 2011; Zeisel et al. 2015). The deepest part of the CA1, which is actually situated dorsally, due to the "upside down" position of CA1 in the brain, is the alveus, white matter containing myelinated fibers of the temporoammonic pathway. The first layer, oriens, contains basal dendrites of the pyramidal cells, and is innervated by Schaffer collaterals from the CA3. The pyramidal layer contains pyramidal cell somata, while cell bodies of interneurons can be found in every layer. The radiatum contains apical dendrites of pyramidal cells, also receiving innervation from Schaffer collaterals, and from commissural fibers of the CA3. Lastly, the most superficial lacunosum-moleculare layer, adjacent to the dentate gyrus, contains distal dendritic tufts of pyramidal cells, innervated by entorhinal afferents. The axons of CA1 pyramidal cells give local collaterals to innervate interneurons, but not other CA1 pyramidal cells, and leave the hippocampus through the alveus, projecting primarily to the subiculum.

One of the most exciting functional features of the hippocampus is its role in spatial representation. Pyramidal cells of the CA1 have unique spatial receptive fields, as, in contrast to sparse baseline firing activity, they discharge at high frequency in specific places of the environment (O'Keefe and Dostrovsky 1971). This "place cell" activity is

maintained even in the absence of Schaffer collateral input, by the perforant path alone. These findings and others highlight the function of the hippocampus and the CA1 circuit as an integrator of complex, highly processed sensory representation, exhibiting both pattern completion and pattern separation, encoding the spatial, temporal, sequence, and contextual features of events (Moser et al. 2008). Inhibition plays a fundamentally important role in these functions, by balancing excitation, maintaining and modulating rhythmic activity, tuning the firing of pyramidal cells, and filtering dendritic integration. Understanding the diverse network role of IN subtypes in the hippocampal circuit is one of the long-standing and most exciting challenges of neuroscience (Freund and Buzsaki 1996; Roux and Buzsáki 2015; Somogyi and Klausberger 2005). In the next chapter, I will briefly introduce the diversity of inhibitory interneurons of the CA1.

1.2.3. Diversity of interneurons

What defines an interneuron subtype? GABAergic interneurons, while they are ten times less numerous compared to the relatively homogenous pyramidal cells, exhibit substantial variability. This variability constitutes in their different developmental origins, specific organization of input and output synapses, molecular expression patterns, intrinsic electrophysiological properties such as discharge modes, and their characteristic firing patterns in intact circuits in vivo (Klausberger and Somogyi 2008; Markram et al. 2004). As none of these features define clear, uniform types of interneurons, classifications based on just one parameter often lead to contradictions. Nevertheless, despite the presence of many axes in the multidimensional space of diversity, specific types of interneurons are defined, and the existence of disjunctive clusters of cells can be identified based on their transcriptome (Tasic et al. 2016; Telley et al. 2016; Zeisel et al. 2015). The most striking anatomical feature of interneurons is the specialized targeting of distinct subdomains of postsynaptic pyramidal cells. Based on preferential target profiles, there are perisomatic interneurons, targeting the somata and proximal dendrites of neurons, dendritic interneurons, synapsing on the basal and apical dendrites, tuft-targeting cells, which selectively innervate the most distal segments of the dendritic tree, and axo-axonic cells, which preferentially target the axon hillock and axon initial segment. It is important to note, however, that cells belonging to

the same morphological type can be very different in every other parameter (Freund and Katona 2007).

The neurochemical classification of interneurons is based on the combinatorial expression profile of calcium binding proteins and neuropeptides, which is strongly related to the developmental origin of the cell. Cortical interneurons, unlike pyramidal cells, are not generated in the ventricular zone of the given brain area, but are produced in the ganglionic eminences at the lateral ventricle of the ventral telencephalon (Butt et al. 2005; Wonders and Anderson 2006). Typically, interneurons derived from the medial ganglionic eminence express either parvalbumin (PV) or somatostatin (SST), while neurons from the central ganglionic eminence express reelin or vasoactive intestinal polypeptide (VIP). More recently, a three-way classification based on mutually exclusive expression of PV, SST or ionotropic serotonin receptor 3A has been suggested (Lee et al. 2010b; Rudy et al. 2011). In the hippocampus, a considerable fraction of interneurons is derived from the preoptic area of the hypothalamus. Again, it has to be stressed that interneurons expressing one of these markers can show significant heterogeneity in their other parameters (Klausberger and Somogyi 2008).

During electrophysiological recordings, the most straightforward identification of an interneuron is the response it displays upon current injections. The types of discharge patterns include fast spiking (non-accommodating), bursting, regular-spiking (accommodating), irregular spiking and stuttering. Relying solely on intrinsic properties to identify neurons, however, can be misleading, as multiple subtypes can display indistinguishable electrophysiological responses (Markram et al. 2004).

Finally, the timing of interneuron firing in relation to oscillatory network activity, and the recruitment of interneuron activity by feedforward or feedback circuits are critical parameters in understanding their function in vivo. Based on the above detailed parameters, Klausberger and Somogyi in their classical work have used an immense body of accumulated knowledge to outline 21 distinct classes of GABAergic interneurons in the CA1 region (Bezaire and Soltesz 2013; Klausberger and Somogyi 2008; Somogyi and Klausberger 2005). In this study, I will focus on specific types of these interneurons, the few classes that express CB_1 cannabinoid receptors.

DOI:10.14753/SE.2017.1972

1.3. Subtypes and roles of CB_1–expressing interneurons in the CA1

1.3.1. Distinctive features of CB_1-expressing interneurons

The first evidence for the presynaptic expression of CB_1 on axon terminals came from interneurons of the CA1 region (Katona et al. 1999). These cells were containing the neuropeptide cholecystokinin (CCK), and were morphologically characterized as perisomatically targeting (also called basket cells, based on the basket-like appearance of their axon terminals enclosing pyramidal cell somata in the neocortex). Later studies identified more subtypes of CCK-positive interneurons, including VIP or vesicular glutamate transporter 3-positive cells and dendritically-targeting interneurons (Ali and Todorova 2010; Cope et al. 2002; Lee et al. 2010a; Somogyi et al. 2004). Thus, CB_1-positive cells can be divided into three morphological categories: one perisomatically targeting type (basket cells), and two dendritically-targeting types, Schaffer collateral-associated and perforant path-associated cells. Each of these morphological types express regular spiking (accommodating) firing pattern, and are often reciprocally connected through both chemical and electrical synapses. Although all CCK-positive cells express CB_1, and both markers can be used interchangeably for many purposes, it is noteworthy that not all CB_1-positive cells express CCK, and single-cell transcriptomic studies identified multiple CB_1-positive cell types (Bezaire and Soltesz 2013; Zeisel et al. 2015). Another feature of CCK/CB_1 interneurons that separates them from other interneurons is their role in integration of the excitation from multiple afferents of the hippocampus. These cells receive specific input from modulatory brainstem nuclei, and express postsynaptic receptors for serotonin and acetylcholine, and presynaptically, on their axon terminals, estrogen and GABAB receptors (Freund and Katona 2007).

The inhibition delivered by CCK/CB_1-positive cells is characterized by asynchronous GABA release. Presynaptically, they express N-type (Ca_v 2.2) calcium channels, which are loosely coupled to the vesicle release sites (Hefft and Jonas 2005). The asynchronicity of release is further aggravated by activity of CB_1 receptors (Ali and Todorova 2010).

1.3.2. Role of CB_1–expressing interneurons in network function

Although CCK/CB_1-expressing interneurons are not numerous in the CA1, they have a fundamental role in the regulation of pyramidal cell networks. During rhythmic network activity, these cells discharge at the phase of theta oscillation when place cells (pyramidal cells within their place field) fire (Klausberger et al. 2005). This pattern, together with the plasticity endowed by CB_1 expression led to the hypothesis that these cells are important in the generation of neuronal assemblies and promoting sparse coding, by effectively suppressing pyramidal cell populations, while place cells firing at higher rate can lift the inhibition from CB_1-positive interneurons via endocannabinoid signaling (Freund and Katona 2007).

Recent studies revealed that CCK/CB_1-positive interneurons are also important in regulating dendritic integration and synaptic plasticity, as well as gating excitation in pyramidal cells. Surprisingly, CCK/CB_1 cells provide by far the strongest feedforward inhibition recruited by Schaffer collateral activity, the downregulation of which is a major component of the potentiation of entorhino-hippocampal (perforant path) synapses (Basu et al. 2013). Moreover, long-range inhibitory projections from the entorhinal cortex selectively inhibit CCK/CB_1 interneurons, which underlies the gating of entorhino-hippocampal information flow (Basu et al. 2016).

1.4. Super-resolution microscopy methods

1.4.1. Principle of super-resolution microscopy

Fluorescence microscopy is one of the most widely applied methods in life sciences, due to the relative ease of use, versatile labeling modes, and potential for real-time dynamic observations. The resolution of any far-field microscope is limited by the diffraction of the rays used for imaging, photons in the case of light microscopy. This diffraction limit, often called Abbe's law, comes from the fact that imaging is the reverse of projection, and just as light cannot be focused to an infinitely small spot, the image of a very small light source can also not be infinitely small. Thus, if the size of the light source is below half the wavelength of the light, the resulting image does not depend on the size or shape of the light source, but only on some parameters of imaging, namely the wavelength of light, the refractive index of the imaging medium, and the numerical aperture of the objective. This image, called the Airy-disc, or point spread

function (PSF), is a Gaussian spot surrounded by a series of ever fading rings. As a result, light sources that are close together, cannot be separated based on their image. In other terms, the PSF is the highest spatial frequency the microscope can transmit. Due to physical limitations, glass objectives cannot resolve two neighboring point-like emitters if they are separated by less than 200 nm (Requejo-Isidro 2013; Tønnesen and Nägerl 2013). This distance is an order of magnitude larger than macromolecules, and in the size range of synapses and dendritic spines, thus, for biological applications of light microscopy, the diffraction limit was indeed a limitation, already in the time of Cajal. Electron microscopy, by using electrons instead of photons and electromagnetic lenses instead of glass, can achieve extremely high resolutions, exceeding the requirements of biological applications; however, it has its own limitations. Pre-embedding immunogold electron microscopy is able to reveal endogenous protein distribution with sufficient resolution, but it suffers from low sensitivity, and from the possibility of artefacts due to the required strong aldehyde fixation and resin embedding. High pressure freezing and replica labeling has the ability to reveal distribution with superior sensitivity and resolution, but it is limited to proteins located in randomly fractured membrane areas instead of complete anatomical profiles (Tanaka et al. 2005). Importantly, none of these methods can be applied on live, dynamic samples.

In the past decades, while the theory of the diffraction limit remained valid, multiple innovative approaches, collectively termed super-resolution microscopy, enabled fluorescence imaging with up to nanometer-scale resolution (Godin et al. 2014; Maglione and Sigrist 2013; Oddone et al. 2014; Yamanaka et al. 2014). The numerous published methods are all using one of the following three independent approaches to break the diffraction limit. The first group of methods is based on reversible saturable optical fluorescence transition, and, similarly to a confocal microscope, is using laser scanning. The most widespread variant, stimulated emission depletion microscopy (STED), works by pairing the excitation beam with a doughnut-shaped depletion beam with a non-diffraction-limited zero intensity spot at the center, to prohibit fluorescence emission from the periphery of the excitation beam, and thus, to engineer the effective excitation PSF to be smaller than dictated by diffraction (Hell and Wichmann 1994). This does not improve the imaged PSF, however, as the microscope is performing raster

scanning of one pixel at a time, it is known that the detected fluorescence is always originating from the zero intensity spot of the STED beam. The confinement of this spot is determined by laser power, thus, in biological applications, the resolution is in the range of 25-50 nm (Tam and Merino 2015). The second group of methods is called structural illumination microscopy (SIM). In this method, multiple widefield images are acquired on a camera from the same field of view, each illuminated with a different pattern. The interference fringes (Moiré pattern) in the resulting images carry high-frequency spatial information of the sample in one direction in a lower frequency, which can be resolved by the microscope. An image with increased resolution thus can be calculated from all the images taken with different directions of the illumination pattern (Gustafsson 2000). The theoretical limit of resolution improvement using SIM is twofold, practically 120 nm.

The third group of methods, single molecule localization microscopy (SMLM), is based on the temporally separated detection of light from individual emitters, and includes photoactivation localization microscopy (PALM) and stochastic optical reconstruction microscopy (STORM) (Betzig et al. 2006; Hess et al. 2006; Rust et al. 2006). These are based on the switching between non-fluorescent and fluorescent states of individual molecules, fluorescent proteins and organic dyes, respectively (Allen et al. 2013). In the present study, we have been utilizing STORM, thus, I will focus on this method in details. The limit that diffraction poses on resolution applies to the case of simultaneous imaging of multiple fluorescence emitters with spatially overlapping PSFs. The position of a single emitter, or several emitters present in a sufficiently low density, however, can be determined with great accuracy, by calculating the centroid of the PSFs. This method has been in use for single particle tracing since the 1980s (Gelles et al. 1988; Oddone et al. 2014). To exploit the precision of single molecule localization in densely labeled samples, it is necessary to control the fluorescence of emitters to maintain simultaneous emission from multiple sources at a very low density. Upon continuous illumination of the entire field of view with sufficiently high light intensity, the photoswitchable fluorophores emit photons, and, after a short time, enter a non-fluorescent state. This transformation is reversible, in contrast to photobleaching which involves irreversible oxidation of the fluorophore. After sending the fluorophores within the field of view to dark state, the stochastic return to excitable state results in the sparse

blinking of individual fluorophores, which can be recorded on a fast camera to calculate the position of each event and reconstruct the spatial distribution of the signal (Rust et al. 2006).

Although the principle of STORM does not require any special modification to the microscope or treatment of the sample to work, several improvements were necessary to make it practical for imaging biological samples. In recent applications, both the conversion of fluorophores to dark state and the return to excitable state are controlled to achieve optimal conditions. First of all, a more stable dark state is obtained by the covalent binding of a thiol group from chemicals of the special imaging medium, and irreversible photobleaching is avoided by the constant enzymatic scavenging of reactive oxygen species (Dani et al. 2010; Dempsey et al. 2009; Rust et al. 2006). Activation of fluorophores, i.e. increasing the probability to return to excitable state, is necessary to build adequate reconstruction of the sample within practically manageable time. For optimal results, oblique illumination with a laser TIRF illuminator, a sensitive electron multiplying EMCCD or scientific complementary metal–oxide–semiconductor camera, and a high numerical aperture TIRF objective has been used (Barna et al. 2016; Dani et al. 2010).

The method for activation differentiates two approaches. The original reports of STORM used activator-reporter dye pairs, that is, labeled the probes with two different dyes, one used for imaging (reporter), and one not excited during acquisition, but periodically illuminated with low-intensity light (activator). The spatial proximity of the two dyes results in the probabilistic return of the reporter to excitable state after the activator is illuminated, through a mechanism which is to date not understood. In this configuration, acquisition is performed through cycles of one activation and multiple imaging frames (Rust et al. 2006). In the second approach, known as direct STORM or dSTORM, a single dye species is activated directly, without the involvement of a dye, with higher energy (405nm) photons (Heilemann et al. 2008; van de Linde et al. 2011).

1.4.2. Multi-channel and three-dimensional STORM imaging

One of the most attractive features of fluorescence microscopy is the ease of multiplexing different labels by exploiting the specific excitation and emission wavelengths of different dyes. It is possible to perform simultaneous or sequential multi-channel imaging also with STORM using three different approaches. Firstly, when using activator-reporter dye pairs, multiple probes can be labeled with the same reporter, but different activator dyes to selectively activate each subset of probes (Bates et al. 2012; Bates et al. 2007; Shroff et al. 2008). Thus, by alternating the wavelength used for activation, blinking events detected immediately after activation can be assigned to the respective channel. The advantages of this method are that it allows simultaneous detection of multiple channels, and that it doesn't suffer from chromatic aberration. The drawback is that channel assignment is probabilistic, and thus crosstalk between channels is inevitable (Dani et al. 2010). The second approach relies on the separation of emission from different reporter dyes using optical filters, which is becoming more available as an increasing number of fluorophores are being tested for SMLM (Dempsey et al. 2011; Lehmann et al. 2015a; Lehmann et al. 2015b). This method rules out crosstalk, but doesn't allow simultaneous acquisition of channels, and introduces chromatic aberration. Finally, multi-channel imaging with spectral unmixing of different reporters allows simultaneous detection and prevents crosstalk, however, it requires splitting the emitted light and thus reduces intensity (Bates et al. 2012; Lampe et al. 2012; Zhang et al. 2015).

Thus far, I've focused on the two-dimensional resolution of microscopic images, and methods improving lateral resolution. However, the diffraction limit also applies for axial resolution, which is, in widefield microscopy, very poor. Confocal microscopy can significantly improve this by rejecting off-focus light using a pinhole in the back focal plane of the objective, but the achieved resolution is still low (>500 nm). Each of the aforementioned three domains of super-resolution microscopy have developed means to achieve super-resolution in the axial dimension too. In STORM, this is achieved exploiting astigmatism (Huang et al. 2008b). By placing a cylindrical lens in the light path at the camera port of the microscope, the image of the emitter is not affected if the emitter is located exactly at the focal plane of the objective. However, if the emitter is out of focus, the image is elongated horizontally or vertically depending on the axial

position in relation to the focal plane. After calibration with sub-resolution emitters immobilized in a monolayer on the coverslip surface, the axial position of each blinking event can be determined from the parameters of an ellipse fitted on the distorted image of the emitter. Using this method, 3D-STORM images with an axial resolution of 40 nm can be recorded from a thin volume while improvements of the method offer the imaging of larger volumes (Huang et al. 2008a; Lakadamyali et al. 2012; Min et al. 2014).

1.4.3. Determining the resolution, and visualizing STORM data

The resolution of an SMLM image is determined by two key factors: the density of detected molecules and the localization precision (Oddone et al. 2014). The precision of determining the position of a single-molecule image is not limited by the PSF of the microscope or by the pixel size of the camera. While both of these factors need to be taken into account, the accuracy of the fitting mainly depends on the number of photons detected from a blinking event. This measure of resolution, called localization precision, can be calculated analytically, but can also be determined experimentally by measuring the standard deviation of the centroids of multiple localizations of the same fluorophore. According to the Nyquist criterion of sampling, structural features smaller than the double of the distance of the nearest fluorophores cannot be resolved. Consequently, the density of detected fluorophores also contributes to the resolution of the reconstructed image. Mathematical means of providing exact numerical measures of resolution are available in the literature (Dempsey et al. 2011; Nieuwenhuizen et al. 2013; Thompson et al. 2002).

Finally, it is important to note that SMLM does not produce an image of the sample, but rather a list of coordinates of individual localization points. Therefore, the visualization of the microscopy data requires some form of rendering. The earliest publications simply used scatterplots of positions, which are accurate, but do not facilitate the intuitive interpretation of images (Rust et al. 2006). It is common in the literature to generate pixelated images where the greyscale intensity reflects the number of molecules per pixel, this method, however, sacrifices resolution at well-sampled, and introduces erroneous details in undersampled regions of the image (Baddeley et al. 2010). The molecule list can also be represented with Gaussian spots at the position of

DOI:10.14753/SE.2017.1972

each localization point, with the spread of the spot representing the localization precision of the given point. Such images represent the information content of the molecule list more faithfully, and allow the rendering of the STORM image at arbitrary zoom level (Dani et al. 2010).

DOI:10.14753/SE.2017.1972

2. Objectives

How the molecular composition of specific neurons underlies their circuit function is a fundamental question of neuroscience. However, the required integrated analysis of electrophysiological, structural and nanoscale molecular features of individual cells has been technically challenging. The CB_1 cannabinoid receptor is a major regulator of synaptic strength throughout the CNS, but the determinants of the cell type-specific variability in endocannabinoid signaling are poorly understood. Therefore in this study our specific aims are:

1) To develop a method for cell-specific molecular imaging
    - Evaluate whether STORM super-resolution imaging can be used for quantitative purposes
    - Optimize STORM for imaging CB_1 distribution in brain tissue
    - Optimize the correlated acquisition and analysis of confocal and STORM images of individually labeled neurons
2) To determine cell type-specific alterations in the molecular organization of synaptic endocannabinoid signaling
    - Compare the abundance and distribution of CB_1 between perisomatically- and dendritically-targeting interneurons
    - Compare the nanoscale organization of synaptic active zones between perisomatically- and dendritically-targeting interneurons
3) To investigate the dynamic rearrangement of CB_1 receptors in response to cannabinoid agonists
    - Determine the effect of acute elevation of endocannabinoid levels
    - Determine the effect of chronic THC treatment
    - Determine molecular basis of the dose-dependence and recovery of cannabinoid tolerance

DOI:10.14753/SE.2017.1972

3. Methods

3.1. Animals

Animal experiments were approved by the Hungarian Committee of the Scientific Ethics of Animal Research (license number: XIV-1-001/2332-4/2012), and were performed according to the Hungarian Act of Animal Care and Experimentation (1998, XXVIII, Section 243/1998, renewed in 40/2013), which are in accordance with the European Communities Council Directive of 24 November 1986 (86⁄609⁄EEC; Section 243/1998). All efforts were made to minimize pain and suffering, and to reduce the number of animals used. Perfusions for population-level STORM experiments were carried out on adult (postnatal day 50-60) male littermate $CB_1^{+/+}$ and $CB_1^{-/-}$ (kindly provided by Prof. Andreas Zimmer, University of Bonn, Germany) C57BL/6H mice (Zimmer et al. 1999). Under deep anesthesia with intraperitoneal injection of ketamine–xylazine (25 mg/ml ketamine, 5 mg/ml xylazine, 0.1% w/w pipolphen; 1 ml/100 g), mice were perfused transcardially with 0.9% saline for 2 minutes, followed by 4% paraformaldehyde (PFA) in 0.1 M phosphate buffer (PB, pH = 7.4) for 20 minutes. After perfusion, the brains were removed from the skull, cut into blocks and post-fixed in 4% PFA for 2 hours. Either 20 µm or 50 µm thick coronal sections were collected for immunofluorescence labeling or for immunogold staining, respectively, using a Leica (Nussloch, Germany) VT-1000S vibratome, and washed extensively in PB.

Acute hippocampal slice preparations were obtained from male C57BL/6N mice (postnatal day 25-40). Under deep anesthesia with isoflurane, mice were decapitated, and the brains were quickly removed and put in ice-cold high-sucrose artificial cerebrospinal fluid (ACSF; in mM, 85 NaCl, 75 sucrose, 2.5 KCl, 25 glucose, 1.25 NaH_2PO_4, 4 $MgCl_2$, 0.5 $CaCl_2$, and 24 $NaHCO_3$, equilibrated with 95% O_2 and 5% CO_2). Cutting to 300 µm was performed on a Vibratome in ice-cold oxygenated high-sucrose ACSF. After sectioning, slices were incubated in high sucrose ACSF for 60 minutes at 34°C, and then transferred to an oxygenated chamber containing ACSF (containing in mM: 126 NaCl, 2.5 KCl, 26 $NaHCO_3$, 2 $CaCl_2$, 2 $MgCl_2$, 1.25 NaH_2PO_4, and 10 glucose, equilibrated with 95% O_2 and 5% CO_2) for 60 minutes at room temperature.

3.2. Chronic drug treatment

All procedures were performed in accordance with the Italian Ministry of Health guidelines (D.L. 116/92; D.L. 111/94-B) and EEC Council Directives (219/1990 and 220/1990). Male C57BL/6J mice (postnatal day 22–31) were housed together (ten per cage), and randomly assigned to treatment groups. Individuals were identified by marking the tails daily with paint marks. Mice were injected twice daily intraperitoneally with vehicle (1% ethanol, 2% Tween 80 and saline) or THC (THC-Pharm GmbH, Frankfurt am Main, Germany) for 6.5 days. After the last injection, mice were allowed to recover according to the experiment (24 hours to 6 weeks), and then sacrificed to prepare acute hippocampal slices as described above.

3.3. Patch-clamp recording

Electrophysiological recordings from pyramidal cells and interneurons were carried out at 33°C in oxygenated ACSF. A fixed stage microscope (Eclipse FN1, Nikon, Tokyo, Japan) equipped with infrared differential interference contrast optics and micromanipulators (Luigs & Neumann, Ratingen, Germany) was used to visualize and approach the cells with borosilicate glass micropipettes (3–4 MΩ) filled with internal solution containing 0.2% biocytin, and (in mM) 126 K-gluconate, 4 KCl, 10 HEPES, 4 ATP-Mg, 0.3 GTP-Na, 10 phosphocreatine, pH 7.2, 270–290 mOsm. Pyramidal cells and interneurons located in the pyramidal and radiatum layers of CA1, respectively, were recorded in whole-cell patch-clamp configuration. Traces were recorded using MultiClamp700B amplifiers (Molecular Devices, Sunnyvale, USA). Signals were filtered at 3 kHz using a Bessel filter and digitized at 10 kHz with a Digidata 1440A analog–digital interface (Molecular Devices). The resting membrane potential was measured in current-clamp mode, and then the response of the cell to current steps (from -200 to 300 in 50 pA increments, 1s) was recorded. Then, cells were clamped to -70 mV for 10-30 minutes to allow axonal labeling with biocytin. Series resistances were carefully monitored, and the recordings were discarded if the series resistance changed > 20% or reached 20 MΩ. The recorded traces were analyzed using the Clampfit 10.2 software (Molecular Devices). After recording, the sections were transferred into 4% PFA in PB, and fixed for 40 hours at 4°C.

3.4. Cell culture

HEK293 cells were maintained in cell culture treated T25 flasks in Dulbecco's modified Eagle's medium containing 25 mM D-glucose and 10 % heat-inactivated neonatal calf serum at 37 °C and 5 % CO_2. For transfection with the construct coding N-terminally EGFP-tagged CB_1 (Tappe-Theodor et al. 2007), the cells were split onto poly-D-lysine (20 μg/ml) coated glass-bottom petri dishes. (Ibidi, Martinsried, Germany). Transfection was performed using 1 μg of plasmid DNA and 1 μl Lipofectamine 2000 (Invitrogen, Carlsbad, USA) per dish, according to manufacturer's instructions. Dishes were returned to 37 °C and 5 % CO_2 for 18 hours to allow the expression of the construct. After incubation, cells were fixed in 4 % paraformaldehyde for 15 minutes.

3.5. Immunostaining

Immunostaining in this study was used to label HEK cells and brain slices for confocal microscopy and STORM. All tissue samples were stained free-floating, in 24-well tissue culture dishes, and incubations were at room temperature on an orbital shaker unless stated otherwise. The primary and secondary antibodies used throughout the study are listed in Table 1 and Table 2, respectively.

Table 1: Primary antibodies utilized in the study

Antigen	Host species	Dilution	Catalogue number or reference
Bassoon	Mouse	1:2000	Ab82958, Abcam (Cambridge, UK)
CB_1	Guinea pig	1:1000	Gift of M. Watanabe (Hokkaido, Japan) (Fukudome et al. 2004)
CB_1	Rabbit	1 μg/ml	ImmunoGenes Kft (Budakeszi, Hungary) (Dudok et al. 2015)
CCK	Mouse	1:3000	#9303, CURE (Los Angeles, USA)
EGFP	Mouse	1:1000	MAB3580, Millipore (Darmstadt, Germany)

Custom-labeled secondary antibodies were prepared from unlabeled antibodies listed in Table 2. Amino-reactive succinimidyl ester derivatives of dyes AF405 and AF647 were purchased from Molecular Probes (Carlsbad, USA), and Cy3 from GE Healthcare (Little Chalfont, UK), and dissolved in DMSO at 0.2 mg/ml. Antibodies (50 µl) and dyes (one activator: AF405, 4 µl or Cy3, 1.5 µl; and reporter (AF647, 0.6 µl) were mixed in a tube, and 6 µl of 1M $NaHCO_3$ was added to start the reaction. After 30 minutes of incubation at room temperature, 140 µl of DPBS was added to stop the reaction, and the mixture was filtered through Sephadex G-25 size exclusion chromatography columns (GE Healthcare). The first 550 µl of elution was discarded, and the next 300 µl was collected. The antibody concentration and the labeling ratio were determined using a spectrophotometer (SmartSpec Plus, Bio-Rad, Hercules, USA).

Table 2: Secondary antibodies utilized in the study

Target species	Host species	Label	Dilution	Catalogue number
Guinea pig	Donkey	Custom Cy3 + AF647	2 µg/ml	706-005-148, Jackson ImmunoResearch (West Grove, USA)
Mouse	Donkey	Custom AF405 + AF647	2 µg/ml	715-005-150, Jackson
Rabbit	Donkey	Custom Cy3 + AF647	2 µg/ml	711-005-152, Jackson
Mouse	Donkey	AF594	3.75 µg/ml	715-585-150, Jackson
Guinea pig	Donkey	AF647	3.75 µg/ml	706-605-148, Jackson

For the staining of HEK cells, petri dishes with fixed cells were washed three times in PB, and permeabilized for 10 minutes in 0.05M Tris-buffered saline (TBS, 0.9% NaCl, pH = 7.4) containing 0.1% Triton X-100. Dishes were then incubated with Guinea pig anti-CB_1 primary antibody, and in some experiments, mouse anti-EGFP antibody, for 1 hr. The cells were then washed in TBS three times and stained with secondary antibodies (Cy3 + AF647 donkey anti-Guinea pig for single CB_1, and AF594

donkey anti-mouse and AF647 donkey anti-Guinea pig) in TBS for 1 hr. Finally, dishes were washed twice in TBS and twice in PB, and stored in PB with 0.05% NaN_3 until imaging.

Before immunostaining, slices containing filled neurons were developed to visualize the biocytin labeling inside the recorded cell. After extensive washing in PB and TBS, slices were treated with 0.5% Triton X-100 in TBS twice for 30 minutes, and incubated in AF488-labeled streptavidin (1:1000, Jackson). Sections were then washed in TBS and PB consecutively, mounted on glass slides in Vectashield (Vector Laboratories, Burlingame, USA), covered with #1.5 borosilicate glass coverslips (Menzel-Gläser, Braunschweig, Germany), and sealed with nail polish (Crystal Nails, Melbourne, USA). Labeled cells were imaged by confocal microscopy (see below), and then the coverslips were removed and the sections returned to PB.

For STORM experiments, sections of perfused brain or slices containing developed neurons were embedded in 2% agarose, and sectioned on a Vibratome to 20 μm thickness. Sections were washed extensively in TBS, and then incubated in blocking solution containing 1% bovine or human serum albumin in TBS (also containing Triton X-100 for perfused brain samples). Then, the sections were incubated overnight in TBS containing one or two of the primary antibodies (Guinea pig anti-CB_1, mouse anti-CCK, mouse anti-bassoon, rabbit anti-CB_1), washed extensively in TBS, and then incubated in the respective secondary antibodies for 4 hours. Finally, sections were washed again in TBS and PB, the hippocampi were trimmed, and mounted on glass coverslips (one section per coverslip) in PB, and let to dry. Coverslips were stored dry at 4°C until imaging.

3.6. Microscopy

For the imaging of cellular morphology, confocal z-stacks were recorded from the field of view containing the filled cell (2048 by 2048 pixels, 131 nm/px) with 0.75-1 μm step size and 100-150 μm range using 488 nm illumination and 20x objective (0.75 NA, CFI Plan Apo VC, Nikon) on an A1R or C2 confocal microscope fitted on a Ti-E or a Ni-E microscope, respectively (Nikon).

All STORM imaging was carried out on an N-STORM system, consisting of a Ti-E inverted microscope equipped with laser TIRF illuminator (with a 2x magnifying lens in the illuminator to increase power density at the center of the field), 300 mW solid-state 647 nm laser, 405, 488 and 561 nm lasers, an Andor iXon DU-897 back-lit cooled EMCCD (equipped with cylindrical lens in the light path for astigmatic 3D imaging), a C2 confocal scanhead, and a 100x objective (1.49 NA, CFI Apochromat TIRF, Nikon). Before imaging each specimen, fresh imaging medium was prepared, containing 5% glucose, 0.1 M 2-Mercaptoethylamine (30070, Sigma, St. Louis, USA), 1 mg/ml glucose oxidase (G2133, Sigma) and 1500 U/ml catalase (C30, Sigma) in DPBS (Dani et al. 2010).

For glass-bottom petri dishes containing HEK cells, storage buffer was removed and the imaging medium was added, the dish was closed air-tight and placed on the microscope stage. Randomly selected GFP-positive cells were first imaged in confocal mode, by acquiring z-stacks with sequential illumination with 488 and 561 or 647 nm excitation (512 by 512 by 15 voxels, 80 by 80 by 150 nm resolution. Then the 3D-STORM image of the same field of view was acquired for each cell (2000 cycles of 1 activation (561 nm, low power) and 3 reporter (647 nm, maximal power) frames each, 30 ms exposure time) using STORM filter cube (excitation by any line, emission in far-red).

For tissue sections, imaging medium was spread on a slide, and then the slide was covered with the coverslip containing the section, sealed with nail polish, and equilibrated on the microscope stage for 5 minutes. Imaging was continued for up to 3 hours after covering the sample. Axon terminals were selected by systematically scanning through the sample and including every eligible axon terminal (within 10 μm from the coverslip, field of view not overlapping with previous images from the same sample). Confocal z-stacks were taken as described above, and then single-channel or dual-channel 3D-STORM images (1000 cycles per channel, 1 activation (405 or 561 nm, low power) and 3 reporter (647 nm, maximal power) frames, 30 ms each, per cycle) were recorded. For dual-channel STORM, cycles for the two channels were alternated. Before starting acquisition, fluorophores in the field of view were sent to dark state by maximal illumination with 647 nm. The protocol published by our group contains

additional details and recommendations for the application of the STORM method (Barna et al. 2016).

3.7. Image analysis

Low-magnification confocal images of filled neurons were analyzed in ImageJ, or reconstructed in Neurolucida 10 (MBF Bioscience, Williston, USA). For producing bouton distribution histograms and calculating BDI, the following procedure was applied. Stacks were loaded in ImageJ, enhanced using the Despecle and Subtract Background commands, and maximum intensity z-projections were generated. On these, the borders of the oriens, pyramidale and radiatum layers were hand-drawn based on the pyramidal cell nuclei, and added to ROI Manager. Then, the position of each visible axon terminal was clicked, saving its coordinates. Then, the distance of each bouton from the layer borders was calculated, normalized to the thickness of the pyramidal layer, converted to reflect laminar position (i.e. zero is the center of the pyramidal layer, negative values are towards oriens, and positive values are towards the radiatum), and rounded to one decimal precision. These values were used to plot histograms, and to calculate a bouton distribution index (BDI) from the descriptive statistics of all boutons of a cell according to the formula BDI = $\frac{0.5}{|M|*(Q3-Q1)}$, where M is the mode and Q1 and Q3 are the upper and lower quartiles of the distribution, respectively. This index is vulnerable in case of multimodal distributions, therefore in such cases, the histogram was inspected to reveal any possible mismatch. If two modes were in adjacent bins, the mean of the two modes was used.

High magnification confocal stacks (used for correlated STORM analysis) were deconvolved with Huygens Professional (SVI, Hilversum, Netherlands) using theoretical PSF (based on the optical parameters of the imaging) and classic maximum likelihood estimation algorithm, 100 iterations. STORM images were processed with NIS Elements STORM Module (Nikon) using the same experimentally determined z-calibration curves and identical peak thresholds for all images. For dual-channel STORM images, crosstalk correction was performed with identical parameters for all images. Image-based drift correction was enabled. The resulting molecule list, containing the drift corrected, 3-dimensional coordinates and the channel assignment of each localization point (LP, one blinking event was considered one LP even if the event

lasted several frames) in the field of view, were exported in text format for further analysis.

To select the LPs belonging to the filled axon terminal of the labeled neuron, deconvolved confocal stacks were loaded in ImageJ, enhanced using the Despecle, Subtract Background and Enhance contrast commands, and the three central optical sections, corresponding to the volume covered by the 3D-STORM image, were maximum intensity z-projected. These images were then transformed using the TurboReg plugin based on a calibration to remove most of the differences in magnification, rotation and translation between confocal and STORM image of the same field of view. The text file containing STORM coordinates was read. Then, with only the biocytin channel displayed, a rectangular selection was made around the labeled axon terminal. The confocal image within the rectangle was copied, transformed to RGB color image to display all channels, and rescaled to 1 nm per pixel resolution. Then, each STORM LP was checked if it is within the rectangular region, and included points were transformed to match the rescaled and cropped confocal region and displayed on the image as a multipoint ROI with 1 nm precision. To eliminate any remaining mismatch between the confocal and STORM image, the confocal image was moved manually until the STORM and the corresponding confocal channel were in perfect alignment, while the LP positions remained unaltered. Finally, the outline of the biocytin-positive axon terminal was drawn manually, and STORM points within this shape were identified, and their coordinates and channel assignments were saved as a text output. The size of this region, and the number of included points were saved and used for the area, perimeter and NLP measures. Morphological descriptors were also measured using built-in ImageJ functions. These are dimensionless numbers reflecting the following ratios: circularity is the ratio of the area and perimeter normalized to that of a circle, aspect ratio is the ratio of the axes of a fitted ellipse, and solidity is the ratio of the area of the shape over its convex area.

The saved molecule lists were used for all the subsequent measurements and analyses carried out using custom-written scripts in ImageJ, Matlab or Python languages. Specific analysis methods are explained in the Results chapter together with

the relevant biological context, and are described in detail in the original publication (Dudok et al. 2015).

Visualization of the STORM images was obtained with NIS-Elements STORM module as two-dimensional Gaussian representations, or with VMD (University of Illinois, USA), which is a program for three-dimensional visualization of molecule structures. To feed STORM data to VMD, LPs were converted to pdb format, originally used to store positions of atoms. Each LP was added as an atom (using the measured position of LPs), and convex hull edges were added as bonds. Color coding was assigned either as different atom types for channels, or as separate chain identifiers for clusters.

3.8. Statistical analysis and figure preparation

Statistical analysis was performed and graphs were plotted using Statistica 10 (Dell, Round Rock, USA). Before selecting the appropriate probe for hypothesis testing, samples were evaluated whether data points from different cells or animals of a group can be pooled using nonparametric Kruskal-Wallis ANOVA. If the test revealed no difference between cells or animals of the group in any of the groups, the data points were pooled. Otherwise, the mean of each cell or animal was calculated and used for further analysis. The resulting sample was then tested for normality and equality of variances using Saphiro-Wilk test and F-test, and the histograms were inspected. Typically, the properties of the samples did not meet the assumptions of parametric probes, thus, nonparametric probes were used. For the comparison of two groups, Mann-Whitney U test with continuity correction (two-sided) was used if the sample sizes were comparatively low (<20) for its power to detect differences if the means of groups are different. For larger samples, two-sample Kolmogorov-Smirnow test was used, for it is less likely to produce false positive results with increasing sample size, and is more sensitive to detect differences in distributions even if the means are not very different. For comparisons of multiple independent groups, Kruskal-Wallis ANOVA was used, with post-hoc median test for multiple comparisons if difference between groups was detected. Data were presented as scatterplots, histograms, cumulative histograms or box plots.

For the selection of individually sized bouton populations from the two cell types, the following algorithm was used. First, the sizes, and individual and group identifiers of all available boutons were read into the input sample. Then, boutons with size outside the interdecimal range of their respective group were discarded to avoid including extremes. Next, a bouton from one (source) group was selected at random, and the bouton from the opposite (pair) group with the least difference in size was found. Both boutons were added to the output sample and removed from the input, and this process was continued alternating the source and pair groups until the output sample contained the desired number of boutons.

For figure preparation, unmodified digital micrographs were converted to 8-bit RGB images, and edited and labeled using Photoshop CS5 (Adobe, San Jose, USA). In case of correlated confocal and STORM images, snapshots of the Gaussian representations were generated, overlaid and manually transformed to match the corresponding confocal image, and, in some cases, cropped for the region of the labeled axon terminal. Note that this method is different and independent from the more precise method used for analysis (which uses coordinates instead of a rendered image), but it is still appropriate to create faithful representations of the STORM LPs belonging to a labeled profile. Confocal images of multiple samples presented in the same figure were modified jointly and identically during every step to preserve any differences. Adjustment to contrast and gamma correction were done to facilitate inspection by humans. All microscopic images are false colored, and hue was adjusted for each channel to meet the color composition of the given figure. For most of the correlated confocal-STORM image pairs, the confocal images were resized using nearest neighbor resampling to preserve the edges of original pixels, except for Figure 10, where bicubic resampling was used to smoothen the outline of the axon.

3.9. Personal contribution to the results

The results presented in this study are a result of a collaborative effort, and several researchers provided invaluable samples, reagents, microscopy- and programming support. My contribution was central in solving the technical challenges of microscopy

DOI:10.14753/SE.2017.1972

and image processing, planning experiments, capturing, analyzing and interpreting microscopy data, and preparing figures.

HEK cells were maintained and transfected by Christopher Henstridge (Figure 2), and László Barna recorded most of the STORM images of HEK cells. I have performed immunostaining and part of the imaging, and image analysis (Figure 3). Immunostaining and STORM for Figure 6 was carried out by Eszter Szabadits and László Barna. I have analyzed the data and prepared the figure. For all experiments involving individually filled neurons, all patch-clamp recordings and analysis of electrophysiological data were performed by Marco Ledri, Szilárd Szabó, and Sang-Hun Lee. I have carried out the morphological analysis and reconstruction of cells, and the immunostainings with technical assistance from Balázs Pintér. During experiments with high sample numbers, I have collected the vast majority of STORM images, while Stephen Woodhams and Szilárd Szabó contributed with collecting some of the images. I have developed the method for the correlated visualization and analysis of confocal and STORM images, and processed and analyzed all images. For molecular distance (Figure 15), and clustering calculations (Figure 16), I have acquired and processed the images, and analyzed the results, while László Barna performed the distance or cluster analysis on the data sets. Chronic and acute drug treatments were done by Claudia Sagheddu and Sang-Hun Lee, respectively, and I performed the processing, imaging and analysis of the samples. I have performed all the statistical analysis, and prepared all the figures in the study, except for Figure 1, which is the work of László Barna.

DOI:10.14753/SE.2017.1972

4. Results

4.1. STORM super-resolution imaging in cell culture model

4.1.1. Assessing the quantitative power of STORM

To validate the use of STORM for studying the nanoscale subcellular distribution of CB_1 cannabinoid receptors, we have first used the simplified model of a heterologous expression system before turning to complex brain tissue specimens. Human embryonic kidney cells (of the HEK-293 cell line) were cultured under routine adherent cell culture conditions, and were transiently transfected with a plasmid DNA containing the coding sequence of the human *cnr1* gene (encoding the CB_1 protein) fused with the coding sequence of the fluorescent protein EGFP, driven by a viral promoter. This construct has been shown to express a chimeric CB_1 protein tagged N-terminally with EGFP (EGFP-CB_1), which is transported to the plasma membrane of HEK cells (Tappe-Theodor et al. 2007). After fixing and permeabilizing the cells, we have carried out indirect fluorescent immunostaining with a polyclonal primary antibody raised against EGFP or CB_1. For the detection of primary antibodies, we have used custom-made secondary antibodies, which were produced by conjugating IgG molecules with reactive versions of the small organic fluorescent dye molecules AF647 and Cy3 (Figure 1). While AF647 is bound to the IgG at a low stoichiometry (less than one dye per protein molecule), Cy3 is bound at a ratio of over 2:1. This configuration allows the detection of AF647 as a reporter, and the use of Cy3 as an activator during STORM imaging (Rust et al. 2006).

DOI:10.14753/SE.2017.1972

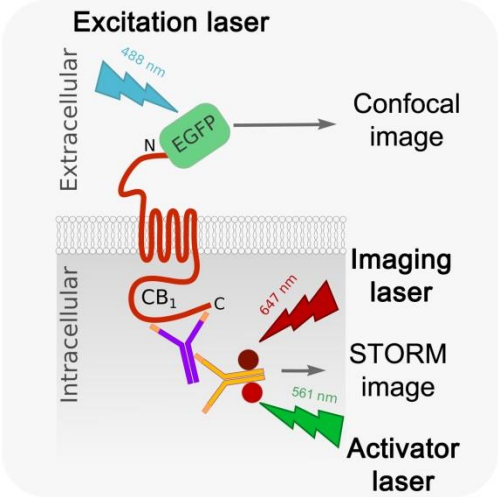

Figure 1. Schematic drawing of the experimental setting for correlated confocal and STORM imaging of chimeric molecules. CB_1 receptors labeled by a genetically encoded fluorescent tag and by immunostaining can be detected with two independent methods using confocal and STORM imaging modalities (Dudok et al. 2015).

After immunostaining, EGFP-CB_1 can be imaged using conventional fluorescence or confocal microscopy by detecting the intrinsic fluorescence of EGFP, and also by using STORM to detect the reporter dyes (Figure 1). Thus, if the anti-CB_1 immunostaining and STORM imaging are sensitive and specific, both methods of detection are expected to display similar spatial distribution. Moreover, if the number of detected molecules in STORM is proportional to the number of CB_1 proteins, the relative intensity of several individual cells with variable expression levels is expected to change in a correlated manner between the confocal and STORM images. To test these hypotheses, we have compared correlated image pairs of transfected HEK cells captured with constant acquisition settings. These image pairs demonstrated that the distribution of the signal is qualitatively similar between the confocal and STORM images of the same cell (Figure 2). Cells that didn't show GFP fluorescence (untransfected cells in the culture) had negligible levels of STORM signal, confirming the specificity of the staining and the imaging process, and indicating that HEK cells don't express native CB_1 receptors.

DOI:10.14753/SE.2017.1972

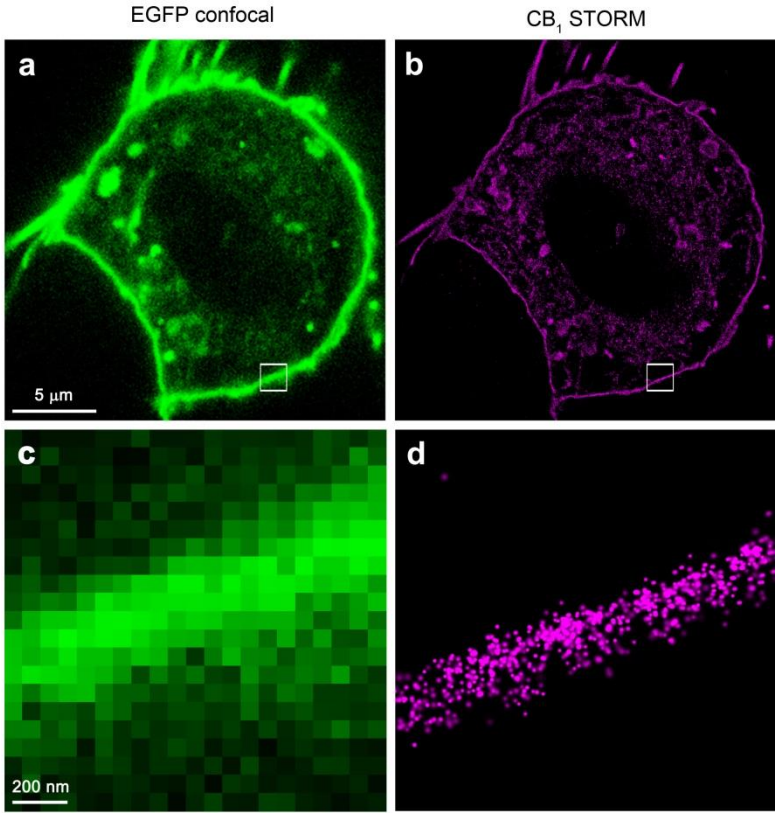

Figure 2. Correlated confocal and STORM images of a representative HEK cell expressing EGFP-CB_1. (a) Confocal image of the intrinsic EGFP fluorescence demonstrates the targeting of the construct to the plasma membrane. (b) STORM image of the anti-CB_1 immunostaining of the same cell reveals similar distribution of the two types of detected signal. (c) High magnification view of the boxed region from panel (a) shows the blurred nature of the confocal image, due to limited resolution. (d) In contrast, the high power STORM image provides sharp visualization of the plasma membrane of the cell (Dudok et al. 2015).

Our next goal was to determine whether the quantification of localization points (LP) in the STORM data is a reliable way to measure relative protein abundance. To answer this question directly, one would need to take STORM images of immunostained samples with a series of known protein concentrations, and define the dynamic range within which the number of localization points (NLP) is linearly correlated to protein concentration. However, it's not trivial to perform such an experiment, especially not in a setting that mimics the cellular environment in which biological measurements are carried out. Using the EGFP fluorescence to measure the relative protein concentration across samples, however, is feasible, assuming that the number of detected photons is related to the number of excited molecules. Indeed, fluorescence intensity of confocal images has been used to determine the copy number

of EGFP-tagged molecules (Verdaasdonk et al. 2014). Staining the samples using antibodies, however, may introduce additional limitations for quantification, as the concentration of bound antibodies may not follow the concentration of epitopes in a linear fashion. On the other hand, it has been shown that under well-optimized conditions, anti-EGFP immunostaining can reliably report EGFP levels (Mortensen and Larsson 2001). On confocal images of our HEK cell samples, intrinsic EGFP fluorescence was strongly correlated to the intensity of indirect fluorescent anti-CB_1 immunostaining (Figure 3a), indicating that the expression level of the construct, the concentration of primary and secondary antibodies, and the detector settings of the confocal microscope were adequate for the reliable measurement of immunofluorescence intensity (n = 65536 pixels from one representative image, Spearman's rank order correlation, $R = 0.97$, $p < 0.0001$).

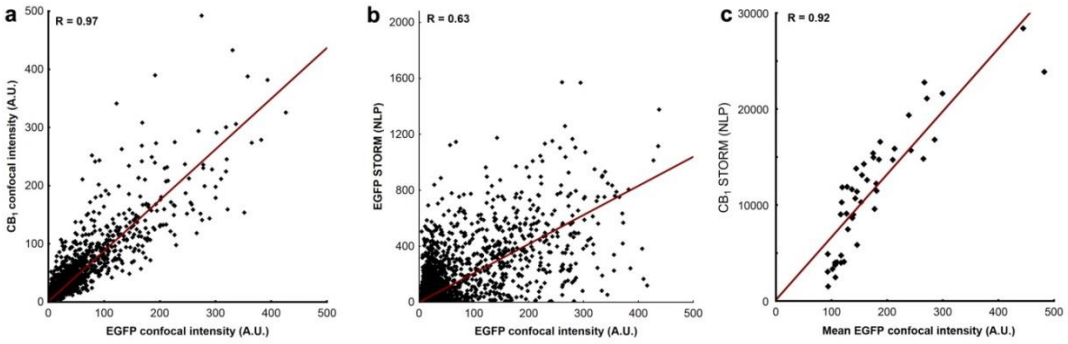

Figure 3. Immunostaining and STORM microscopy is a valid method to probe molecular abundance. (a) Pixels of a confocal image of a representative EGFP-expressing HEK cell immunostained against CB_1 have strongly correlated intensity values in both the intrinsic EGFP fluorescence and the immunofluorescence channels. (b) On the contrary, the intrinsic EGFP fluorescence intensity of pixels is weakly correlated to the NLP in the corresponding area of the anti-EGFP STORM image, due to the different spatial resolution of the two imaging modalities. (c) On the level of individual cells immunostained against CB_1, however, the total EGFP fluorescence from the cell is in strong correlation with the NLP in the STORM image.

The stochastic nature of single molecule localization microscopy raises the question whether the method is suitable for quantification. As the number of detected blinking events is highly variable between individual fluorophores, it is obvious that one LP on a STORM image does not correspond to one epitope in the sample (Dempsey et al. 2011). However, if the density of LPs in a given part of the image is proportional to the concentration of epitopes in the corresponding volume of the sample, the NLP can be

used as a proxy to determine the relative number of proteins. To test this hypothesis, we have investigated the relationship between intrinsic EGFP fluorescence intensity of individual pixels of confocal images, and the NLP from anti-EGFP immunostaining in the corresponding areas of STORM images (Figure 3b). Due to the unavoidable poor pixel-level alignment of the confocal and STORM signals, caused by the different resolutions of the two imaging modalities, we have found only weak correlation of intensity levels (n = 65536 pixels from one representative image, Spearman's rank order correlation, $R = 0.63$, $p < 0.0001$).

Thus, to determine whether anti-CB_1 STORM labeling intensity follows EGFP-CB_1 levels, we have imaged several fields containing individual HEK cells with varying expression levels. Comparison of the integrated signal intensities from whole image fields revealed strong correlation between the measurements obtained by either confocal or STORM microscopy (n = 46 cells from 5 coverslips, Spearman's rank order correlation, $R = 0.92$, $p < 0.001$). The STORM NLP followed EGFP fluorescence intensity in a linear fashion in the medium range of expression levels (Figure 3c). In the high and low extremes of expression levels, however, the confocal intensities were above the linear fit. This can be explained by assuming that either STORM underestimates, or confocal imaging overestimates signal intensity. At the most strongly expressing cells, STORM detection of immunostaining may be confounded by saturation effects such as the spherical limitations of antibody crowding, and/or the overlapping blinking of fluorophores interfering with single molecule detection. Contrary, on the low end, STORM is supposed to be very sensitive in detecting low density signal, as the signal-to-noise ratio (SNR) for even one molecule is sufficient for detection, while confocal imaging is more affected by background fluorescence and Poisson noise, preventing the detection of weak signal. Taken together, this experiment demonstrates the validity of quantitative STORM experiments in biological sample.

4.1.2. Optical sectioning properties of 3D-STORM

The imaging strategy used throughout this study to determine the z coordinates of STORM LPs relies on the astigmatic distortion of the single-molecule images of blinking fluorophores (Huang et al. 2008b). While this method allows the recording of volume images with super-resolution accuracy in all three dimensions without scanning

DOI:10.14753/SE.2017.1972

the sample, it is important to note that the sensitivity of detection is diminishing quickly with increasing distance from the focal plane. This effect is due to the fact that the single emitter image distorted by the cylindrical lens is spread over a larger area than the original image, resulting in reduced SNR, and thus, reducing the probability of successful detection. Moreover, as the spherical aberrations in the image are minimal for emitters between the coverslip and the focal plane, but are worse for emitters located deeper than the focal plane, the decrease in detection sensitivity is also asymmetrical. As a result of these issues, a single 3D-STORM image can contain LPs within 600 nm distance from the focal plane, the probability of detecting a blinking event is only 50% already at 100 nm axial distance (Figure 4). Consequently, a single 3D-STORM image can be regarded as an optical section, but without a definite thickness. We have found empirically that the optical section of one STORM image corresponded to the maximum intensity projection of three neighboring confocal slices (using 150 nm step size).

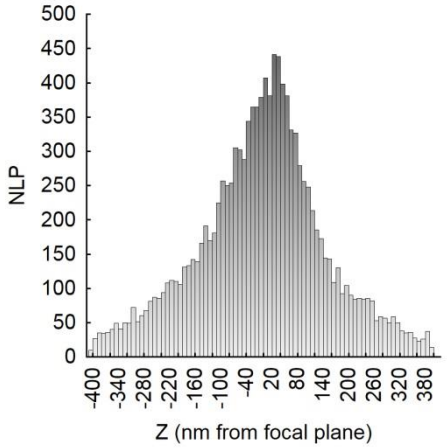

Figure 4. Histogram of the axial coordinates in a 3D-STORM image. Distribution of LPs from the whole CB_1 STORM image of a representative EGFP-CB_1-expressing HEK cell. Note the asymmetrical decrease in the number of points with increasing distance from the focal plane (z = 0). The full width at half maximum of the Gaussian fit is 352 nm.

4.1.3. Determining the localization precision of STORM images

Superior spatial resolution is the main advantage of single molecule localization microscopy over standard methods of fluorescence microscopy. Localization precision can be determined directly by imaging immobilized fluorescent dye molecules, and fitting a Gaussian function on the calculated positions over multiple detections of the same molecule. But the resulting values may not necessarily reflect the quality of

images taken from biological samples. Since the accuracy of positioning detected blinking events largely depends on the SNR of the individual fluorophore images and sample stability, it is imperative to measure localization precision under imaging conditions that are equivalent to the conditions of collecting the actual data, or, more practically, on the same image. This is possible by evaluating isolated clusters of multiple blinking events, presumably originating from single, non-specifically bound secondary antibodies. As these clusters don't contain enough LPs for fitting, we have selected several clusters, and pooled all clusters by aligning them on their centers of masses (Figure 5).

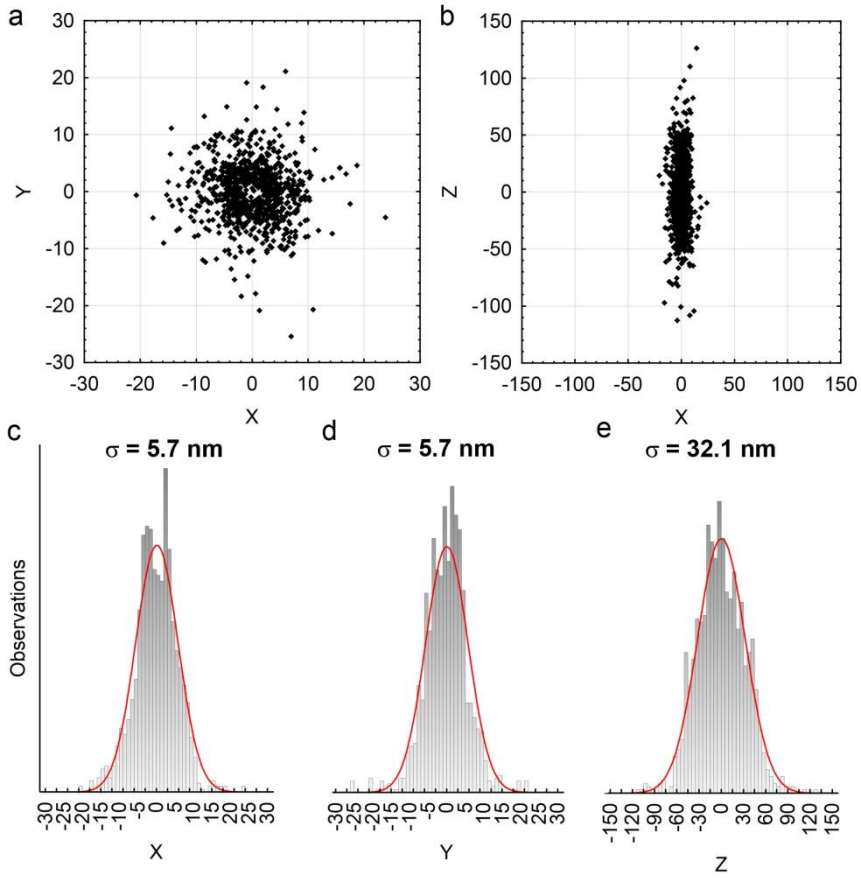

Figure 5. Fluorophore localization precision in the CB_1 STORM images of HEK cells. (a) Scatterplots of the lateral coordinates of the LPs from the pooled clusters of multiple detections of fluorophores. The sparseness of points at the origin of the graph is due to the low number of LPs in individual clusters, resulting in the absence of a point at the center of mass of most clusters. (b) Scatterplot of the axial coordinate reveals larger localization error of the z coordinate. Note that the scale values are different between panels a and b. (c-e) Histograms of the values of coordinates (grey), with the Gaussian fits (red lines) and the calculated standard deviations. All coordinates are in nanometers.

For the calculation of localization precision, clusters containing altogether 1220 LPs were selected from 5 randomly picked STORM images of CB_1 immunostaining. The standard deviations of the coordinates were 5.7 nm in the lateral and 32.1 nm in the axial dimensions, respectively (Figure 5c-e).

4.2. STORM super-resolution imaging of cannabinoid receptors in brain tissue

4.2.1. Validating the immunostaining and imaging protocol

The first studies that introduced the STORM imaging technique have been using samples such as fluorescently labeled cell-free DNA (Rust et al. 2006), synthetic microtubules (Dempsey et al. 2011), or *in vitro* cell cultures (Bates et al. 2007). These types of samples allow the acquisition of images with excellent SNR from the immediate vicinity of the coverslip. While others have successfully implemented STORM for cryosections from fixed brain tissue (Dani et al. 2010), directly following published protocols was not adequate for achieving our goal, the imaging of labeled axon terminals of individual neurons. First of all, our preliminary experiments suggested that immunostaining of mounted cryosections was less sensitive and less specific compared to the staining of vibratome sections in a free-floating manner. The second issue is the preservation of the tissue structure at the surface of the thin sections, as images with proper SNR can only be collected from within 10 µm distance from the coverslip. While cryosections were suitable for population-level observations in parts of the samples, reliably finding and imaging labeled axon terminals required a more consistent preservation of the tissue. Thirdly, as the photoswitching of the fluorescent dyes requires the presence of a special imaging medium, it was necessary to store the samples between immunostaining and the actual imaging in a way that allows the application of fresh imaging medium. Thus, in order to facilitate the use of STORM for quantitative cell-specific studies, we have used free-floating immunostaining protocol on vibratome sections cut thinner than usual (to 20 µm thickness). After immunostaining, the sections were mounted on the coverglasses and dried, to be covered with imaging medium only at the beginning of the imaging session (Barna et al. 2016).

To validate this protocol, we have used sections from the hippocampi of WT and CB_1 KO mice (Zimmer et al. 1999), immunostained against both CB_1, and the

neuropeptide CCK, which is widely used as a marker of CB_1-expressing interneurons (Katona et al. 1999; Tsou et al. 1999). In the pyramidal layer of the CA1 subfield, we have observed the characteristic staining pattern of CB_1, labeling varicosities in basket-like arrays around the immunonegative somata of pyramidal neurons (Figure 6a). These varicosities presumably correspond to inhibitory axon terminals of GABAergic interneurons, as indicated by CCK-immunoreactivity (Figure 6b). STORM images of the axon terminals revealed hollow, ring-shaped CB_1 labeling, with a level of detail significantly exceeding that of the epifluorescent images (Figure 6c-f). This striking sub-boutonal staining pattern is likely to result from the predominant plasma membrane targeting of the receptors, which has been reported previously by electron microscopic studies (Katona et al. 1999; Nyiri et al. 2005). As the focal depth of a single STORM image is maximum 600 nm with the sensitivity of detection sharply decreasing away from the focal plane, while the diameters of the axon terminals range from 800 to 1000 nm (Takács et al. 2014), these STORM images represent partial optical sections of the boutons.

DOI:10.14753/SE.2017.1972

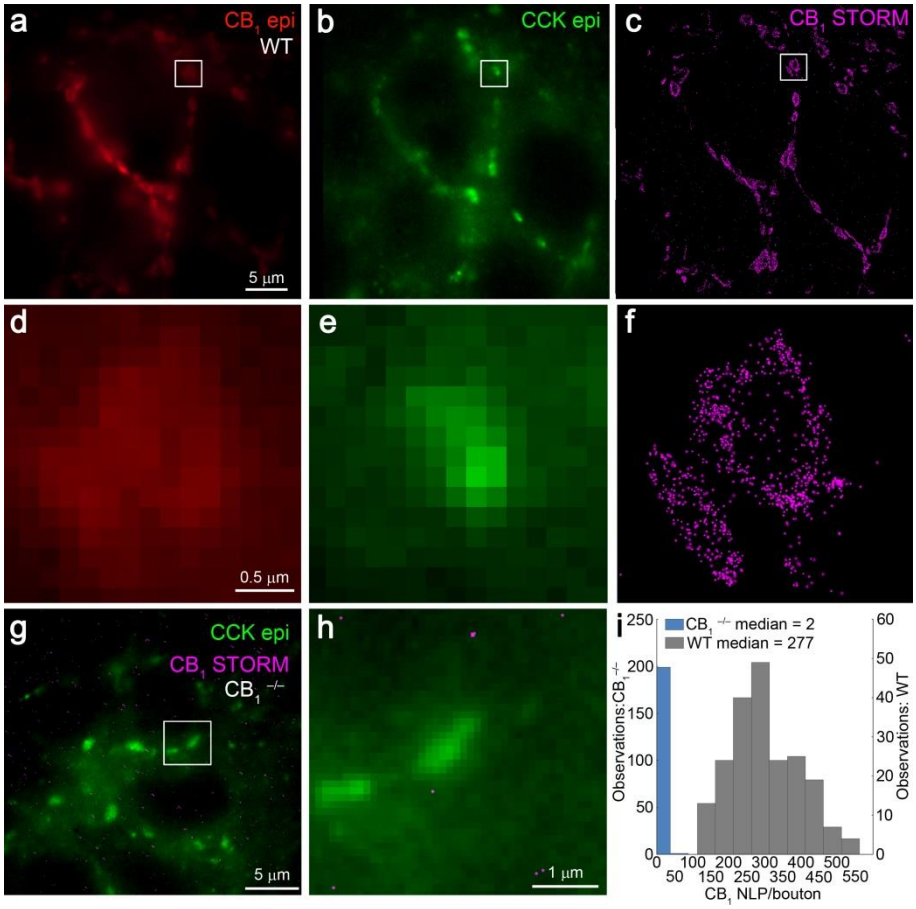

Figure 6. Visualization of CB_1 receptors on hippocampal axon terminals using STORM. (a) Epifluorescent micrograph of CB_1 immunostaining in the pyramidal layer of hippocampal CA1 region, illustrating the labeling of varicosities around immunonegative somata. (b) The same varicosities are also positive for CCK. (c) STORM image of the same field of view reveals the sharp plasma membrane labeling visualized by CB_1. (d-f) High magnification view of the boxed region from the top panels. (g-h) The CB_1 STORM signal was nearly undetectable in sections from CB_1 KO mice. (i) Histogram of the CB_1 NLP detected in CCK-positive varicosities in WT and KO samples. The low level of background labeling indicates the specificity of the antibody and the imaging process (Dudok et al. 2015).

As the vast majority of CCK-containing cells in the CA1 co-express CB_1 receptors (Bezaire and Soltesz 2013; Katona et al. 1999; Marsicano and Lutz 1999), we were able to evaluate the specificity of the CB_1 immunoreactivity selectively in the investigated profiles, in CCK-positive varicosities (Figure 6g-h). Quantification of the CB_1 STORM NLP in rectangular regions of interest (ROIs) selected based on the epifluorescent image of CCK labeling revealed less than 1% background in the CB_1 immunostaining (n = 208 and 200 ROIs from 3 WT and 2 KO mice, respectively). In boutons from WT mice, the CB_1 NLP was moderately variable (Figure 6i, interquartile range (IQR): 223-

358 NLP, CV = 37%). Altogether, these results indicate that similarly to our previous observations in cell cultures, CB_1 immunostaining detected by STORM is also sensitive and specific in fixed hippocampal sections.

4.2.2. Implementing STORM for studying identified neurons

While the sampling strategy used in the previous measurements is suitable for assessing background labeling, it is not adequate for quantitative characterization of CB_1-expressing axon terminals, because CCK, being a neuropeptide stored in a few dense-core vesicles per axon terminal (Ghijsen et al. 2003), does not outline the area of the boutons precisely, and is likely to introduce a sampling bias towards larger boutons with higher probability of CCK content. Moreover, multiple subclasses of interneurons express CB_1 in the CA1 region. While these neurons are clearly segregated into two groups based on their preferential targeting of perisomatic or dendritic domains (Cope et al. 2002; Klausberger and Somogyi 2008), some studies suggest that both populations can be further classified. A subpopulation of perisomatic CCK/CB_1-positive cells co-expresses a vesicular glutamate transporter (Somogyi et al. 2004), and dendritically targeting cells may show different pattern of axon arborization, identified as perforant path-associated or Schaffer collateral-associated interneurons (Ali and Todorova 2010). One study has identified 7 morphological types of CCK-immunoreactive interneurons, based on the laminar distribution of their axons (Pawelzik et al. 2002). As it is already known that different populations of CCK/CB_1-positive interneurons show fundamentally different sensitivity to both exogenous and endogenous cannabinoids (Lee et al. 2010a), we aimed to develop a cell-specific bouton sampling approach which allows the integrated analysis of morphological, physiological and nanoscale molecular parameters of neurons.

To this end, we have carried out patch-clamp electrophysiological recordings in acute hippocampal slice preparations, and labeled the recorded cells with the small molecule tracer biocytin in the intracellular solution. We have recorded from large multipolar neurons located in the stratum radiatum of the CA1, and measured their passive and active intrinsic membrane properties and firing patterns in response to sub-threshold current injections. Most of the cells exhibited low frequency, adapting firing behavior, known as the regular spiking firing pattern (Figure 7a,d), which is a

DOI:10.14753/SE.2017.1972

characteristic electrophysiological feature of CCK/CB_1-expressing interneurons (Kawaguchi and Kubota 1998; Lee et al. 2010a; Neu et al. 2007). The slices were fixed and the biocytin labeling was developed after the recording, allowing post-hoc morphological characterization. The vast majority of cells belonged to either of two distinctive morphological types: cells displaying selective targeting of the axons to the stratum pyramidale (Figure 7b) were classified as perisomatically targeting (PtIN), whereas cells with extensive axonal arborization in strata radiatum and oriens (Figure 7e) were classified as dendritically targeting interneurons (DtIN).

DOI:10.14753/SE.2017.1972

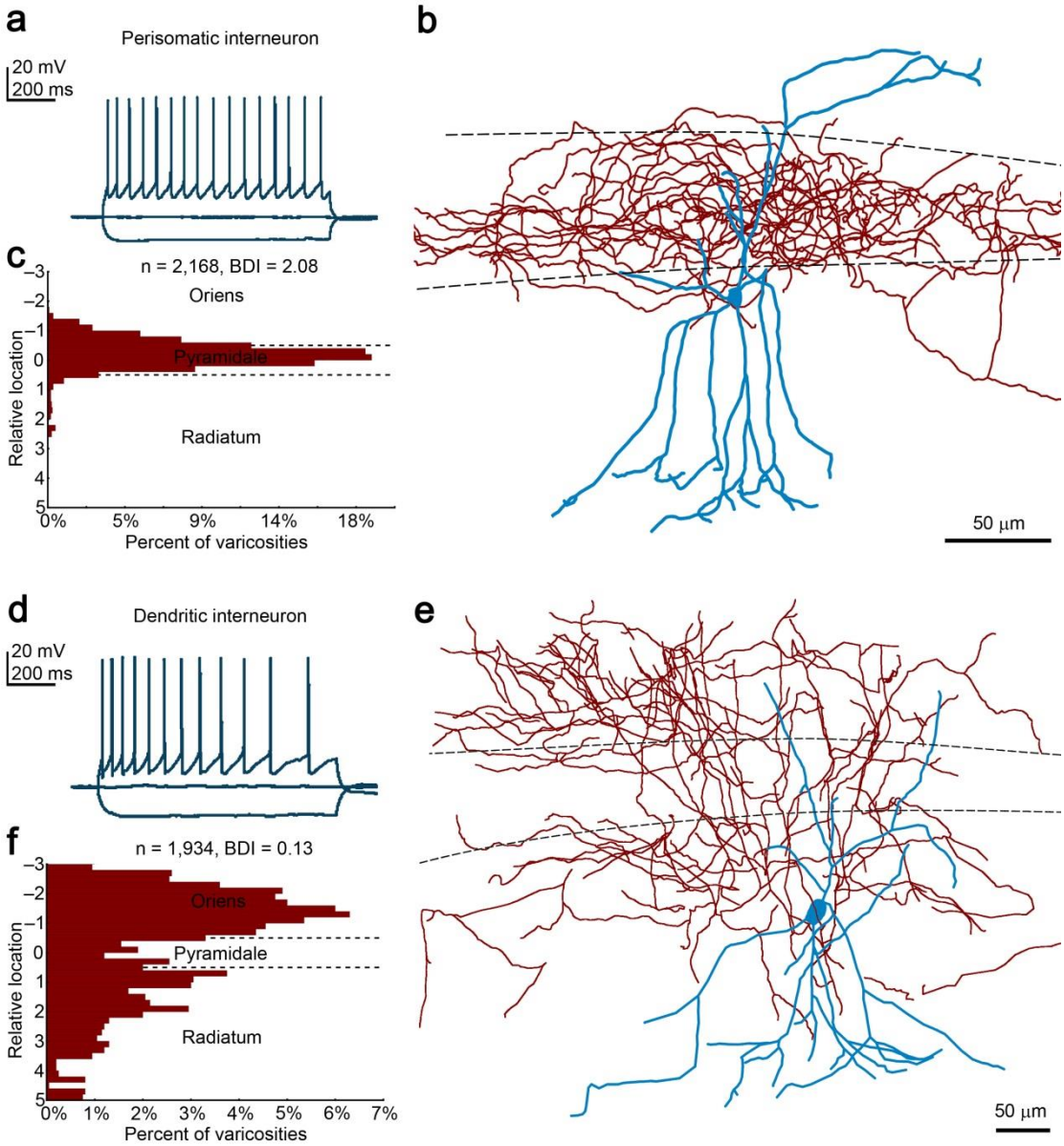

Figure 7. Morphological classification of regular-spiking interneurons. (a) Multipolar neurons in the CA1 radiatum were recorded in whole-cell patch-clamp configuration. The voltage traces in response to hyperpolarizing and depolarizing current steps reveal the regular spiking phenotype characteristic to CCK/CB_1-expressing interneurons. (b) The cells were filled with biocytin through the patch pipette, developed using fluorescent streptavidin conjugates, and imaged using confocal microscopy. Reconstruction of a representative perisomatic interneuron depicts the concentration of axons in the pyramidal layer. (c) Quantitative evaluation of the distribution of axonal varicosities allows the unbiased categorization of the cell as PtIN. (d-f) In case of a second cell, the same experimental workflow revealed a similar accommodating firing pattern, but remarkably different distribution of the axons. This cell was categorized as DtIN (Dudok et al. 2015).

Some cells, however, were difficult to subjectively classify into one of these two groups. Thus, to avoid the pitfalls of examining heterogeneous cell populations, we have developed a quantitative approach for the characterization of axonal morphology, the bouton distribution index (BDI). In order to calculate this index, the borders of the pyramidal layer, as well as the positions of axonal varicosities (n = 997 ± 58 varicosities/cell) were marked on the maximum intensity projections of confocal image stacks captured from each cell, and the distances of varicosities from layer borders were calculated, and normalized to the local thickness of the pyramidal layer. The index was then calculated from the descriptive statistics (mode and IQR) of the relative distances (see Methods). The value of the index is greater than 1 if the mode of the axon distribution is close to the center of the pyramidal layer, and the distance between the first and third quartiles (IQR) is less than the thickness of the pyramidal layer. On the contrary, the value of the index is less than 0.5 if the mode is outside the pyramidal layer and the IQR is greater than the thickness of the pyramidal layer. Thus, the BDI was used to separate clearly perisomatically (BDI>1) and dendritically targeting (BDI<0.5) neurons. Intermediate cells, accounting for less than 5% of all recorded cells with adequate recovery of axons for the BDI analysis, were excluded from the sample.

After establishing an unbiased method for the morphological classification of the cells, we have compared their active and passive electrophysiological properties across cell types (n = 14 and 18 perisomatic and dendritic cells, respectively, all of which displayed continuous firing during the evaluated depolarizing current injection, Mann-Whitney U test, Figure 8). Comparison of cell types revealed the lack of significant difference in the resting membrane potential, input resistance, relative sag amplitude, rebound potential, and action potential amplitude (Figure 8a-e). However, the two populations of cells did display some distinctive active physiological properties, as perisomatic CB_1-positive cells expressed wider action potentials, smaller afterhyperpolarization, and slower initial firing, resulting in a lesser degree of frequency adaptation compared to dendritic cells (Figure 8f-h). These results suggest that while perisomatically and dendritically targeting regular spiking interneurons share a similar electrophysiological phenotype, cell type-specific differences are indeed present between the two groups, confirming the existence of multiple distinct subpopulations within CCK/CB_1-expressing interneurons.

DOI:10.14753/SE.2017.1972

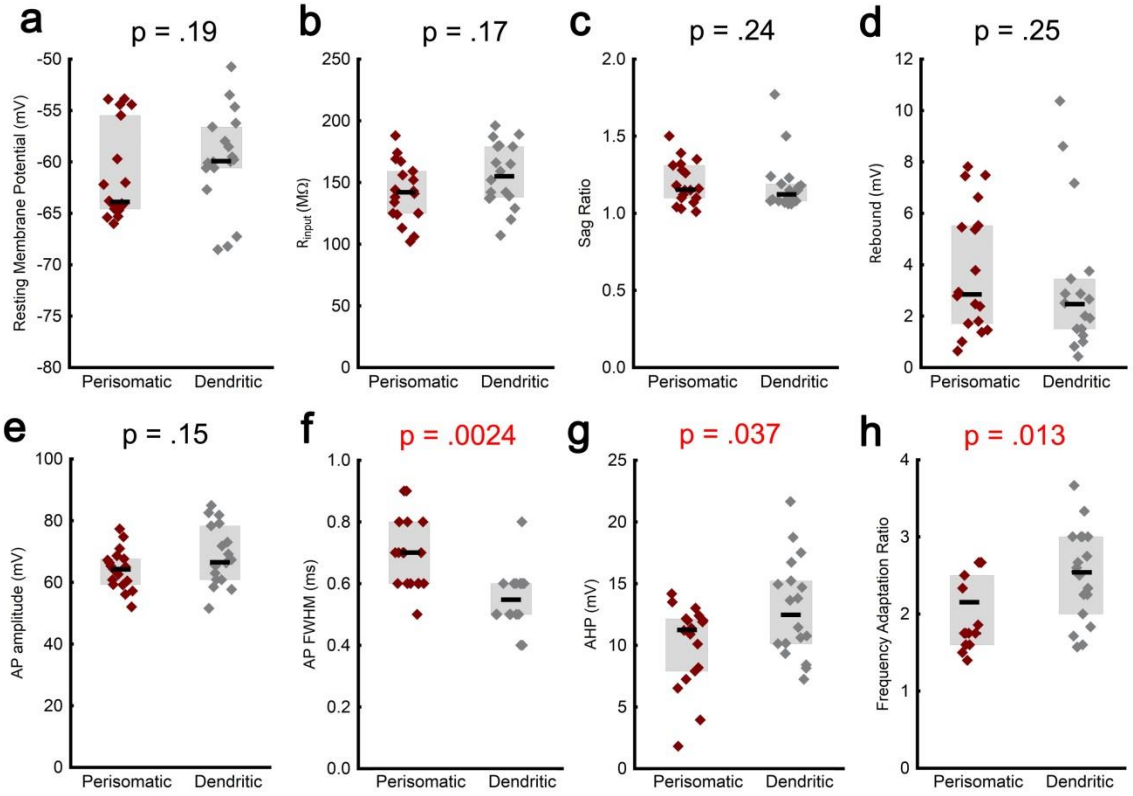

Figure 8. Electrophysiological properties of regular spiking perisomatically- and dendritically-targeting interneurons. Comparison of morphologically identified cells, graphs show raw data (individual cells) and median ± IQR (Dudok et al. 2015).

After the detailed morphological and electrophysiological characterization of the recorded cells, we aimed to obtain high resolution molecular localization data from the axon terminals of the identified neurons. To this end, we have embedded the 300 µm-thick slices containing the developed neurons in agarose, and cut the blocks to 20 µm-thin sections on a vibratome. Then, we have performed immunostaining optimized for STORM as shown earlier (Figure 6). The imaging approach used before, however, was not suitable for precisely outlining the area of the filled axon terminals, due to the low spatial resolution of epifluorescence images obtained on the EMCCD camera. As the EMCCD is optimized for sensitivity to be able to detect single-fluorophore blinking events, the relatively large physical pixel size of the sensor results in the undersampling of the image (160 nm/px using 100x objective). Moreover, the epifluorescent configuration introduces severe blurring of the image due to the effects of light diffraction and the presence of out-of-focus signal. To improve the resolution, we have equipped the STORM microscope with a confocal scan head, and used confocal

DOI:10.14753/SE.2017.1972

imaging followed by deconvolution (see Figure 9). Deconvolution is a post-acquisition computational method, which, using the a priori knowledge of the shape of the PSF calculated from the optical parameters of the imaging, can enhance the resolution of light microscopy images, and remove noise and off-focus signal (Landmann 2002).

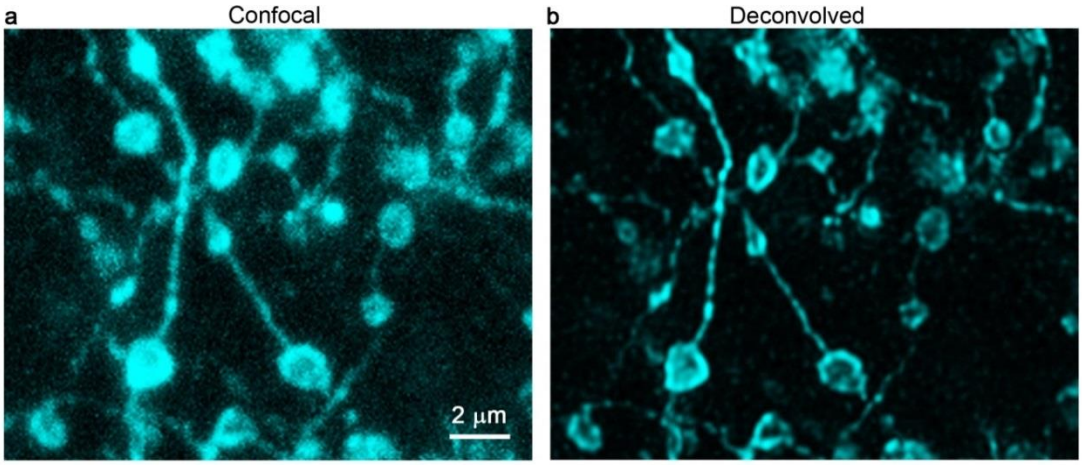

Figure 9. The effect of deconvolution on confocal image stacks. Maximum intensity projection of the same confocal image of CB_1 immunostained fibers in the pyramidal layer of CA1 before (a) and after deconvolution (b). The improved resolution of the deconvolved image is noticeable on the preterminal axonal segments and on the well-resolved doughnut-shaped organization of CB_1 on axon terminals.

On the combined confocal-STORM platform, we have localized the labeled axonal varicosities of the filled interneurons, and captured confocal image stacks of the biocytin fluorescence, followed by 3D-STORM imaging of anti-CB_1 immunostaining (Figure 10). After alignment of the respective image pairs (see Methods), it became possible to dissect the STORM LPs belonging to a given axon terminal. Throughout the study, we have used this correlative imaging approach to obtain nanoscale molecular distribution data from the axon terminals of identified interneurons.

DOI:10.14753/SE.2017.1972

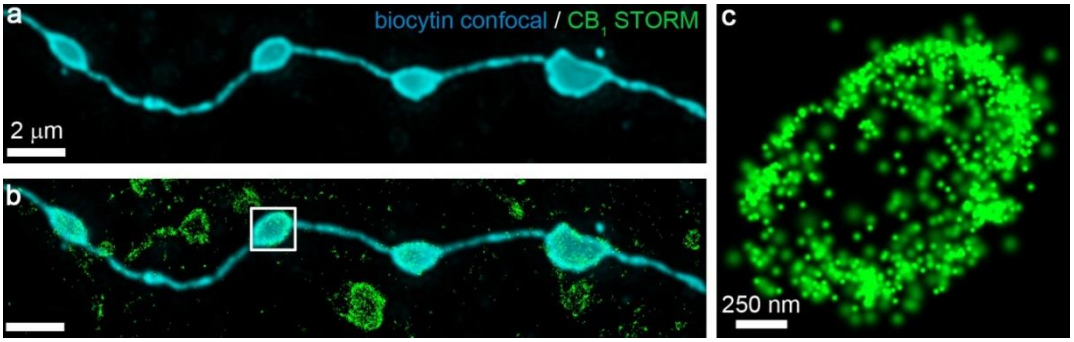

Figure 10. Correlated confocal and STORM imaging from axon terminals of individually labeled neurons. (a) Deconvolved confocal image of a biocytin-labeled string of boutons from an identified, morphologically and electrophysiologically characterized interneuron. (b) Overlaying the STORM image reveals dense CB_1 immunolabeling on the surface of axon terminals and on connecting axonal segments. Maximal intensity projection of 3 neighboring confocal sections (150 nm step size) is shown, to match the volume of the STORM image. The same approach is used throughout the study when correlated confocal and STORM images are shown. (c) STORM image of the boxed axon terminal illustrates the doughnut-shaped distribution of CB_1 on the optical section of the bouton, presumably resulting from the preferential plasma membrane targeting of the receptor.

4.3. Distribution of CB_1 on axon terminals of perisomatically and dendritically targeting interneurons

4.3.1. The abundance of CB_1 on GABAergic axon terminals

Could the higher cannabinoid sensitivity of PtINs be simply explained by more CB_1 receptors on their axon terminals? To test this hypothesis, we have first measured the CB_1 content of on average 50 ± 3 axon terminals from 6 perisomatic and 6 dendritic interneurons with correlated confocal and STORM microscopy. From the confocal images of the biocytin cell fill, we have also determined the size and morphological descriptors of the axon terminals. Comparing the circularity, aspect ratio, and solidity of the axon terminals revealed no significant difference between perisomatic and dendritic cells (n = 6-6 cells, $p > 0.05$, Mann-Whitney U test, Figure 11), even though these cell types target different subcellular domains of the postsynaptic pyramidal neurons.

DOI:10.14753/SE.2017.1972

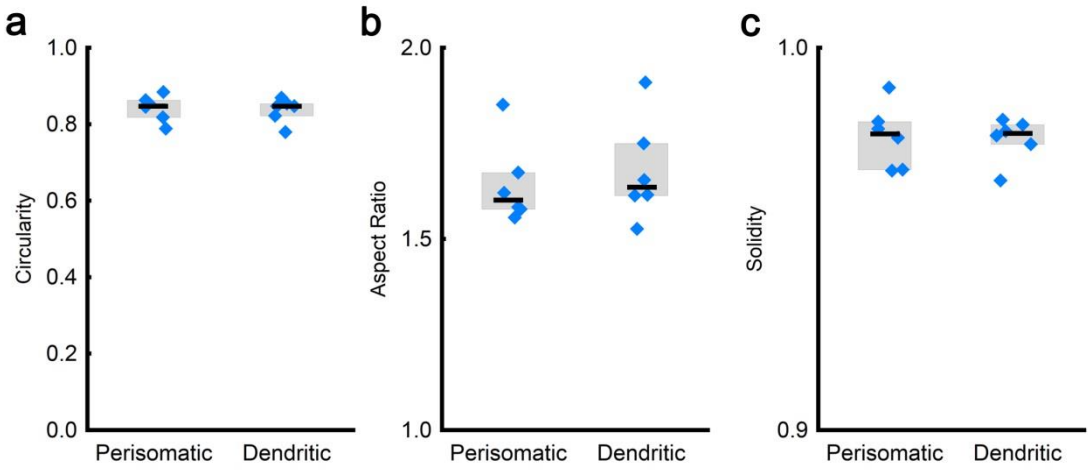

Figure 11. Morphological analysis of axon terminals of perisomatically and dendritically targeting interneurons. Shape descriptors (dimensionless numbers) were measured on confocal images of biocytin-labeled axon terminals using ImageJ. Differences were not significant between cell types ($p > 0.05$). Graphs show raw data (mean values of cells), and median ± IQR (Dudok et al. 2015).

However, when we determined the size of the axon terminals (measured as either the 2D area of the freehand shape drawn on the deconvolved confocal image of the axon terminal, or as the perimeter of a 2D convex hull fitted on the CB_1 LPs), we have found that perisomatic cells had 39% larger axon terminals compared to dendritic interneurons (n = 6-6 cells, Mann-Whitney U test, Figure 12a-b). The abundance of CB_1 receptors, assessed by counting the NLP in the CB_1 STORM image under the 2D area selected based on the biocytin confocal image, was also 40% higher on the axon terminals of PtINs (Figure 12c).

Does the similar effect size in the cell type-specific differences in bouton size and CB_1 NLP reflect correlation between the two parameters? To address this question, we have compared these on the level of individual axon terminals. As the downstream signaling of CB_1 occurs in the plasma membrane (Wilson et al. 2001), the most meaningful way to express correlation is to compare the surface area of the membrane to the number of receptors. However, the exact measurement of the membrane surface from which the STORM LPs are collected is not feasible, because the non-uniform detection sensitivity across the axial dimension (see Figure 4). Thus, we have used the 2D perimeter of the axon terminals, which is proportional to the membrane surface in the optical cross-section of the axon terminal. Despite the relatively high variability in

DOI:10.14753/SE.2017.1972

CB_1 NLP (CV = 56%), CB_1 levels expressed a moderately strong correlation with perimeter in the boutons of both perisomatic and dendritic interneurons (n = 279 and 334 terminals, respectively, Spearman's rank order correlation, Figure 12d).

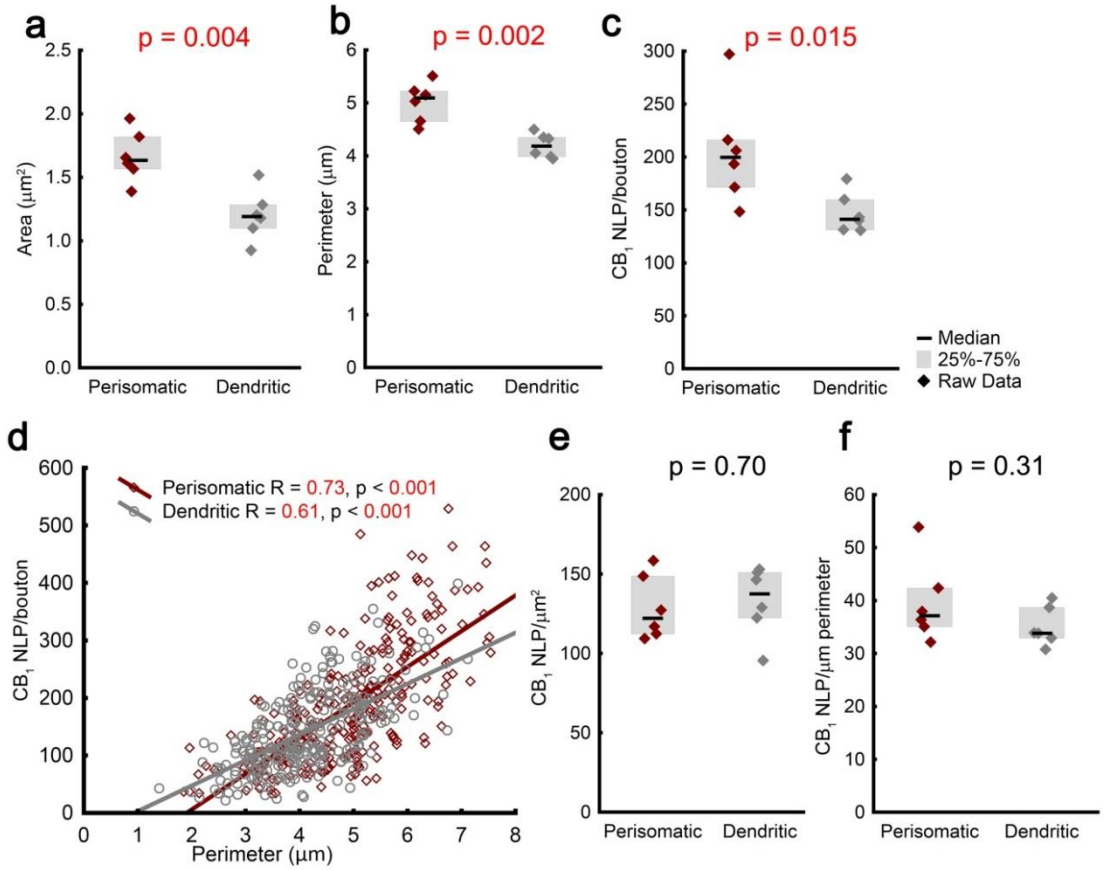

Figure 12. The CB_1 content scales with the size of inhibitory axon terminals. (a-b) Axon terminals of PtINs are larger than those of DtINs. (c) In parallel, perisomatic boutons contain more CB_1 receptors. (d) CB_1 NLP is correlated with bouton size at the level of individual axon terminals. (e-f) On average, perisomatic and dendritic interneurons contain similar density of presynaptic CB_1 receptors. Graphs show raw data (mean values of cells), and median ± IQR (Dudok et al. 2015).

In the light of the correlation between the abundance of CB_1 and the size of axon terminals, we asked whether the density of CB_1 is constant across boutons, or between cell types. While we still have found substantial variability on the level of individual terminals (CV = 41%), no significant difference was present between the mean values of PtINs and DtINs (Figure 12e-f). Taken together, bouton size is a major predictor of the number of CB_1 receptors, and while additional factors may contribute to the variability between axon terminals, both investigated interneuron subclasses express presynaptic CB_1 in a similar density.

DOI:10.14753/SE.2017.1972

4.3.2. Validation of the CB_1 density measurements

Although we have shown in cell cultures that the STORM NLP in anti-CB_1 immunostaining is a reliable reporter of CB_1 protein abundance (see Figure 3), it cannot be ruled out that the similar apparent endogenous CB_1 density on the surface of different types of interneurons is the consequence of saturation effects. Thus, we have directly tested whether the measured density values are in the dynamic range of detection. First, we have compared the STORM labeling density in ROIs (one for every bouton, 30 by 30 confocal pixels each, area = 0.0064 μm^2) placed on axon terminals with ROIs of the same size on the plasma membrane of EGFP-CB_1 expressing HEK cells (n = 10 ROI per cell).

Notably, the axon terminals of both cell types exhibited CB_1 density values (median = 2095 NLP/μm^2) within the range between the two extreme HEK cells (medians = 824 to 4680 NLP/μm^2) (Figure 13a). In agreement with the previous results from all axon terminals (see Figure 12e-f), the mean density of CB_1 in the ROIs on boutons of perisomatic and dendritic interneurons was similar (n = 6-6 cells, Mann-Whitney U test, p = 0.59). Next, we have determined the range of labeling densities on boutons by averaging the ROIs from each individual interneuron, and calculating the mean ± SD ranges of the cell mean values. Interneurons exhibited moderate variability in the mean CB_1 density of their axon terminals, as 10 of the 12 interneurons had mean values within the aforementioned range. Then, HEK cells with their mean values within the density range of interneuron axon terminals were selected (n = 20 HEK cells). The correlation between intrinsic EGFP fluorescence intensity and CB_1 STORM NLP (see Figure 3c) was remarkably strong and highly linear within this range (Spearman's rank order correlation, Figure 13b) in this subset of HEK cells covering the STORM LP density range of endogenous CB_1 on interneuron axon terminals, indicating that the immunostaining and imaging protocol is not saturated. Moreover, examining the histogram of local STORM signal densities expressed as the number of neighboring points within 50 nm 3D Euclidean distance from each CB_1 LP on axon terminals revealed right-tailed distribution (Figure 13c), which also argues against the possibility that detection is saturated at a high fraction of the LPs.

DOI:10.14753/SE.2017.1972

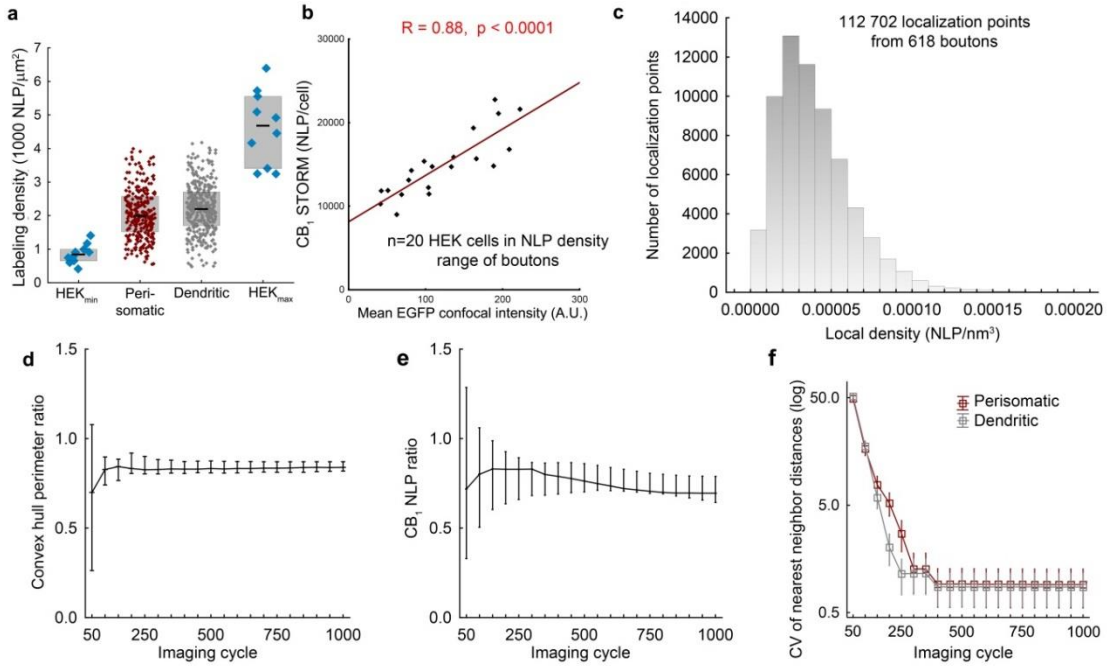

Figure 13. The density of CB_1 LPs on axon terminals is in the dynamic range of the measurement. (a) The density of CB_1 STORM signal is within the range defined by the two HEK cells with the lowest and highest expression levels of EGFP-CB_1. The graph shows raw data (ROIs), and median ± IQR. (b) The correlation between EGFP fluorescence intensity and anti-CB_1 STORM NLP in individual HEK cells is highly linear within the population of transfected HEK cells within the STORM density range defined as the mean ± SD of the mean endogenous CB_1 STORM density on interneurons. (c) Histogram of local STORM signal densities in spheres of 50 nm radius around each LP of the CB_1 STORM images of axon terminals. (d) The perimeter of a 2D convex hull fitted on the CB_1 STORM LPs of each axon terminal was calculated using LPs from the first n imaging cycles. Mean ± 95% confidence interval of the mean of 6 dendritic interneurons (normalized to the mean of perisomatic cells) is shown as a function of n. (e) The same approach was used to show the difference in CB_1 NLP between cell types. (f) The CV (%) of nearest neighbor distances within the CB_1 LPs detected in the first n cycles on each bouton (median ± IQR) is shown as the function of n. The high initial variance (note the logarithmic scale) which is later reduced and constant reflects undersampling of the receptors only in the first 400 cycles (Dudok et al. 2015).

Finally, we have tested whether the number of camera frames captured for the reconstruction of each STORM image is sufficient to reliably determine the density of presynaptic CB_1 receptors on axon terminals. Figure 13d-e show the difference in bouton perimeter and CB_1 NLP between the two interneuron subtypes, calculated from the LPs detected during the first n cycles of imaging. In both cases, the cell type-specific differences shown earlier (Figure 12b-c) were statistically significant already after a few 100s of cycles, and remained highly constant at late phases of the imaging,

indicating that the conclusion of the experiment is independent of the length of imaging. The images were also suitable to probe nanoscale CB_1 distribution, as the CV of nearest neighbor distances between LPs was constant after the initial phase of imaging (Figure 13f). These results indicate that the imaging parameters used throughout the study allow detecting a sufficiently large fraction of endogenous CB_1 without saturation, enabling the quantitative investigation of nanoscale molecular distribution.

4.3.3. Nanoscale distribution of CB_1 on the membrane of GABAergic axon terminals

The similar density of CB_1 receptors on the boutons of both PtINs and DtINs is in apparent contradiction to the higher efficacy of cannabinoids on perisomatic inhibition, suggesting that the abundance of presynaptic CB_1 receptors per se is not the main factor setting the cannabinoid sensitivity of synapses. Indeed, while glutamatergic synapses contain considerably lower level of CB_1 receptors compared to GABAergic synapses (Katona et al. 2006; Marsicano and Lutz 1999), behavioral effects of cannabinoid administration are mostly mediated by CB_1 receptors on glutamatergic axon terminals (Monory et al. 2007), and the G-protein mediated signaling downstream to CB_1 is also higher in excitatory cell types (Steindel et al. 2013). Can a different efficacy of CB_1 also explain the subtype-specific differences in cannabinoid signaling between GABAergic interneurons?

To date, we are not aware of any studies revealing details on the specific pharmacology and G-protein coupled signaling of CB_1 on perisomatic and dendritic inhibitory synapses. On the other hand, the nanoscale distribution of CB_1 in relation to active zones could also contribute to increased cannabinoid sensitivity of perisomatic interneuron synapses. Regulation of synaptic transmission by CB_1 occurs through the plasma membrane-delimited inhibition of VGCCs (Herlitze et al. 1996; Wilson and Nicoll 2001), and it is likely that only calcium channels in the vicinity of the calcium sensors can trigger vesicle release (Chen et al. 2015; Eggermann et al. 2012). Thus, the domain within which the activation of CB_1 can affect neurotransmitter release may be limited to the vicinity of VGCCs coupled to the release sites. The reported diffusion coefficients for GPCRs in plasma membranes is typically in the 10^{-9} cm^2/s range, regardless of native, oligomerized, or ligand-bound states (Herrick-Davis et al. 2013).

Based on single-particle-tracking of GPCRs and these diffusion coefficients, the estimated domain size of a GPCR signaling unit is about 150-200 nm (Daumas et al. 2003). Indeed, previously it has been suggested that CB_1 is enriched in a perisynaptic annulus at GABAergic axon terminals (Nyiri et al. 2005). Thus, we have aimed to investigate the nanodomain-specific abundance of CB_1 at synapses of perisomatically- and dendritically targeting terminals.

In contrast to electron microscopy, STORM does not allow the direct visualization of synapses. Thus, to study the synapse-related nanoscale distribution of CB_1, we have utilized immunostaining to label synaptic active zones. The presynaptic active zone protein bassoon is involved in the targeting of VGCCs to the synaptic active zone in various synapses (Frank et al. 2010; Nishimune et al. 2012; Richter et al. 1999; tom Dieck et al. 1998). Moreover, bassoon co-immunoprecipitates with VGCCs, and its molecular abundance is correlated to the quantity of calcium channels in synaptosomes (Carlson et al. 2010; Wilhelm et al. 2014). First, we have tested whether bassoon immunolabeling can visualize GABAergic synapses in our model system (Figure 14). We have filled pyramidal neurons during patch-clamp recordings, and immunostained the sections containing filled cells against CB_1 and bassoon, using secondary antibodies conjugated with activator-reporter dye pairs. Confocal microscopy revealed CB_1-expressing varicosities impinging on the somata (Figure 14a-b) and dendrites (Figure 14d-e) of pyramidal cells. The appositions between the varicosities and the postsynaptic cell are putatively GABAergic synapses. Indeed, on dual-channel STORM images, clusters of bassoon labeling were visualized inside the CB_1-positive varicosities, exactly at the contact sites with the biocytin-labeled profiles (Figure 14c,f). Together with the immunogold electron microscopy evidence for the targeting of bassoon to presynaptic active zones, this striking specificity of bassoon STORM labeling to contact sites enabled us to use bassoon as a synaptic marker in the forthcoming experiments (Richter et al. 1999). While the dual-channel STORM imaging approach allows the precise labeling of the position of synaptic active zones together with the measurement of extrasynaptic CB_1 LP numbers and positions on the same axon terminal, it is important to note that crosstalk between channels and the applied crosstalk subtraction algorithm makes quantification unreliable in areas where signals from both channels may overlap, i.e. inside synaptic active zones.

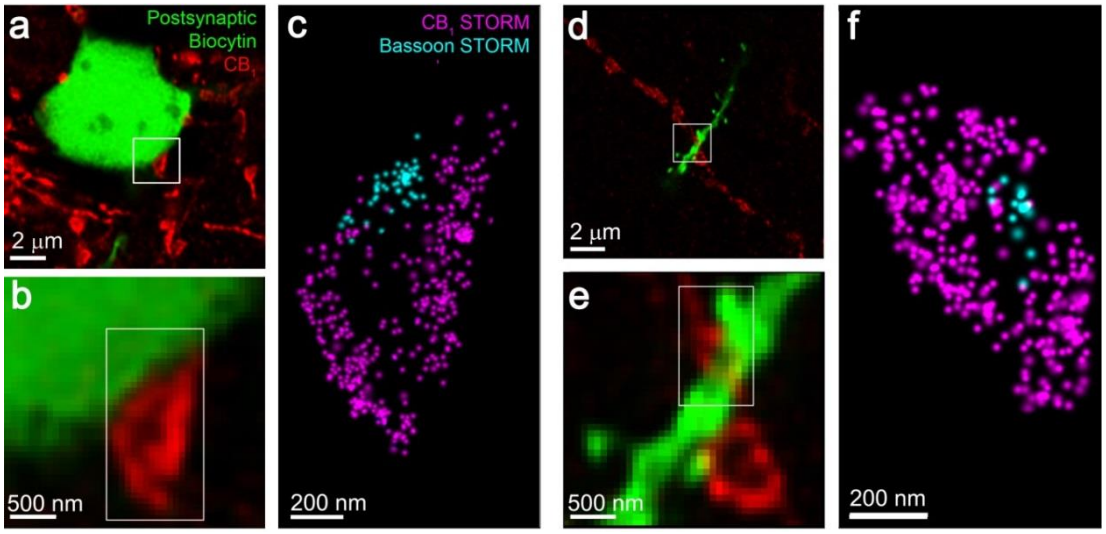

Figure 14. Bassoon STORM labeling labels synapses in CB_1-expressing axon terminals. (a) Confocal image of the cell body of a filled CA1 pyramidal cell and adjacent CB_1-expressing varicosities. (b) Enlarged view of the boxed region illustrates the close contact between the axon terminal and the postsynaptic cell. (c) Dual-channel STORM image of CB_1 and bassoon immunolabeling reveals the specific accumulation of bassoon STORM signal to the contact site, consistent with labeling of the presynaptic active zone. (d-f) The same approach shows the presence of bassoon at contact sites of dendritically-targeting varicosities. The experiment was replicated in 10 cells from one mouse (Dudok et al. 2015).

Next, we have carried out the same dual-channel STORM experiment on slices containing filled PtINs and DtINs. On the biocytin-labeled axon terminals of electrophysiologically and morphologically characterized interneurons, bassoon immunostaining revealed clusters (Figure 15a-d), similarly to the results shown previously on the inputs of filled pyramidal cells. To test whether there are major cell type-specific differences in the nanoscale distribution of CB_1 in relation to the bassoon clusters, first we have measured the 3D Euclidean distance of each CB_1 LP from the nearest bassoon LP (Figure 15e,g). On average, the CB_1-to-bassoon distances were similar in the axon terminals of PtINs and DtINs (Figure 15i, n = 311 and 141 axon terminals from 10 perisomatic and 10 dendritic cells, Mann-Whitney U test, p = 0.69). However, as CB_1R downstream signaling is confined to the membrane, Euclidean calculations underestimate the actual CB_1-bassoon distance along the plasma membrane of the axon terminal. As this effect depends on the size of the bouton, and the two cell types are different in bouton size (see Figure 12a-b), we sought for a more direct measure for evaluating the nanodomain-specific distribution of CB_1. Exploiting the fact

that CB_1 itself decorates the plasma membrane of axon terminals at high density, the bounding volume of the boutons can be approximated by fitting a convex hull on the CB_1 LPs. Because the convex hull operation discards LPs inside the volume, and only the LPs belonging to the axon terminal are selected (based on the biocytin labeling), the surface of this convex hull can be considered as an estimation of the plasma membrane. Indeed, the majority of CB_1 was found close to the convex hull (79 ± 1% and 81 ± 1% of LPs within 200 nm 3D distance from the convex hull surface, n = 280 and 141 perisomatic and dendritic axon terminals, respectively).

To obtain more relevant data on CB_1-bassoon distance, we have measured the length of the shortest path between LPs on the surface of the convex hull fitted on the CB_1 channel. However, in agreement with the Euclidean distance measurements, the mean surface distance of CB_1 LPs from bassoon LPs was similar between cell types (Figure 15i, n = 33 and 22 axon terminals from 8 perisomatic and 5 dendritic cells, Mann-Whitney U test, p = 0.31). Note, that while both the Euclidean and surface distances were measured from data from the same experiment, the number of analyzed boutons is lower for surface distances, as due to computational limitations, only axon terminals with simple convex morphology and a single bassoon cluster were included. Importantly, as the STORM image represents an optical section of the axon terminal, not all faces of the convex hulls represent actual surface areas of the bouton, and thus, measurements obtained with this method are approximative. Axon terminals with large convex hull faces representing false surfaces were discarded from the analysis.

DOI:10.14753/SE.2017.1972

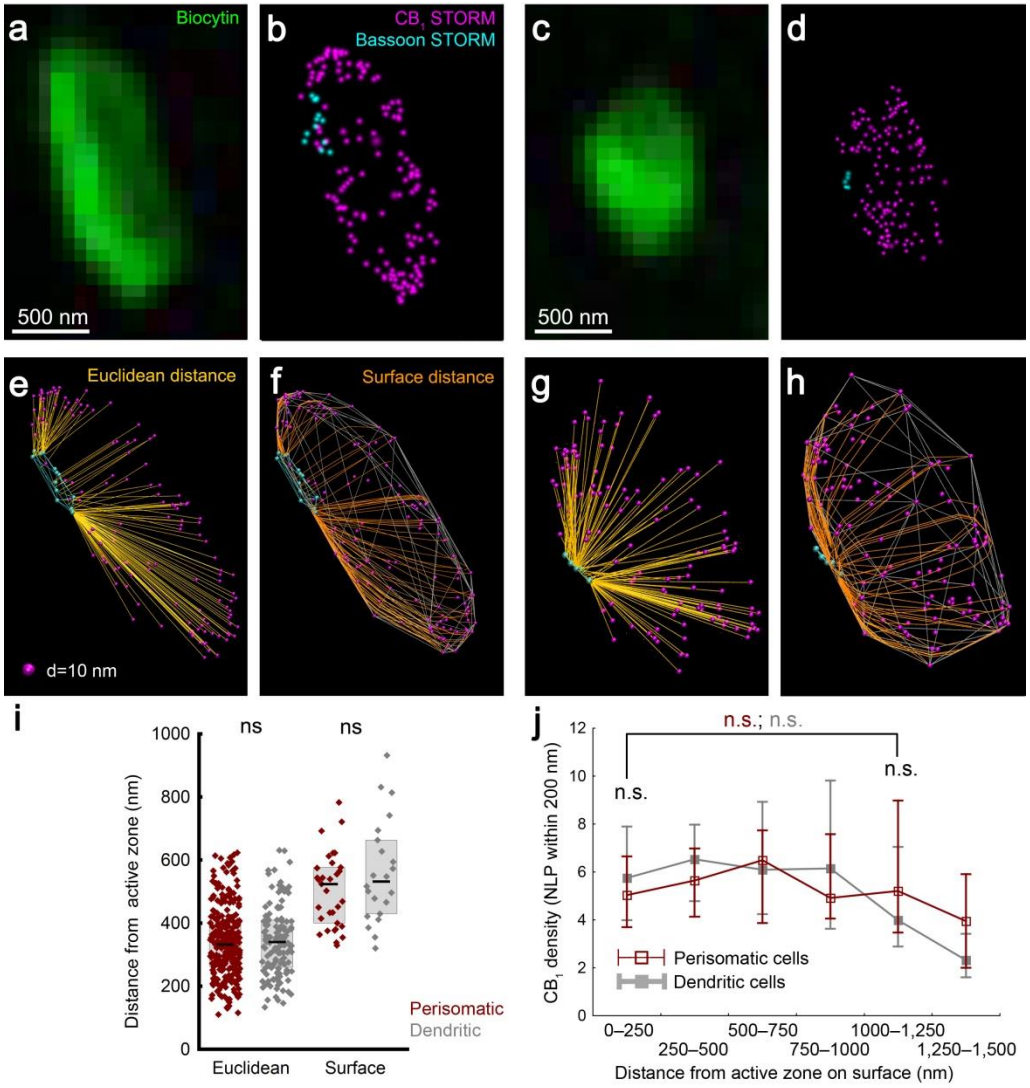

Figure 15. Homogenous distribution of CB_1 on the surface of axon terminals. (a-b) Perisomatic interneurons were filled with biocytin, immunostained against CB_1 and bassoon, and imaged using dual-channel STORM. While CB_1 labeling decorated the entire surface of the bouton, bassoon labeling was restricted to clusters at the edge of axon terminals. (c-d) The same approach was used to label axon terminals of DtINs. (e-h) Three-dimensional renderings of the optical sections of two axon terminals showing the CB_1 and bassoon LPs, together with the trajectories used for distance measurements (yellow), and the convex hull fitted on the CB_1 points (silver). (i) The mean distance of CB_1 from bassoon was similar between axon terminals of PtINs and DtINs, measured either as Euclidean or surface distance. The graph shows raw data (boutons) and median ± IQR. (j) The spatial density of CB_1 LPs, measured at random points of the surface of the convex hull (median ± IQR), was similar between cell types, and was independent of the distance from bassoon-labeled active zones (Dudok et al., 2015).

To determine if CB_1 is specifically enriched in the proximity of synaptic active zones, we sought to directly measure the density of LPs on the surface defined by the convex hulls. Measurement points were placed at random positions on each triangular

face of the convex hull at a high density to uniformly cover the entire surface. Then, the number of CB_1 LPs within a given distance (200 nm, which is larger than the separation between measurement points) was determined for each point, together with the surface distance of the given point from the nearest bassoon LP. Thus, by pooling measurement points into bins, we could estimate the average density of CB_1 at the surface of the convex hulls (representing optical sections of the axon terminals) at certain distances from active zones (Figure 15j). Contrary to our expectations, we have found that the surface density of CB_1 near synaptic active zones was identical between PtINs and DtINs (n = 33 and 22, respectively, p = 0.86, Mann-Whitney U test). Contradicting earlier reports (Nyiri et al. 2005), the density of receptors near synapses was not higher than at more distant membrane parts of boutons (p = 0.64 and 0.28 for perisomatic and dendritic cells, respectively). This contradiction might be the consequence of the interfering effects of bassoon signal at active zones, thus, the measurement of CB_1 density is not reliable inside or in the immediate vicinity of bassoon clusters. Altogether, these data suggest that CB_1 receptors cover the extrasynaptic membrane of GABAergic interneuron axon terminals homogenously, with similar density between subtypes of CB_1-positive interneurons. Therefore, the number and nanodomain-specific positioning of receptors is not likely to be under precise regulation, and is not likely to underlie cell type-specific alterations in the cannabinoid sensitivity of synaptic transmission.

4.4. Organization of presynaptic active zones in CB_1-positive axon terminals

4.4.1. Nanoscale distribution of bassoon STORM labeling

The endocannabinoid system regulates GABA release by inhibiting the function of presynaptic molecules that promote vesicle fusion, such as VGCCs and active zone proteins like RIM1α (Chevaleyre et al. 2007; Szabó et al. 2014). The degree of overall inhibition should depend not only on the number of activated receptors, but also on the number of effector molecules to be controlled by those receptors. The observation that CB_1 receptor densities are uniform between cell types lead us to hypothesize that a difference in the ratio of receptor and effector molecules can underlie the difference in cannabinoid sensitivity. But how to measure the number of relevant effector molecules to be controlled by CB_1? The contribution of different downstream pathways to short-

or long-term, tonic or phasic forms of synaptic plasticity in specific types of synapses is partially understood (see 1.1.3). However, as shown in glutamatergic synapses, the size of presynaptic active zones correlates tightly with release probability, the amplitude of calcium transients, and also with the abundance of VGCCs and RIM proteins (Holderith et al. 2012). Thus, active zone size can serve as a proxy to measure the potency of the axon terminal for vesicle release. As bassoon expression selectively labels presynaptic active zones, we have performed single-channel STORM imaging of bassoon in labeled axon terminals of identified interneurons (Dani et al. 2010; Richter et al. 1999; tom Dieck et al. 1998; Wilhelm et al. 2014).

Consistently with the active zone-restricted distribution of bassoon, STORM images of anti-bassoon immunostaining show the accumulation of bassoon in distinct puncta near the edge of the axon terminals (Figure 16). Unlike in the case of dual-channel STORM, the lack of crosstalk and crosstalk-subtraction allows uncompromised quantification of the distribution of bassoon in this experiment. Because of the conspicuous accumulation of bassoon in multiple spots, we sought to assess the spatial clustering of STORM signal in a quantitative manner. To this end, we have applied DBSCAN clustering on the coordinates of bassoon LPs inside each axon terminal (Ester et al. 1996). This algorithm identifies clustered points based on local density, without a pre-defined number of clusters, while localization points present at low density are treated as noise. Typically, multiple clusters were identified on each axon terminal (Figure 16c,f), in agreement with electron microscopic evidence showing multiple anatomical release sites at boutons of CB_1-expressing interneurons in the hippocampus (Biró et al. 2006). DBSCAN removed ~20% of LPs as noise. As these points are isolated from the clustered labeling, and there is no evidence for bassoon to be present and functional outside release sites, we found the exclusion of noise points from the analysis justified. To overcome the liability from arbitrarily setting clustering parameters, we have replicated the results with a wide range of parameter settings with the same conclusions (not shown).

DOI:10.14753/SE.2017.1972

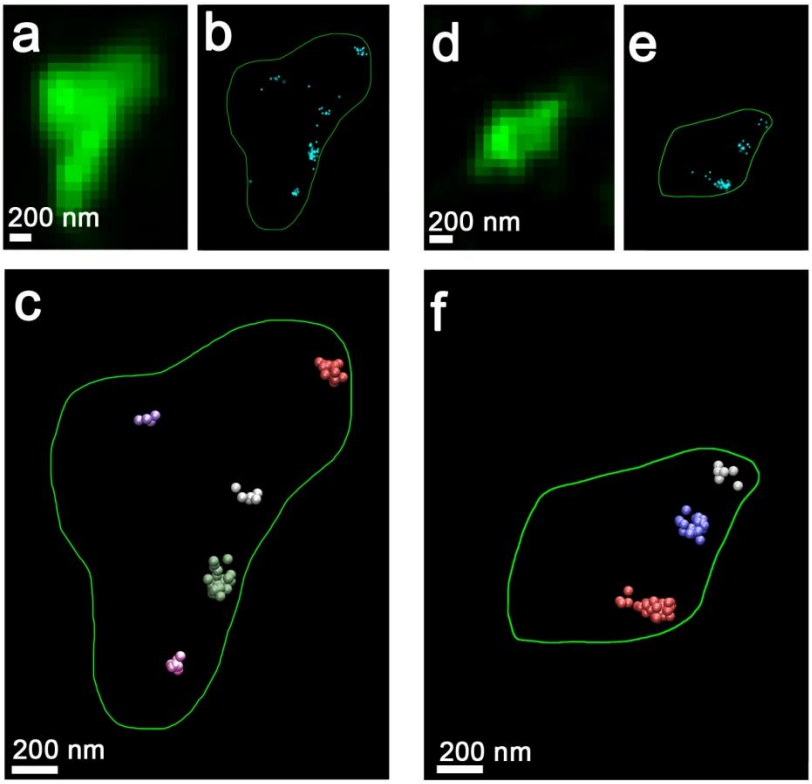

Figure 16. Bassoon STORM labeling in identified axon terminals exhibits clustered distribution. (a) Confocal image of a biocytin-positive axonal varicosity of a CB_1-expressing PtIN. (b) STORM image of single-channel bassoon immunostaining in the area of the axon terminal (green outline) shows clustered appearance. (c) Three-dimensional rendering of the bassoon LPs of the same axon terminal after spatial clustering with the DBSCAN algorithm. LPs belonging to clusters are color-coded for cluster membership, LPs classified as noise are hidden. (d-f) The same strategy revealed clusters of bassoon labeling in axon terminals of DtINs (Dudok et al., 2015).

Despite the larger size of perisomatic axon terminals (see Figure 12), axon terminals of both PtINs and DtINs contained similar numbers of bassoon LPs (Figure 17a, n = 349 and 374 boutons from 10 perisomatic and 12 dendritic cells, respectively, Mann-Whitney U test), which is in stark contrast with the difference in CB_1 NLPs measured in a separate single-staining experiment (Figure 17b, two-sample Kolmogorov-Smirnov test). However, after spatial clustering of the bassoon LPs, we have detected a higher number of clusters in perisomatic axon terminals (Figure 17c). Consequently, the size of individual clusters was smaller, indicating a more fragmented nanoscale organization of the presynaptic active zone in perisomatic synapses (Figure 17d).

DOI:10.14753/SE.2017.1972

4.4.2. Cell type-specific alterations in local CB_1 receptor to effector ratio

This observation, together with the previously established homogenous distribution of CB_1 receptors across the plasma membrane of axon terminals, lead us to hypothesize that individual presynaptic active zones of PtINs express an increased local ratio of CB_1 and bassoon LPs. To test this hypothesis, we have returned to the data set obtained from dual-channel CB_1-bassoon STORM experiments to measure the distance of CB_1 LPs from active zones. As discussed earlier, the distance within which CB_1 can affect downstream targets is not precisely known, but can be estimated in the range of 150-200 nm (see 4.3.3). Thus, if the abundance of bassoon is similar between perisomatic and dendritic synapses, but there are more CB_1 receptors within the relevant distance from bassoon due to the more fragmented distribution of bassoon labeling, the local receptor to effector ratio will also be higher. Indeed, we have found that there are up to 50% more CB_1 LPs within a given distance limit from bassoon at perisomatic synapses (Figure 17e, n = 80 randomly selected boutons per cell type, two-sample Kolmogrov-Smirnov test, see the rationale for the downsampling later). As indicated by the uniform magnitude of difference across any distance limit, this difference is unlikely to be the consequence of a preferential synapse-associated targeting of CB_1, but rather result from the fragmented positioning of active zones paired with homogenous CB_1 distribution.

DOI:10.14753/SE.2017.1972

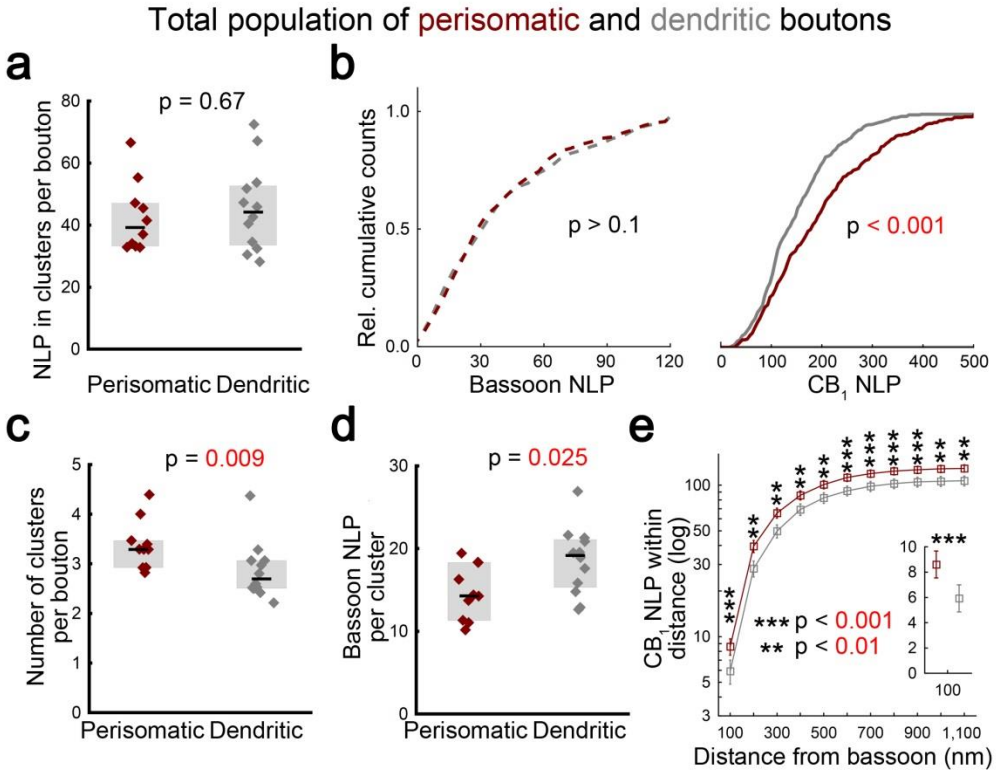

Figure 17. Fragmented active zone architecture results in higher CB_1 receptor to effector ratio in axon terminals of perisomatically targeting interneurons. (a) Quantification of single-channel bassoon STORM labeling in biocytin-labeled axon terminals of PtINs or DtINs. (b) Cumulative histograms comparing bassoon- and CB_1-content of perisomatic and dendritic axon terminals (recorded in separate single-channel STORM experiments, data in right panel is replotted from Figure 12c). (c) Perisomatic axon terminals contain more clusters of bassoon STORM labeling. (d) Individual clusters in perisomatic axon terminals contain fewer bassoon LPs compared to terminals of DtINs. (e) In dual-channel STORM images, the number of CB_1 NLP within any given distance limit from bassoon is higher in perisomatic axon terminals (log scale, median ± IQR, from the same data as Figure 15i, insert shows results for the 100 nm distance limit with linear scale). Box plots show raw data (mean values of cells) and median ± IQR (Dudok et al., 2015).

An alternative explanation of the higher number of CB_1 within a distance limit from bassoon could be the larger size, and the larger CB_1 content of perisomatic axon terminals. To directly test whether the observed alterations reflect true cell type-specific molecular differences, or are just emergent features of larger axon terminals of perisomatic interneurons, we have analyzed an identically sized bouton population from both cell types. To generate this sample, 80-80 axon terminals of both cell types were selected in a manner that guaranteed both random sampling and identical size distribution of axon terminals (see Methods). Such a sample was generated from the

single-channel CB_1 and bassoon STORM experiments, and the dual-channel CB_1-bassoon STORM experiment as well. The n = 80 per group sample size was selected as the highest n that could return a subpopulation of virtually identical size distribution of axon terminals in both cell types (two-sample Kolmogorov-Smirnov test, Figure 18a). To maintain comparable statistical power across tests, the same number (80-80) of axon terminals were selected at random, without respect to bouton size, for the analysis presented earlier on Figure 17e.

Comparing the CB_1 and bassoon NLPs within identically sized bouton populations revealed that consistently with our previous results showing identical CB_1 density between cell types, axon terminals of both cell types contained the same amount of CB_1 LPs, and the distribution of CB_1 NLP between individual axon terminals was identical (two-sample Kolmogorov-Smirnov test, Figure 18b). On the contrary, but in agreement with previous results showing that larger perisomatic terminals expressed the same amount of bassoon as smaller dendritic boutons, axon terminals of DtINs contained more bassoon LPs compared to perisomatic boutons of the same size (Figure 18b). Further in line with previous observations, the number of bassoon clusters per axon terminal was similar between cell types (Figure 18c), resulting in smaller size of individual clusters in axon terminals of PtINs (Figure 18d). Are these smaller active zones surrounded by the same number of CB_1 receptors? As expected, identically sized axon terminals with identical number of bassoon clusters and homogenous distribution of CB_1 resulted in identical number of CB_1 LPs within any distance limit from bassoon in both cell types (Figure 18e). Altogether, these results confirm the cell type-specific, bouton-size independent difference in the nanoscale architecture of bassoon-positive active zones, and demonstrate the increased CB_1 receptor to bassoon ratio at presynaptic active zones of PtINs.

DOI:10.14753/SE.2017.1972

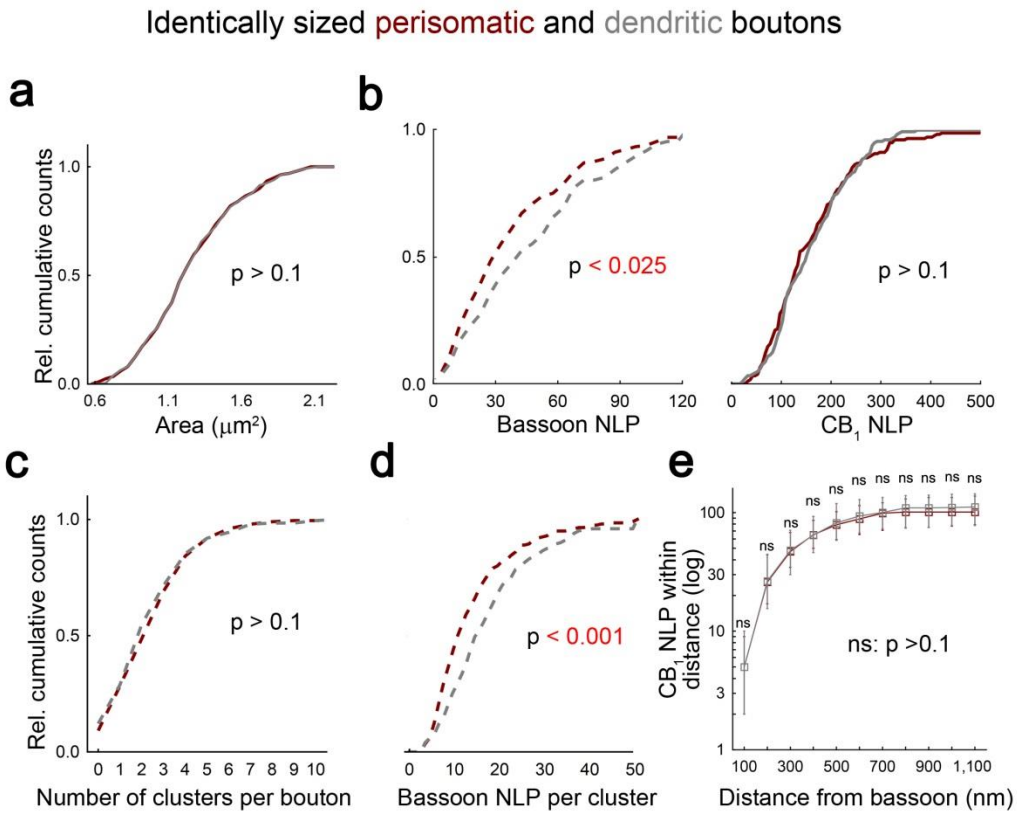

Figure 18. Nanoscale active zone architecture is determined by cell type, not by axon terminal size. (a) To separate the cell type-specific and bouton size-regulated differences between interneurons, subsamples of boutons with identical size distribution were generated. (b) In identically sized boutons, DtINs contained more bassoon, but the same amount of CB_1 LPs compared to perisomatically-targeting cells. (c) The number of clusters was similar in identically sized axon terminals of both cell types. (d) Individual clusters of bassoon STORM labeling contained fewer LPs in perisomatic boutons. (e) The nanoscale anatomical organization of bassoon and CB_1 resulted in identical number of CB_1 LPs within a given distance limit from bassoon in identically sized bouton populations. Graph shows median ± IQR (Dudok et al., 2015).

The integrated analysis of results from single-channel and dual-channel STORM experiments revealed that terminals of PtINs, the average cluster comprises fewer copies of bassoon compared to DtINs, while it is surrounded by the same density of CB_1 receptors. This configuration leads to an increased (by ~45%) putative ratio of CB_1 receptors and their downstream effectors at perisomatic synapses, which might explain the increased sensitivity to endogenous and exogenous cannabinoids of PtIN to pyramidal cell connections (Lee et al. 2010a). On the other hand, due to the larger size of boutons and the higher number of bassoon clusters within, perisomatic axon

terminals can be equally competent to release GABA when free from cannabinoid control.

4.5. Dynamic reorganization of CB_1 distribution on agonist application

4.5.1. Effects of endocannabinoids on CB_1 localization

Thus far, we have determined the principles underlying steady-state distribution of CB_1 receptors, showing homogenous density of CB_1 across the extrasynaptic plasma membrane of GABAergic axon terminals. After activation by binding of a ligand, GPCR signaling is terminated by targeting the receptors to endocytic domains, leading to internalization (Moore et al. 2007). Thus, we have predicted that increased levels of endogenous or exogenous cannabinoid agonists may lead to reorganization, potentially revealing separate functional and reservoir pools of CB_1 on axon terminals. To test this hypothesis, we first investigated nanoscale CB_1 distribution with the cell-specific STORM approach developed earlier, after pharmacologically elevating the levels of endocannabinoids in slices. We have focused these experiments on PtINs to avoid heterogeneity in sampling, assuming that CB_1 internalizations will be governed by similar principles as in DtINS, because previous results did not uncover any differences in the density or distribution of CB_1 between interneuron subtypes.

Incubation of acute brain slices with 100 nM JZL184 (JZL), a selective inhibitor of MGL, or with 1 μM PF3845 (PF), a FAAH inhibitor, doubles the levels of 2-AG and anandamide, respectively, by preventing their enzymatic degradation (Lee et al. 2015). After preincubation with vehicle (DMSO) or inhibitors for 40 minutes, PtINs were patched, filled with biocytin, and processed for CB_1 STORM imaging as described earlier (Figure 19a). Treatment with JZL or PF did not affect the area of axon terminals compared to vehicle-treated slices (n = 3, 3 and 7 cells, respectively, 22±12 boutons per cell, Kruskal-Wallis ANOVA and median test, p = 0.0961 and 0.2292 between DMSO-JZL and DMSO-PF, respectively). Surprisingly, treatment did not affect CB_1 NLP on the axon terminals (Figure 19b).

DOI:10.14753/SE.2017.1972

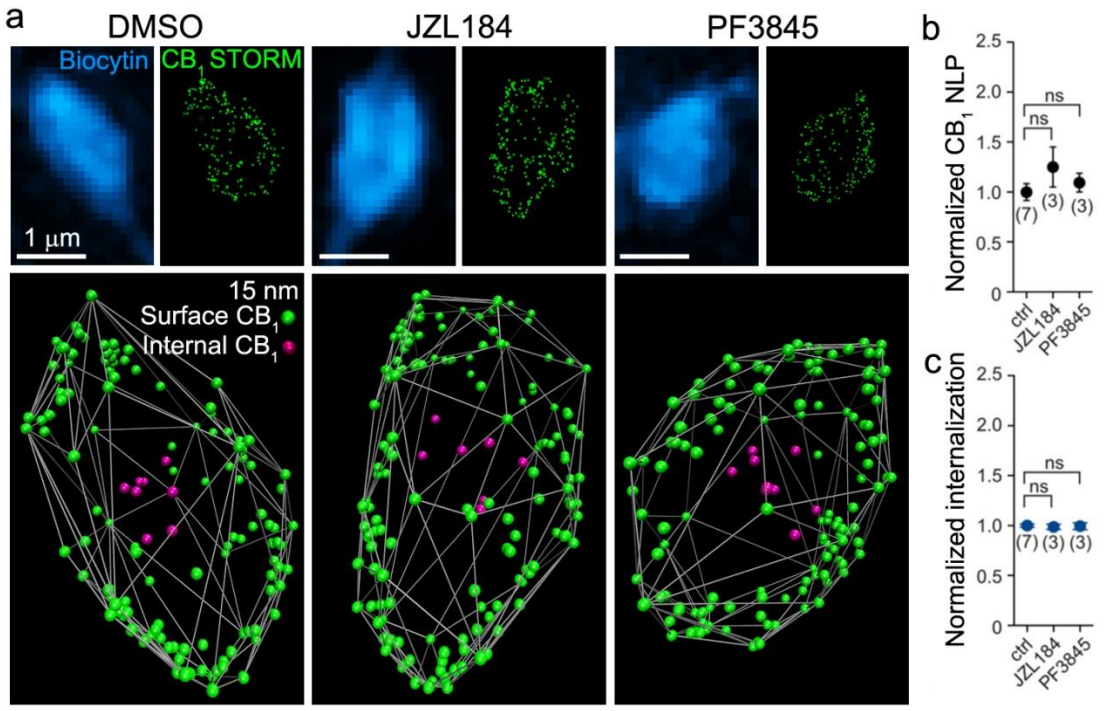

Figure 19. The membrane expression of CB_1 is not affected by increased levels of endocannabinoids. (a) Biocytin confocal and CB_1 STORM images of optical sections from axon terminals of individually filled PtINs from slices acutely treated with vehicle or with JZL or PF, inhibitors of endocannabinoid-degrading enzymes to increase tissue levels of 2-AG or anandamide, respectively. Surface and internal CB_1 LPs were identified solely for visualization purposes by setting a threshold for the internalization index of individual LPs. The edges of the convex hull fit on the CB_1 signal is indicated by silver lines. (b) Acute elevation of endocannabinoid levels did not alter CB_1 NLP on axon terminals. (c) Treatment had no effect on internalization index of CB_1 LPs (determined from the distance of LPs from the center of mass of the bouton). Mean values per cell were normalized to the mean of control cells, ns indicates $p > 0.5$ between groups, number of cells are indicated in parentheses, error bars represent SEM (Lee et al. 2015).

The unaltered total number of CB_1 receptors on individual axon terminals indicates that acute elevation of endocannabinoid levels is not leading to degradation of CB_1 receptors. This can mean that the treatment does not alter steady-state internalization, or that receptors are removed from the plasma membrane, but are not degraded or transported away from the axon terminal within the time frame of the experiment. To differentiate between these two possibilities, we sought to determine the effect of treatment on the surface versus internal localization of CB_1 receptors. The distance of each CB_1 LP from the center of mass of all LPs of the axon terminal is sensitive to a shift of LPs towards the center of the bouton. However, this distance greatly depends on

the size of the given axon terminal. To allow comparison of different axon terminals, we have calculated an internalization index (distance of LPs from the center of mass over the radius of the bouton determined from the confocal image), the value of which would approach 0 if all LPs are in the center of the bouton, and approach 1 if all LPs are on the surface. After treatment with JZL or PF, the mean internalization index of boutons was not changed (Figure 19c), thus, we cannot detect an increase in the endocytosis of CB_1 upon acutely increased levels of endocannabinoids in the tissue.

4.5.2. Effect of exogenous THC on CB_1 localization

The results showing no reorganization of CB_1 receptors upon MGL inhibition are surprising, because chronic MGL blockade has been shown to inhibit CB_1–mediated LTD of GABAergic synapses (Schlosburg et al. 2010). One possible explanation for this contradiction is that the duration of preincubation with drugs in the previous experiment is too short compared to the time scale of the dynamics of surface CB_1 density. To robustly test the long-term changes in presynaptic CB_1 expression at GABAergic axon terminals, we have turned to an in vivo animal model. Repeated exposure to the phytocannabinoid CB_1 agonist THC is also known to induce behavioral and functional tolerance for CB_1 agonists, while a single injection has no such effect (Bass and Martin 2000; Hoffman et al. 2007; Varvel et al. 2005). Thus, we have carried out an established chronic THC administration protocol by injecting mice intraperitoneally with 10 mg/kg THC twice daily for 6.5 days (Bass and Martin 2000). After the last injection, mice were allowed to recover for one additional day, which ensures that THC is cleared from the brain, and thus, the chronic effects of THC can be studied separately from acute effects (Hoffman et al. 2007).

To assess the reorganization of presynaptic CB_1 receptors at GABAergic axon terminals, slices were cut from vehicle- and THC-treated mice, and PtINs were recorded and filled. Consistently with the reported loss of CB_1 radioligand binding from the hippocampus after THC exposure in mice and regular cannabis smoking in humans (Hirvonen et al. 2012; Long et al. 2013), levels of CB_1 immunostaining were dramatically reduced throughout the hippocampus of slices obtained from THC-treated compared to control mice (Figure 20). Moreover, and in contrast to the homogenous distribution of CB_1 on axon terminals in control mice, the extremely weak membrane

labeling in THC-treated samples was accompanied by the appearance of punctate labeling inside boutons, which might correspond to endocytotic structures.

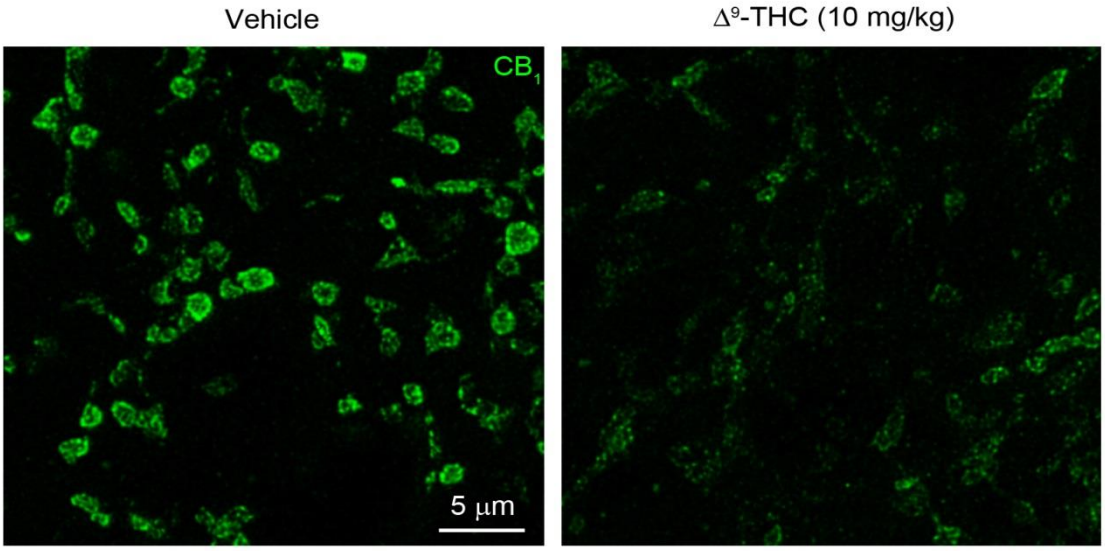

Figure 20. Reduction in CB_1 immunoreactivity in the hippocampus of THC-treated mice. High-power maximal intensity z-projections of deconvolved confocal images from the CA1 pyramidal layer in the hippocampi of control mice and mice treated with chronic THC injections. Note the smooth, plasma membrane-like labeling on putative GABAergic axon terminals in control sections, which is greatly reduced in intensity, and replaced by a more punctate pattern in THC-treated samples. Representative images were recorded and modified identically.

To allow reliable quantitative imaging of CB_1 distribution in THC-treated samples, we have used a novel CB_1 antibody with superior sensitivity for immunostaining samples containing filled interneurons for cell-specific STORM (Dudok et al. 2015). On the axon terminals of PtINs, CB_1 STORM LPs covered the surface in high density (Figure 21a-b), as illustrated by 3-dimensional rendering of LPs and the convex hull fit on them (Figure 21c). Strikingly, in cells filled in slices from THC-treated mice one day after the last injection, the CB_1 STORM signal no longer outlined the biocytin-containing axon terminals clearly (Figure 21d-e). However, the low density of CB_1 LPs still detected on the surface was adequate to fit convex hulls which faithfully represented the shape of the axon terminals (Figure 21f), indicating that CB_1 receptors were not completely removed from the plasma membrane. In addition to the low-density surface labeling, clusters of LPs were observed inside the convex hulls, unlike in cells from vehicle-treated mice.

DOI:10.14753/SE.2017.1972

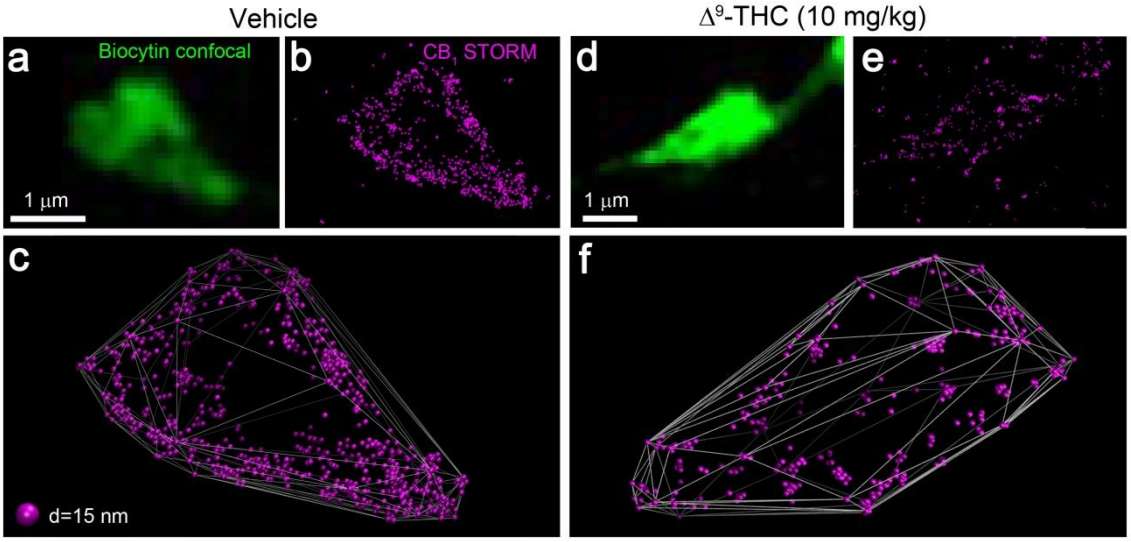

Figure 21. Chronic THC treatment leads to remodeling of CB_1 distribution. (a) Confocal image of an optical section from an axon terminal of an identified PtIN filled in a section from vehicle-treated mouse. (b) Correlated CB_1 STORM image shows that CB_1 LPs outline the labeled axon terminal. (c) Three-dimensional rendering of CB_1 LPs belonging to the labeled bouton and the convex hull fit on the LPs. CB_1 decorates the surface of the axon terminal. (d-f) The same approach was used to evaluate CB_1 STORM signal after chronic THC pre-treatment. The amount of CB_1 labeling is markedly reduced, and clusters of LPs are detected inside the axon terminals (Dudok et al. 2015).

To quantitatively evaluate the redistribution of labeling, we have measured the NLP and the internalization index of PtIN axon terminals (n = 185 and 117 axon terminals from 3 vehicle- and 2 THC-treated mice, Mann-Whitney U test). The amount of CB_1 labeling per bouton has decreased significantly by 74% after THC treatment (Figure 22a), and this change was accompanied by a significant shift of the remaining LPs from the surface towards the center of the axon terminals (Figure 22b). Together, these results show that chronic treatment with a high dose of THC induces significant reorganization of CB_1 receptors at GABAergic synapses.

Next, we have asked the question whether THC-induced reorganization of CB_1 is reversible. During recovery from THC tolerance, different aspects of cannabinoid tolerance are restored with different time courses. For instance, tolerance for THC-induced hypoactivity is completely restored after 7.5 days, tolerance for antinociception after 11.5 days, impairment of LTP after 14 days, and reduction in brain CB_1 receptors

in human chronic cannabis smokers is restored after 4 weeks of abstinence (Bass and Martin 2000; Hirvonen et al. 2012; Hoffman et al. 2007). Thus, to examine the correlation between behavioral tolerance and molecular reorganization, we have studied recovery after 11.5 days, when the behavioral tolerance (in the tetrade essay) induced by the chronic THC treatment regime we have applied is completely restored, and, as a positive control for recovery, after 6 weeks, when all reports show complete restoration of the endocannabinoid system. After 6.5 days of THC injections as described above, mice were allowed to recover, and PtINs were filled to perform cell-specific STORM imaging of CB_1 immunostaining. After 11.5 days of recovery, the CB_1 NLP in THC-treated mice was still by 35% below the levels measured in the respective controls, treated and housed together during the full duration of the experiment (Figure 22a, n = 283 and 113 boutons from 3 vehicle- and 3 THC-injected mice, respectively, Mann-Whitney U test). Increased internalization of CB_1, however, was no longer evident, as the internalization index was similar in both groups (Figure 22b). After the longer recovery period of 6 weeks, both CB_1 NLP and the internalization index was undistinguishable between treatment groups (Figure 22, n = 113 and 92 boutons from 2 vehicle- and 3 THC-injected mice, Mann-Whitney U test).

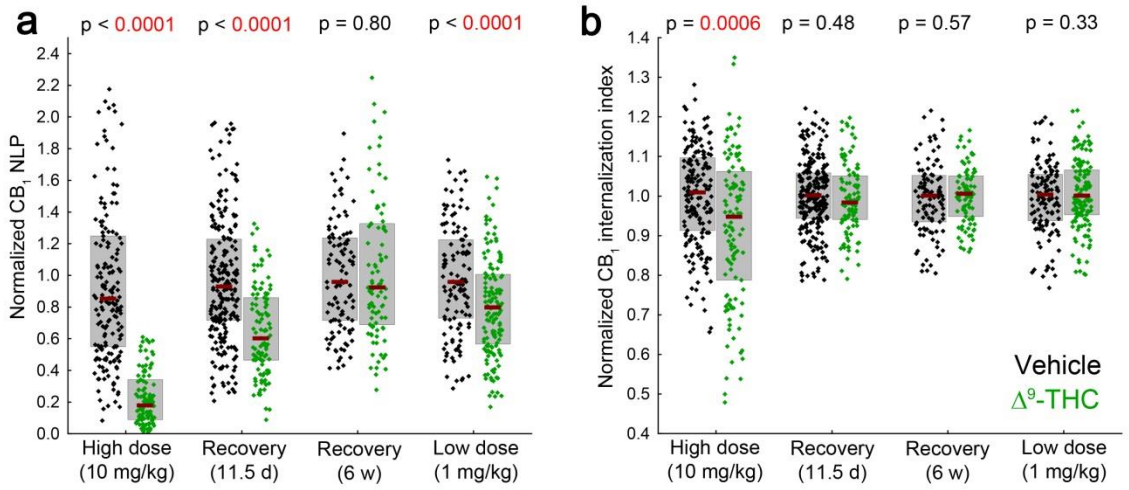

Figure 22. Recovery and dose-dependence of molecular reorganization after chronic THC exposure. (a) The NLP on axon terminals of individually labeled PtINs was determined after THC treatment in four separate experiments, each including vehicle-treated mice for designated controls. Chronic THC injections resulted in a marked loss of CB_1 from axon terminals, which effect recovered only partially within 11.5 days, and completely within 6 weeks. A lower, therapeutically relevant dosing resulted in a lesser degree of reduction in CB_1 NLP. (b) The CB_1 internalization index

was measured on the same axon terminals. Internalization of CB_1 was evident only after high dose THC treatment, and recovered quickly (Dudok et al. 2015).

The 10 mg/kg dose of THC used in the above experiments is considered high, as it has been established for the purpose of inducing tolerance (Abood et al. 1993; Bass and Martin 2000; Oviedo et al. 1993). In humans, peak serum THC levels are approximately 100 ng/ml at 3 hours after smoking cannabis (Heishman et al. 1990; Huestis 2007). In the therapeutic dosing of THC, for instance in the case of Sativex, a combined THC and CBD preparation with indication for multiple sclerosis, a lower serum THC level of 10 ng/ml is targeted to avoid psychoactive effects and the development of tolerance (Karschner et al. 2011; Stott et al. 2013). To test whether the significant rearrangement of CB_1 distribution after chronic treatment with 10 mg/kg THC is prevented when lower, therapeutically relevant doses are administered, we have performed the same experiment with 1 mg/kg dosing, which does not lead to behavioral effects in the tetrad assay (El-Alfy et al. 2010; Varvel et al. 2005). After low-dose treatment, CB_1 NLP on axon terminals of PtINs decreased slightly, but significantly, by 16%, without any noticeable effect on the internalization index (Figure 22, n = 113 and 92 boutons from 2 vehicle- and 3 THC-injected mice, Mann-Whitney U test). Together, these experiments show that chronic effect of exogenous cannabinoid application leads to a dose-dependent and reversible loss of CB_1 from the surface of hippocampal GABAergic axon terminals, with different time-scale of receptor internalization and degradation.

DOI:10.14753/SE.2017.1972

5. Discussion

In this study, we have validated the use of immunostaining and STORM for the relative quantitative measurement of protein abundance in biological samples at nanoscale, and developed a method for the cell-specific analysis of STORM images in labeled axon terminals of identified neurons. We have applied this approach to show the uniform density of CB_1 cannabinoid receptors across the plasma membrane of perisomatically- and dendritically-targeting interneurons of the CA1 region of the hippocampus. These experiments revealed that the CB_1 content is correlated to the size of axon terminals, and the boutons of PtINs are larger, and contain proportionally more CB_1 compared to DtINs. On the contrary, axon terminals of both cell types contained equal total amounts of bassoon, which was distributed in more individual clusters in PtINs. Synthesizing the results from experiments with single- and double-staining against CB_1 and bassoon, we have found that identically sized PtIN and DtIN axon terminals contain the same number of CB_1 to control smaller active zones in PtINs, and that in the total population of PtIN and DtIN axon terminals, active zones are controlled by more CB_1 in PtINs. Consequently, we conclude that the local nanoscale ratio of CB_1 and downstream effectors is considerably higher in PtIN axon terminals. Finally, we have shown that chronic application of the exogenous cannabinoid agonist THC, but not an acute elevation of the levels of the endocannabinoids anandamide or 2-AG, resulted in a reversible, dose-dependent loss of CB_1 from the surface of axon terminals. Together, these results provide insight into the cell-specific molecular determinants of cannabinoid sensitivity, and the molecular background of cannabinoid-induced impairment of the control of GABA release at hippocampal inhibitory synapses.

5.1. Cell-specific STORM enables relative quantitative nanoscale imaging on axon terminals of identified neurons.

Super-resolution fluorescence microscopy has been recently used fruitfully to study the nanoscale structure of neurons and protein distribution of synapses. In particular, STORM was used to study the axial distance of different pre- and postsynaptic active zone and PSD proteins from the cleft, as well as the trans-synaptic alignment of such proteins (Dani et al. 2010; Tang et al. 2016). The nanoscale clustering of synaptic receptors has also been the subject of extensive research (MacGillavry et al. 2013; Nair

et al. 2013). Both STORM and STED were used to map the synaptic inputs of neurons, to provide quantitative measures of dendritic spine morphology in the healthy brain and in disease, and to uncover unknown structural details of cytoskeletal architecture (MacGillavry and Hoogenraad 2015; Sigal et al. 2015; Wijetunge et al. 2014; Xu et al. 2013).

Although PALM was used to quantify the number of photoconvertible proteins to count genetically labeled postsynaptic scaffolding molecules (gephyrin) at inhibitory synapses, to our knowledge, the use of immunostaining and STORM for quantitative comparisons has never been evaluated (Maglione and Sigrist 2013; Specht et al. 2013). Because of the stochastic nature of STORM, the number of times each fluorophore label is detected during the imaging is also probabilistic. Therefore, we aimed to test the hypothesis whether the number of localization points (NLP) in a STORM image of a region is correlated to the number of target proteins, which is essential for the use of STORM to compare protein quantity between samples. Our results obtained from HEK cells expressing chimeric CB_1 indirectly suggest that the NLP reports protein concentration over the density range of CB_1 STORM signal on GABAergic axon terminals, when imaging conditions are constant across samples. Importantly, with SMLM, not only the resolution is improved, but also the sensitivity is increased. Contrary to intensity based imaging such as widefield, confocal, STED or SIM microscopy, where the SNR is decreased with low density labeling, the SNR for detecting an individual blinking event with SMLM is increased with low labeling density, due to the decreased background intensity and the constant brightness of individual fluorophore images. Therefore, STORM can be especially useful to detect low copy number molecules, if a sufficiently sensitive antibody or other labeling method is available.

To study the nanoscale distribution of CB_1 receptors on axon terminals, we have implemented STORM microscopy in combination with single-cell labeling via patch-clamp recordings. Using this approach, we were able to measure electrophysiological, morphological, and nanoscale molecular features of the same identified neurons. We have demonstrated that immunostaining and STORM can be utilized to compare protein levels, as the CB_1 LP density on axon terminals is above the background and below the

saturation levels of the measurement. However, it is important to note that due to the reliance of our approach on immunostaining in tissue, it is not known whether epitope availability and steric hindrance of antibodies limits the detection of receptors. These factors are more likely to confound labeling in the area of the presynaptic active zone, where the density of proteins is very high (Wilhelm et al. 2014).

Correlated light- and electron microscopy has been available for a long time to study individually labeled neurons, and, theoretically, can be combined with immunogold labeling to solve the problem of imaging nanoscale molecule distribution (Gulyás et al. 1993). However, such experiments are extremely time-consuming, and therefore, to our knowledge, electron microscopy has not been used in such way. With correlated confocal and STORM microscopy, on the other hand, axon terminals of a labeled neuron can be imaged in a matter of minutes. Exploiting the performance of STORM, we have taken images of over 7000 biocytin-labeled axon terminals of 79 electrophysiologically and morphologically characterized interneurons, with a localization precision of 6 nm in the lateral, and 41 nm in the axial dimensions.

5.2. Uniform distribution of presynaptic CB_1 receptors

Surprisingly, and in contrast with receptors of anterograde neurotransmitters, CB_1 receptors were distributed uniformly across the plasma membrane of the axon terminals, and their numbers were strongly correlated to the size of the bouton (Nair et al. 2013; Specht et al. 2013). Importantly, the majority of the receptors were detected on the surface of the axon terminal, and only one tenth were detected intracellularly. These results, together with the high mobility of CB_1 reported in cultured hippocampal neurons, and in contrast with a pervious immunogold electron microscopic study, suggest the free diffusion of the receptors across the extrasynaptic plasma membrane, uncontrolled by anchoring to molecular scaffolds or by endocytosis at steady-state (Mikasova et al. 2008; Nyiri et al. 2005). But why are the axons and axon terminals of CB_1-expressing interneurons covered in CB_1 in such high density? Are all receptors on the surface contributing to the cannabinoid sensitivity of the synapse? To tackle this question, we have examined two subtypes of CB_1-expressing hippocampal interneurons with markedly different sensitivity to endo- and exogenous cannabinoids, and different endocannabinoid tone (Lee et al. 2010a). We have found similar density of receptors on

the axon terminals of both cell types, suggesting that receptor density alone does not determine the strength of functional CB_1-mediated signaling. Supporting this notion, calcium imaging experiments found no correlation between the strength of tonic endocannabinoid-mediated depression of presynaptic calcium currents and the density of receptors on the axon terminal (Lenkey et al. 2015).

5.3. Implications for the cannabinoid control of synapses

If CB_1 density does not explain the potency of cannabinoid signaling, what other factors might be involved? Knockout or mutations of neuroligin 3 or neurexins, adhesion molecules that form transsynaptic bridges through the synaptic cleft, caused an impairment of tonic endocannabinoid signaling (Anderson et al. 2015; Földy et al. 2013; Südhof 2008). Interestingly, CB_1-expressing interneurons displayed a remarkably selective composition of transsynaptic adhesion molecules and their binding partners (Fuccillo et al. 2015). Thus, it is possible that CB_1 receptors in the nanodomains of vesicle release sites are bound to specific molecules that regulate their function, and that only synaptically targeted receptors are competent in regulating release, while extrasynaptic receptors may solely serve as a reservoir pool. However, it is currently not known whether CB_1 is enriched in, or excluded from synapses. Our experiments were not optimal for detecting such organizational rules, as the dual-channel STORM approach utilized in this study is prone to crosstalk, and high-density bassoon labeling of the active zone interferes with the quantitative detection of CB_1. Immunogold labeling against CB_1, using freeze-fractured replica labeling or postembedding immunostaining, detected CB_1 receptors in the synaptic active zones of interneuron axon terminals (Lenkey et al. 2015; Nyiri et al. 2005). These studies, however, did not address the question whether the different cannabinoid sensitivity of PtINs and DtINs correlates with the density of CB_1 in active zones. Therefore, further studies are required to identify the pool of CB_1 receptors controlling vesicle release. Moreover, recent results indicate that different molecular mechanisms might underlie tonic and phasic endocannabinoid signaling. Inverse agonists of CB_1 were capable of increasing the success rate of CB_1-expressing GABAergic synapses above baseline levels, indicating tonic endocannabinoid signaling, whereas neutral antagonists, despite blocking DSI, were ineffective at preventing tonic signaling (Lee et al. 2015). One possible explanation for this observation is that ligand-free activity of the CB_1 receptor

is responsible for the endocannabinoid tone; however, it is hard to explain the observed variability, activity-dependence and synapse-specificity of tonic signaling with bona fide constitutive activity (Kim and Alger 2010; Lee et al. 2010a; Neu et al. 2007). Moreover, in neuroligin 3 knockout mice, tonic, but not phasic endocannabinoid signaling was affected (Földy et al. 2013). Therefore, it is conceivable that transsynaptic interactions would regulate tonic signaling by stabilizing CB_1 in a constitutively active or 2-AG-bound conformation, or trapping constitutively active or 2-AG-bound CB_1 in the synaptic active zone. It remains to be tested whether phasic and tonic endocannabinoid signaling is mediated by the same set of receptors. While tonic endocannabinoid signaling appears to be synapse specific, phasic endocannabinoid signaling at GABAergic synapses is generally not a homosynaptic mechanism. Specifically, i-LTD is proposed to be mediated by 2-AG release from neighboring glutamatergic synapses, and DSI can even spread to neighboring non-depolarized cells (Chevaleyre and Castillo 2003; Wilson and Nicoll 2001). Thus, it cannot be excluded that while synaptic CB_1 can mediate tonic, extrasynaptic receptors mediate phasic endocannabinoid signaling in interneuron axon terminals.

5.4. Different presynaptic active zone architecture in perisomatically- and dendritically-targeting interneurons

We have discovered major differences in the nanoscale active zone architecture of the two interneuron subtypes. A more fragmented distribution of release machinery proteins led to an estimated twofold increase in the local ratio of CB_1 receptors over their downstream effectors in PtINs, which exhibit strong tonic endocannabinoid signaling and high sensitivity to CB_1 agonists. Thus, while both CB_1 receptors and their molecular targets, voltage-gated calcium channels, are mobile at synapses, the relative nanodomain concentration of these molecules near vesicle release sites may determine the efficiency of cannabinoid-induced synaptic regulation (Mikasova et al. 2008; Schneider et al. 2015). The notion that CB_1 activation does not inhibit vesicle release in an all-or-none, but in a gradual manner, is supported by results showing tremendous variability in the baseline failure rate of CB_1-positive synapses, as well as by the fact that continuous firing of the presynaptic cell can override cannabinoid inhibition (Lee et al. 2010a; Losonczy et al. 2004; Neu et al. 2007).

Although the interaction between bassoon and VGCCs has been detected selectively for the CaV2.1 subtype, this has been studied in cell cultures, or in synapses where CaV2.1 is the dominant subtype (Davydova et al. 2014; Frank et al. 2010; Nishimune et al. 2012). Thus, it is currently unknown whether bassoon binds CaV2.2 channels at synapses of CB_1-expressing interneurons. It has been suggested that while there is precise nanodomain coupling between VGCCs and release sites at synapses with CaV2.1, a looser microdomain coupling occurs at synapses with CaV2.2 (Bucurenciu et al. 2008; Eggermann et al. 2012; Hefft and Jonas 2005). Nevertheless, the size of the presynaptic active zone was shown to be tightly correlated with the magnitude of calcium transients in the axon terminals of CB_1-expressing cells, suggesting that components of the active zone tightly regulate calcium signaling even with mobile VGCCs (Holderith et al. 2012; Schneider et al. 2015). As the rate of vesicle fusion is not a linear function of intra-terminal calcium levels, but scales exponentially, it is conceivable that even slight effects on VGCC function can have large functional outcome on the amplitude of postsynaptic currents (Szabó et al. 2014).

5.5. Distinctive features of cannabinoid signaling at GABAergic synapses

The considerable difference in the CB_1 expression level between glutamatergic and GABAergic neurons has been noted for a long time (Katona et al. 2006). However, it is not understood why excitatory synapses use so much less CB_1. In excitatory synapses, DSE is less potent than DSI in inhibitory synapses, but, with long depolarization, can almost completely block neurotransmitter release (Ohno-Shosaku et al. 2001). In cell type-specific knockouts, CB_1 on glutamatergic terminals was involved in most of the behavioral effects of THC, while the deletion of CB_1 from GABAergic terminals left the behavioral responses largely unaffected (Monory et al. 2007). Thus, the low amounts of CB_1 at excitatory synapses result in comparable functional role in controlling neurotransmitter release as the strikingly high density at certain GABAergic synapses. What molecular differences might explain this discrepancy? It has been shown that the downstream G-protein-coupled signaling of CB_1 is different in excitatory and inhibitory neurons, with increased coupling efficiency at glutamatergic synapses (Steindel et al. 2013). Moreover, knockout of neurexins resulted in the diminishment of both tonic and phasic endocannabinoid signaling at glutamatergic synapses, in contrast with the selective effect of neuroligin 3 deletion on tonic signaling at GABAergic synapses

(Anderson et al. 2015; Földy et al. 2013). Thus, it is likely that apart from the molecular differences in the release machinery, G-protein-mediated signaling, and the type of VGCCs, differential nanoscale subsynaptic targeting of CB_1, possibly via interactions with transsynaptic adhesion proteins, contribute to the high efficiency of CB_1 at glutamatergic synapses. This hypothesis, and the role of the higher CB_1 density at GABAergic synapses, remains to be tested.

5.6. Molecular background of cannabinoid tolerance

Although the cannabis plant contains more than 60 cannabinoid and more than 100 terpenoid species that might contribute to the biological effects of marijuana, it has been shown that the psychoactive and behavioral (tetrad) effects are mainly mediated by THC acting on CB_1 (Brenneisen 2007; Huestis et al. 2001; Varvel et al. 2005). The chronic exposure to THC leads to impairment of cognitive and memory functions in rodents and humans (Bolla et al. 2002; Puighermanal et al. 2009; Volkow et al. 2014), the molecular background of which is incompletely understood. Cross-tolerance between THC and endocannabinoids is a likely mechanism, as it has been shown that chronic THC leads to decreased CB_1 levels, and results in impaired endocannabinoid signaling (Hirvonen et al. 2012; Hoffman et al. 2003; Suplita et al. 2008). In the hippocampus, chronic THC was shown to block LTP induction, which may constitute the synaptic background underlying cognitive impairment (Hoffman et al. 2007). Interestingly, in this paradigm, GABAergic, but not glutamatergic transmission was desensitized to inhibition by CB_1 agonists. This role of endocannabinoid-mediated LTD of GABAergic synapses as the major expression mechanism of LTP at excitatory synapses has been confirmed directly in the potentiation of Schaffer collateral synapses, and it is the consequence of the strong contribution of CB_1-expressing interneurons to feedforward inhibition (Basu et al. 2013). As the knockout of CB_1 on GABAergic neurons also leads to the abolishment of hippocampal LTP, it is highly likely that chronic THC impairs hippocampal synaptic plasticity by the desensitization of GABAergic synapses to endocannabinoids (Monory et al. 2015).

To test this hypothesis, we have studied the effect of a chronic THC treatment paradigm which is known to induce behavioral tolerance and reduce synaptic response to cannabinoids in mice. Using STORM on identified axon terminals, we have found an

estimated 75% reduction in the levels of surface CB_1 after treatment with THC. This decrease was accompanied by a 50% increased ratio of internalized receptors, suggesting that agonist-induced endocytosis in axon terminals followed by degradation of internalized receptors leads to the functional blockade of endocannabinoid signaling. This reorganization was specific for the chronic application of exogenous cannabinoids, as acute increase of endocannabinoid levels did not trigger changes.

As discussed earlier, the role of the high level of extrasynaptic CB_1 receptors on GABAergic axon terminals is not understood, and one likely explanation is the function of this population of receptors as a reservoir pool to replenish CB_1 internalized upon agonist binding. Notably, after 11.5 days of recovery from chronic THC, we detected a ratio of internalized receptors equal to baseline, while the total number of receptors was still 35% lower than in control mice. However, significant although incomplete recovery of hippocampal LTP was observed already at 3 days after THC withdrawal (Hoffman et al. 2007). This mismatch between the recovery of functional tolerance and CB_1 levels is consistent with the hypothesis that chronic THC treatment results in the depletion of a reservoir pool of CB_1 by constantly promoting internalization, and after cessation of the treatment, the reservoir pool is filled back relatively slowly by constitutive synthesis and axonal transport of CB_1.

However, our findings showing no decrease in CB_1 levels upon acute elevation of endocannabinoid levels argues against the role of extrasynaptic receptors as a reservoir, because it is counterintuitive that such reservoir population of the receptors would prove adaptive in any physiological process if doubled 2-AG or anandamide concentrations for over an hour did not result in detectable loss of CB_1 (Lee et al. 2015). It cannot be ruled out though that CB_1 distribution in vehicle-treated samples might already reflect a reorganized state compared to the in vivo distribution, as endocannabinoid levels were constantly increasing in acute slice preparations even without the blockade of degradative enzymes.

In glutamatergic synapses, CB_1 levels are considerably lower than in GABAergic terminals, however, it has been demonstrated that CB_1 on glutamatergic terminals is required to mediate some of the behavioral effects of THC in the tetrad assay, while none of the effects were altered by the KO of CB_1 from GABAergic terminals (Katona

et al. 2006; Monory et al. 2007). However, similarly to the recovery of hippocampal LTP, tetrad effects were also significantly but partially recovered after already 4.5 days of withdrawal, and complete recovery lasted for as long as two weeks. These observations suggest that after complete desensitization of synapses with chronic THC, it takes similar amount of time for both synapse populations to functionally recover lost receptors. To specifically test the existence of a potential reservoir pool of receptor on GABAergic, but not on glutamatergic terminals, it would be interesting to see if a less potent chronic treatment regime can result in the loss of CB_1 sensitivity at glutamatergic, but not at GABAergic synapses, and whether a decrease in total CB_1 numbers and increased internalization can be detected before the onset of functional tolerance in GABAergic axon terminals. Our experiment with low dose chronic THC showed slight decrease in total presynaptic CB_1 levels. However, while behavioral studies using the same treatment did not detect behavioral tolerance (suggesting lack of desensitization of glutamatergic synapses for THC), it is not known if this low dose protocol causes impairment of LTP (i.e. desensitization of GABAergic synapses for endocannabinoids).

Taken together, our results demonstrate the dose-dependent, reversible removal of CB_1 receptors from hippocampal GABAergic axon terminals during THC tolerance, which is likely the molecular background of cannabis-induced cognitive deficits. Using lower, therapeutically relevant concentrations did not result in such rearrangement, predicting that the use of low doses of cannabinoids does not necessarily lead to cognitive side effects.

DOI:10.14753/SE.2017.1972

6. Conclusions

STORM super-resolution microscopy, combined with the labeling of single identified neurons during patch-clamp recording, is an efficient approach for the correlated analysis of electrophysiological and morphological features of neurons together with the underlying molecular properties. The NLP in a STORM image is correlated to protein abundance, allowing relative quantitative molecular imaging with a resolution rivalling immunogold electron microscopy (6 nm lateral, and 41 nm axial localization precision).

On the axon terminals of CB_1-expressing interneurons, size of the terminal is a strong predictor of CB_1 content, and PtINs have larger axon terminals with 39% more CB_1 NLP compared to DtINs. The density of CB_1 along the extrasynaptic plasma membrane is uniform and homogenous in both cell types, therefore CB_1 density does not explain the greater cannabinoid sensitivity of PtINs.

The axon terminals of both cell types contain the same levels of bassoon, clustered into more, but smaller individual active zones in PtINs compared to DtINs. In PtIN axon terminals, 49% more CB_1 LPs are found within the active zone nanodomains, which might underlie increased cannabinoid sensitivity and tonic endocannabinoid signaling at these synapses.

Acute elevation of endocannabinoid levels by blocking the degradative enzymes of anandamide or 2-AG does not result in a change in the CB_1 levels of PtIN axon terminals, or in the ratio of internalized receptors. Chronic in vivo THC treatment, however, induces large, 74% reduction in CB_1 NLP on axon terminals of identified PtINs, and increased ratio of internalized receptors. Loss of CB_1 from the surface of interneuron axon terminals is likely the molecular background of THC-induced cannabinoid tolerance and cognitive impairments. The chronic reorganization of CB_1 distribution recovered partially (53% of lost signal was restored) after 11.5 days of THC withdrawal, and complete recovery was reached after 6 weeks. Chronic treatment with low, therapeutically relevant dose of THC induced minor decrease by 16% in presynaptic CB_1 NLP without detectable change in the ratio of internalized receptors.

DOI:10.14753/SE.2017.1972

7. Summary

Endocannabinoid signaling controls neurotransmitter release throughout the central nervous system. Despite the fundamental importance of this phenomenon, the molecular principles determining the strength of endocannabinoid-mediated inhibition of synapses during physiological and pathophysiological processes is not understood. Studying the molecular composition of synapses in a cell type-specific manner has been technically challenging. We have developed a method based on patch-clamp recording, anatomical reconstruction of individual neurons, immunostaining, and correlated imaging using confocal and STORM super-resolution microscopy to reveal cell morphology and quantitative molecular distribution, respectively. This approach uniquely enables the integrated analysis of electrophysiological, morphological, and nanoscale molecular features of individual neurons.

Cell-specific STORM of the CB_1 cannabinoid receptor demonstrated that GABAergic axon terminals are decorated with CB_1 in a homogenous density. Nanoscale cluster analysis of the presynaptic active zone protein bassoon, however, revealed that active zones are more fragmented in perisomatically targeting compared to dendritically targeting interneurons, giving rise to higher local nanodomain ratios of CB_1 and downstream effectors. This difference may explain the higher cannabinoid sensitivity of the synapses of perisomatically targeting interneurons. Next, we have utilized the cell-specific STORM approach to study the remodeling of CB_1 distribution during a pathophysiological process, cannabinoid tolerance. We have found that chronic treatment with THC, the main psychoactive compound of cannabis, resulted in increased internalization, and decreased quantity of CB_1 at axon terminals of individually characterized GABAergic interneurons. This reorganization recovered surprisingly slowly compared to the restoration behavioral tolerance, and was significantly smaller in scale after chronic administration of lower, therapeutically relevant and non-psychoactive doses of THC, and undetectable after acutely elevated levels of endocannabinoids. These results contribute to the understanding of the molecular underpinnings of synaptic cannabinoid signaling and tolerance.

DOI:10.14753/SE.2017.1972

8. Összefoglalás

Az endokannabinoid jelátvitel a központi szinapszisok széles körében szabályozza a neurotranszmitter-felszabadulást. Alapvető jelentősége ellenére az endokannabinoid-mediált gátlás erősségét meghatározó molekuláris szintű szabályozóelvekről keveset tudunk. A szinapszisok molekuláris összetételének sejttípus-specifikus vizsgálatát jelentős módszertani korlátok nehezítették. Egyedi idegsejteken végzett patch-clamp elvezetés és anatómiai rekonstrukció, valamint immunfestés és korrelált konfokális és STORM szuperrezolúciós képalkotás alkalmazásával kifejlesztettünk egy módszert a sejtes morfológia és a kvantitatív molekuláris eloszlás együttes vizsgálatára. Ez a megközelítés egyedülálló módon lehetővé teszi az egyedi neuronok elektrofiziológiai, morfológiai, és nanoskálájú molekuláris jellemzőinek integrált elemzését.

A CB_1 kannabinoid receptor sejt-specifikus STORM vizsgálatával kimutattuk, hogy a CB_1 homogén sűrűségben fedi a GABAerg axonterminálisok felszínét. A preszinaptikus aktív-zóna alkotó bassoon fehérje nanoskálájú klaszter-analízise ezzel szemben felfedte, hogy az aktív zónák nagyobb mértékben fragmentáltak periszomatikus gátlósejtekben a dendritikus sejtekhez viszonyítva. Ez az elrendezés a CB_1 és molekuláris effektorainak magasabb lokális arányához vezet, mely különbség magyarázhatja a periszomatikus axonterminálisok magasabb kannabinoid-érzékenységét. Ezt követően a sejt-specifikus STORM módszert alkalmazva megvizsgáltuk a CB_1 eloszlás átrendeződését kannabinoid tolerancia kialakulása során. A kannabisz pszichoaktív hatásáért felelős THC krónikus alkalmazása az egyedileg jelölt GABAerg interneuronokon a CB_1 receptorok megnövekedett internalizációját, és a receptorok számának csökkenését vonta maga után. A bekövetkezett változás csak meglepően lassan, a viselkedési hatásban mért toleranciánál is később állt helyre. Alacsonyabb dózisú, terápiás alkalmazás szempontjából releváns, és pszichoaktív hatást nem kiváltó krónikus THC kezelés hatására a receptorok átrendeződése jóval kisebb mértékű volt, az endokannabinoidok szintjének akut megemelésének hatására pedig nem volt kimutatható. Ezek az eredmények hozzájárulnak a szinaptikus kannabinoid jelátvitel és a kannabinoid tolerancia molekuláris hátterének pontosabb megismeréséhez.

9. References

Abood ME, Sauss C, Fan F, Tilton CL, Martin BR. (1993) Development of behavioral tolerance to delta 9-thc without alteration of cannabinoid receptor binding or mrna levels in whole brain. Pharmacol Biochem Behav. 46(3):575-579.

Ade KK, Lovinger DM. (2007) Anandamide regulates postnatal development of long-term synaptic plasticity in the rat dorsolateral striatum. J Neurosci. 27(9):2403-2409.

Aguado T, Monory K, Palazuelos J, Stella N, Cravatt B, Lutz B, Marsicano G, Kokaia Z, Guzman M, Galve-Roperh I. (2005) The endocannabinoid system drives neural progenitor proliferation. Faseb J. 19(12):1704-1706.

Ahn K, McKinney MK, Cravatt BF. (2008) Enzymatic pathways that regulate endocannabinoid signaling in the nervous system. Chem Rev. 108(5):1687-1707.

Alger BE. (2012) Endocannabinoids at the synapse a decade after the dies mirabilis (29 march 2001): What we still do not know. J Physiol. 590(Pt 10):2203-2212.

Alger BE, Kim J. (2011) Supply and demand for endocannabinoids. Trends Neurosci. 34(6):304-315.

Ali AB, Todorova M. (2010) Asynchronous release of gaba via tonic cannabinoid receptor activation at identified interneuron synapses in rat ca1. Eur J Neurosci. 31(7):1196-1207.

Allen JR, Ross ST, Davidson MW. (2013) Single molecule localization microscopy for superresolution. Journal of Optics. 15(9):094001.

Andersen P. (2007) The hippocampus book. Oxford University Press, USA: 37-94.

Anderson GR, Aoto J, Tabuchi K, Földy C, Covy J, Yee AX, Wu D, Lee SJ, Chen L, Malenka RC, Südhof TC. (2015) B-neurexins control neural circuits by regulating synaptic endocannabinoid signaling. Cell. 162(3):593-606.

Azad SC, Eder M, Marsicano G, Lutz B, Zieglgansberger W, Rammes G. (2003) Activation of the cannabinoid receptor type 1 decreases glutamatergic and gabaergic synaptic transmission in the lateral amygdala of the mouse. Learn Mem. 10(2):116-128.

Bacci A, Huguenard JR, Prince DA. (2004) Long-lasting self-inhibition of neocortical interneurons mediated by endocannabinoids. Nature. 431(7006):312-316.

Baddeley D, Cannell MB, Soeller C. (2010) Visualization of localization microscopy data. Microsc Microanal. 16(1):64-72.

Barna L, Dudok B, Miczán V, Horváth A, László ZI, Katona I. (2016) Correlated confocal and super-resolution imaging by vividstorm. Nat Protoc. 11(1):163-183.

Bass CE, Martin BR. (2000) Time course for the induction and maintenance of tolerance to delta(9)-tetrahydrocannabinol in mice. Drug Alcohol Depend. 60(2):113-119.

Basu J, Srinivas KV, Cheung SK, Taniguchi H, Huang ZJ, Siegelbaum SA. (2013) A cortico-hippocampal learning rule shapes inhibitory microcircuit activity to enhance hippocampal information flow. Neuron. 79(6):1208-1221.

Basu J, Zaremba JD, Cheung SK, Hitti FL, Zemelman BV, Losonczy A, Siegelbaum SA. (2016) Gating of hippocampal activity, plasticity, and memory by entorhinal cortex long-range inhibition. Science. 351(6269):aaa5694.

Bates M, Dempsey GT, Chen KH, Zhuang X. (2012) Multicolor super-resolution fluorescence imaging via multi-parameter fluorophore detection. Chemphyschem. 13(1):99-107.

Bates M, Huang B, Dempsey GT, Zhuang X. (2007) Multicolor super-resolution imaging with photo-switchable fluorescent probes. Science. 317(5845):1749-1753.

Betzig E, Patterson GH, Sougrat R, Lindwasser OW, Olenych S, Bonifacino JS, Davidson MW, Lippincott-Schwartz J, Hess HF. (2006) Imaging intracellular fluorescent proteins at nanometer resolution. Science. 313(5793):1642-1645.

Bezaire MJ, Soltesz I. (2013) Quantitative assessment of ca1 local circuits: Knowledge base for interneuron-pyramidal cell connectivity. Hippocampus. 23(9):751-785.

Biró AA, Holderith NB, Nusser Z. (2006) Release probability-dependent scaling of the postsynaptic responses at single hippocampal gabaergic synapses. J Neurosci. 26(48):12487-12496.

Bisogno T, Howell F, Williams G, Minassi A, Cascio MG, Ligresti A, Matias I, Schiano-Moriello A, Paul P, Williams EJ, Gangadharan U, Hobbs C, Di Marzo V, Doherty P. (2003) Cloning of the first sn1-dag lipases points to the spatial and temporal regulation of endocannabinoid signaling in the brain. J Cell Biol. 163(3):463-468.

Bodor AL, Katona I, Nyiri G, Mackie K, Ledent C, Hajos N, Freund TF. (2005) Endocannabinoid signaling in rat somatosensory cortex: Laminar differences and involvement of specific interneuron types. J Neurosci. 25(29):6845-6856.

Bolla KI, Brown K, Eldreth D, Tate K, Cadet JL. (2002) Dose-related neurocognitive effects of marijuana use. Neurology. 59(9):1337-1343.

Brenneisen R. (2007) Chemistry and analysis of phytocannabinoids and other cannabis constituents. In: ElSohly MA, editor. Marijuana and the cannabinoids. Totowa, NJ: Humana Press. p. 17-49.

Brown AJ. (2007) Novel cannabinoid receptors. British Journal of Pharmacology. 152(5):567-575.

Bucurenciu I, Kulik A, Schwaller B, Frotscher M, Jonas P. (2008) Nanodomain coupling between ca2+ channels and ca2+ sensors promotes fast and efficient transmitter release at a cortical gabaergic synapse. Neuron. 57(4):536-545.

Busquets-Garcia A, Desprez T, Metna-Laurent M, Bellocchio L, Marsicano G, Soria-Gomez E. (2015) Dissecting the cannabinergic control of behavior: The where matters. Bioessays. 37(11):1215-25.

Busquets-Garcia A, Gomis-González M, Guegan T, Agustín-Pavón C, Pastor A, Mato S, Pérez-Samartín A, Matute C, de la Torre R, Dierssen M, Maldonado R, Ozaita A. (2013) Targeting the endocannabinoid system in the treatment of fragile x syndrome. Nat Med. 19(5):603-607.

Butt SJ, Fuccillo M, Nery S, Noctor S, Kriegstein A, Corbin JG, Fishell G. (2005) The temporal and spatial origins of cortical interneurons predict their physiological subtype. Neuron. 48(4):591-604.

Carlson SS, Valdez G, Sanes JR. (2010) Presynaptic calcium channels and α3-integrins are complexed with synaptic cleft laminins, cytoskeletal elements and active zone components. J Neurochem. 115(3):654-666.

Castillo PE, Younts TJ, Chávez AE, Hashimotodani Y. (2012) Endocannabinoid signaling and synaptic function. Neuron. 76(1):70-81.

Cembrowski MS, Bachman JL, Wang L, Sugino K, Shields BC, Spruston N. (2016) Spatial gene-expression gradients underlie prominent heterogeneity of ca1 pyramidal neurons. Neuron. 89(2):351-368.

Chen K, Neu A, Howard AL, Foldy C, Echegoyen J, Hilgenberg L, Smith M, Mackie K, Soltesz I. (2007) Prevention of plasticity of endocannabinoid signaling inhibits persistent limbic hyperexcitability caused by developmental seizures. J Neurosci. 27(1):46-58.

Chen Z, Das B, Nakamura Y, DiGregorio DA, Young SM. (2015) Ca2+ channel to synaptic vesicle distance accounts for the readily releasable pool kinetics at a functionally mature auditory synapse. J Neurosci. 35(5):2083-2100.

Chevaleyre V, Castillo PE. (2003) Heterosynaptic ltd of hippocampal gabaergic synapses: A novel role of endocannabinoids in regulating excitability. Neuron. 38(3):461-472.

Chevaleyre V, Castillo PE. (2004) Endocannabinoid-mediated metaplasticity in the hippocampus. Neuron. 43(6):871-881.

Chevaleyre V, Heifets BD, Kaeser PS, Sudhof TC, Castillo PE. (2007) Endocannabinoid-mediated long-term plasticity requires camp/pka signaling and rim1alpha. Neuron. 54(5):801-812.

Chhatwal JP, Davis M, Maguschak KA, Ressler KJ. (2005) Enhancing cannabinoid neurotransmission augments the extinction of conditioned fear. Neuropsychopharmacology. 30(3):516-524.

Choquet D, Triller A. (2013) The dynamic synapse. Neuron. 80(3):691-703.

Chávez AE, Chiu CQ, Castillo PE. (2010) Trpv1 activation by endogenous anandamide triggers postsynaptic long-term depression in dentate gyrus. Nat Neurosci. 13(12):1511-1518.

Cope DW, Maccaferri G, Marton LF, Roberts JD, Cobden PM, Somogyi P. (2002) Cholecystokinin-immunopositive basket and schaffer collateral-associated interneurones target different domains of pyramidal cells in the ca1 area of the rat hippocampus. Neuroscience. 109(1):63-80.

Coutts AA, Anavi-Goffer S, Ross RA, MacEwan DJ, Mackie K, Pertwee RG, Irving AJ. (2001) Agonist-induced internalization and trafficking of cannabinoid cb1 receptors in hippocampal neurons. J Neurosci. 21(7):2425-2433.

Cravatt BF, Demarest K, Patricelli MP, Bracey MH, Giang DK, Martin BR, Lichtman AH. (2001) Supersensitivity to anandamide and enhanced endogenous cannabinoid

signaling in mice lacking fatty acid amide hydrolase. Proc Natl Acad Sci USA. 98(16):9371-9376.

Cravatt BF, Giang DK, Mayfield SP, Boger DL, Lerner RA, Gilula NB. (1996) Molecular characterization of an enzyme that degrades neuromodulatory fatty-acid amides. Nature. 384(6604):83-87.

Crozier RA, Wang Y, Liu CH, Bear MF. (2007) Deprivation-induced synaptic depression by distinct mechanisms in different layers of mouse visual cortex. Proc Natl Acad Sci USA. 104(4):1383-1388.

Cui Y, Prokin I, Xu H, Delord B, Genet S, Venance L, Berry H. (2016) Endocannabinoid dynamics gate spike-timing dependent depression and potentiation. Elife. 5:e13185.

Dani A, Huang B, Bergan J, Dulac C, Zhuang X. (2010) Superresolution imaging of chemical synapses in the brain. Neuron. 68(5):843-856.

Daniel H, Rancillac A, Crepel F. (2004) Mechanisms underlying cannabinoid inhibition of presynaptic ca2+ influx at parallel fibre synapses of the rat cerebellum. J Physiol. 557(Pt 1):159-174.

Daumas F, Destainville N, Millot C, Lopez A, Dean D, Salomé L. (2003) Confined diffusion without fences of a g-protein-coupled receptor as revealed by single particle tracking. Biophys J. 84(1):356-366.

Davydova D, Marini C, King C, Klueva J, Bischof F, Romorini S, Montenegro-Venegas C, Heine M, Schneider R, Schröder MS, Altrock WD, Henneberger C, Rusakov DA, Gundelfinger ED, Fejtova A. (2014) Bassoon specifically controls presynaptic p/q-type ca(2+) channels via rim-binding protein. Neuron. 82(1):181-194.

Dempsey GT, Bates M, Kowtoniuk WE, Liu DR, Tsien RY, Zhuang X. (2009) Photoswitching mechanism of cyanine dyes. J Am Chem Soc. 131(51):18192-18193.

Dempsey GT, Vaughan JC, Chen KH, Bates M, Zhuang X. (2011) Evaluation of fluorophores for optimal performance in localization-based super-resolution imaging. Nat Methods. 8(12):1027-1036.

Deshmukh S, Onozuka K, Bender KJ, Bender VA, Lutz B, Mackie K, Feldman DE. (2007) Postnatal development of cannabinoid receptor type 1 expression in rodent somatosensory cortex. Neuroscience. 145(1):279-287.

Devane WA, Dysarz FA, Johnson MR, Melvin LS, Howlett AC. (1988) Determination and characterization of a cannabinoid receptor in rat brain. Mol Pharmacol. 34(5):605-613.

Devane WA, Hanus L, Breuer A, Pertwee RG, Stevenson LA, Griffin G, Gibson D, Mandelbaum A, Etinger A, Mechoulam R. (1992) Isolation and structure of a brain constituent that binds to the cannabinoid receptor. Science. 258(5090):1946-1949.

Dhopeshwarkar A, Mackie K. (2014) Cb2 cannabinoid receptors as a therapeutic target-what does the future hold? Mol Pharmacol. 86(4):430-437.

Di Marzo V, Fontana A, Cadas H, Schinelli S, Cimino G, Schwartz JC, Piomelli D. (1994) Formation and inactivation of endogenous cannabinoid anandamide in central neurons. Nature. 372(6507):686-691.

Di Marzo V, Stella N, Zimmer A. (2015) Endocannabinoid signalling and the deteriorating brain. Nat Rev Neurosci. 16(1):30-42.

Dinh TP, Carpenter D, Leslie FM, Freund TF, Katona I, Sensi SL, Kathuria S, Piomelli D. (2002) Brain monoglyceride lipase participating in endocannabinoid inactivation. Proc Natl Acad Sci USA. 99(16):10819-10824.

Dudok B, Barna L, Ledri M, Szabó SI, Szabadits E, Pintér B, Woodhams SG, Henstridge CM, Balla GY, Nyilas R, Varga C, Lee SH, Matolcsi M, Cervenak J, Kacskovics I, Watanabe M, Sagheddu C, Melis M, Pistis M, Soltesz I, Katona I. (2015) Cell-specific storm super-resolution imaging reveals nanoscale organization of cannabinoid signaling. Nat Neurosci. 18(1):75-86.

Edwards DA, Kim J, Alger BE. (2006) Multiple mechanisms of endocannabinoid response initiation in hippocampus. J Neurophysiol. 95(1):67-75.

Edwards DA, Zhang L, Alger BE. (2008) Metaplastic control of the endocannabinoid system at inhibitory synapses in hippocampus. Proc Natl Acad Sci USA. 105(23):8142-8147.

Egertova M, Simon GM, Cravatt BF, Elphick MR. (2008) Localization of n-acyl phosphatidylethanolamine phospholipase d (nape-pld) expression in mouse brain: A new perspective on n-acylethanolamines as neural signaling molecules. J Comp Neurol. 506(4):604-615.

Eggermann E, Bucurenciu I, Goswami SP, Jonas P. (2012) Nanodomain coupling between ca^{2+} channels and sensors of exocytosis at fast mammalian synapses. Nat Rev Neurosci. 13(1):7-21.

El-Alfy AT, Ivey K, Robinson K, Ahmed S, Radwan M, Slade D, Khan I, ElSohly M, Ross S. (2010) Antidepressant-like effect of delta9-tetrahydrocannabinol and other cannabinoids isolated from cannabis sativa l. Pharmacol Biochem Behav. 95(4):434-442.

Ester M, Kriegel H-P, Sander J, Xu X. (1996) A density-based algorithm for discovering clusters in large spatial databases with noise. Proceedings of the Second International Conference on Knowledge Discovery and Data Mining (KDD-96). p. 226–231.

Fattore L. (2015) Cannabinoids in neurologic and mental disease. Fattore L, editor. London, UK: Academic Press.

Frank T, Rutherford MA, Strenzke N, Neef A, Pangršič T, Khimich D, Fejtova A, Fetjova A, Gundelfinger ED, Liberman MC, Harke B, Bryan KE, Lee A, Egner A, Riedel D, Moser T. (2010) Bassoon and the synaptic ribbon organize $ca^{2}+$ channels and vesicles to add release sites and promote refilling. Neuron. 68(4):724-738.

Freund TF, Buzsaki G. (1996) Interneurons of the hippocampus. Hippocampus. 6(4):347-470.

Freund TF, Katona I. (2007) Perisomatic inhibition. Neuron. 56(1):33-42.

Fu J, Gaetani S, Oveisi F, Lo Verme J, Serrano A, Rodríguez De Fonseca F, Rosengarth A, Luecke H, Di Giacomo B, Tarzia G, Piomelli D. (2003) Oleylethanolamide regulates feeding and body weight through activation of the nuclear receptor pparalpha. Nature. 425(6953):90-93.

Fuccillo MV, Földy C, Gökce Ö, Rothwell PE, Sun GL, Malenka RC, Südhof TC. (2015) Single-cell mrna profiling reveals cell-type-specific expression of neurexin isoforms. Neuron. 87(2):326-340.

Fukudome Y, Ohno-Shosaku T, Matsui M, Omori Y, Fukaya M, Tsubokawa H, Taketo MM, Watanabe M, Manabe T, Kano M. (2004) Two distinct classes of muscarinic action on hippocampal inhibitory synapses: M2-mediated direct suppression and m1/m3-mediated indirect suppression through endocannabinoid signalling. Eur J Neurosci. 19(10):2682-2692.

Földy C, Malenka RC, Südhof TC. (2013) Autism-associated neuroligin-3 mutations commonly disrupt tonic endocannabinoid signaling. Neuron. 78(3):498-509.

Gaffuri AL, Ladarre D, Lenkei Z. (2012) Type-1 cannabinoid receptor signaling in neuronal development. Pharmacology. 90(1-2):19-39.

Gao Y, Vasilyev DV, Goncalves MB, Howell FV, Hobbs C, Reisenberg M, Shen R, Zhang MY, Strassle BW, Lu P, Mark L, Piesla MJ, Deng K, Kouranova EV, Ring RH, Whiteside GT, Bates B, Walsh FS, Williams G, Pangalos MN, Samad TA, Doherty P. (2010) Loss of retrograde endocannabinoid signaling and reduced adult neurogenesis in diacylglycerol lipase knock-out mice. J Neurosci. 30(6):2017-2024.

Gaoni Y, Mechoulam R. (1964) Isolation, structure, and partial synthesis of an active constituent of hashish. Journal of the American Chemical Society. 86(8):1646-1647.

Gelles J, Schnapp BJ, Sheetz MP. (1988) Tracking kinesin-driven movements with nanometre-scale precision. Nature. 331(6155):450-453.

Ghijsen WE, Leenders AG, Lopes da Silva FH. (2003) Regulation of vesicle traffic and neurotransmitter release in isolated nerve terminals. Neurochem Res. 28(10):1443-1452.

Godin AG, Lounis B, Cognet L. (2014) Super-resolution microscopy approaches for live cell imaging. Biophys J. 107(8):1777-1784.

Godlewski G, Offertáler L, Wagner JA, Kunos G. (2009) Receptors for acylethanolamides--gpr55 and gpr119. Prostaglandins Other Lipid Mediat. 89(3-4):105-111.

Grueter BA, Brasnjo G, Malenka RC. (2010) Postsynaptic trpv1 triggers cell type-specific long-term depression in the nucleus accumbens. Nat Neurosci. 13(12):1519-1525.

Gulyas AI, Cravatt BF, Bracey MH, Dinh TP, Piomelli D, Boscia F, Freund TF. (2004) Segregation of two endocannabinoid-hydrolyzing enzymes into pre- and postsynaptic compartments in the rat hippocampus, cerebellum and amygdala. Eur J Neurosci. 20(2):441-458.

Gulyás AI, Miles R, Sík A, Tóth K, Tamamaki N, Freund TF. (1993) Hippocampal pyramidal cells excite inhibitory neurons through a single release site. Nature. 366(6456):683-687.

Gustafsson MG. (2000) Surpassing the lateral resolution limit by a factor of two using structured illumination microscopy. J Microsc. 198(Pt 2):82-87.

Harkany T, Guzmán M, Galve-Roperh I, Berghuis P, Devi LA, Mackie K. (2007) The emerging functions of endocannabinoid signaling during cns development. Trends Pharmacol Sci. 28(2):83-92.

Harkany T, Mackie K, Doherty P. (2008) Wiring and firing neuronal networks: Endocannabinoids take center stage. Curr Opin Neurobiol. 18(3):338-345.

Hashimotodani Y, Ohno-Shosaku T, Tsubokawa H, Ogata H, Emoto K, Maejima T, Araishi K, Shin HS, Kano M. (2005) Phospholipase cbeta serves as a coincidence detector through its ca2+ dependency for triggering retrograde endocannabinoid signal. Neuron. 45(2):257-268.

Hefft S, Jonas P. (2005) Asynchronous gaba release generates long-lasting inhibition at a hippocampal interneuron-principal neuron synapse. Nat Neurosci. 8(10):1319-1328.

Heifets BD, Castillo PE. (2009) Endocannabinoid signaling and long-term synaptic plasticity. Annu Rev Physiol. 71:283-306.

Heifets BD, Chevaleyre V, Castillo PE. (2008) Interneuron activity controls endocannabinoid-mediated presynaptic plasticity through calcineurin. Proc Natl Acad Sci USA. 105(29):10250-10255.

Heilemann M, van de Linde S, Schüttpelz M, Kasper R, Seefeldt B, Mukherjee A, Tinnefeld P, Sauer M. (2008) Subdiffraction-resolution fluorescence imaging with conventional fluorescent probes. Angew Chem Int Ed Engl. 47(33):6172-6176.

Heishman SJ, Huestis MA, Henningfield JE, Cone EJ. (1990) Acute and residual effects of marijuana: Profiles of plasma thc levels, physiological, subjective, and performance measures. Pharmacol Biochem Behav. 37(3):561-565.

Hell SW, Wichmann J. (1994) Breaking the diffraction resolution limit by stimulated emission: Stimulated-emission-depletion fluorescence microscopy. Opt Lett. 19(11):780-782.

Herkenham M, Lynn AB, Johnson MR, Melvin LS, de Costa BR, Rice KC. (1991) Characterization and localization of cannabinoid receptors in rat brain: A quantitative in vitro autoradiographic study. J Neurosci. 11(2):563-583.

Herkenham M, Lynn AB, Little MD, Johnson MR, Melvin LS, de Costa BR, Rice KC. (1990) Cannabinoid receptor localization in brain. Proc Natl Acad Sci USA. 87(5):1932-1936.

Herlitze S, Garcia DE, Mackie K, Hille B, Scheuer T, Catterall WA. (1996) Modulation of ca2+ channels by g-protein beta gamma subunits. Nature. 380(6571):258-262.

Herrick-Davis K, Grinde E, Cowan A, Mazurkiewicz JE. (2013) Fluorescence correlation spectroscopy analysis of serotonin, adrenergic, muscarinic, and dopamine receptor dimerization: The oligomer number puzzle. Mol Pharmacol. 84(4):630-642.

Hess ST, Girirajan TP, Mason MD. (2006) Ultra-high resolution imaging by fluorescence photoactivation localization microscopy. Biophys J. 91(11):4258-4272.

Hirvonen J, Goodwin RS, Li CT, Terry GE, Zoghbi SS, Morse C, Pike VW, Volkow ND, Huestis MA, Innis RB. (2012) Reversible and regionally selective downregulation of brain cannabinoid cb1 receptors in chronic daily cannabis smokers. Mol Psychiatry. 17(6):642-649.

Hoffman AF, Oz M, Caulder T, Lupica CR. (2003) Functional tolerance and blockade of long-term depression at synapses in the nucleus accumbens after chronic cannabinoid exposure. J Neurosci. 23(12):4815-4820.

Hoffman AF, Oz M, Yang R, Lichtman AH, Lupica CR. (2007) Opposing actions of chronic delta9-tetrahydrocannabinol and cannabinoid antagonists on hippocampal long-term potentiation. Learn Mem. 14(1-2):63-74.

Holderith N, Lorincz A, Katona G, Rózsa B, Kulik A, Watanabe M, Nusser Z. (2012) Release probability of hippocampal glutamatergic terminals scales with the size of the active zone. Nat Neurosci. 15(7):988-997.

Howlett AC, Bidaut-Russell M, Devane WA, Melvin LS, Johnson MR, Herkenham M. (1990) The cannabinoid receptor: Biochemical, anatomical and behavioral characterization. Trends Neurosci. 13(10):420-423.

Howlett AC, Blume LC, Dalton GD. (2010) Cb(1) cannabinoid receptors and their associated proteins. Curr Med Chem. 17(14):1382-1393.

Hsieh C, Brown S, Derleth C, Mackie K. (1999) Internalization and recycling of the cb1 cannabinoid receptor. J Neurochem. 73(2):493-501.

Hsu KL, Tsuboi K, Adibekian A, Pugh H, Masuda K, Cravatt BF. (2012) Daglβ inhibition perturbs a lipid network involved in macrophage inflammatory responses. Nat Chem Biol. 8(12):999-1007.

Huang B, Jones SA, Brandenburg B, Zhuang X. (2008a) Whole-cell 3d storm reveals interactions between cellular structures with nanometer-scale resolution. Nat Methods. 5(12):1047-1052.

Huang B, Wang W, Bates M, Zhuang X. (2008b) Three-dimensional super-resolution imaging by stochastic optical reconstruction microscopy. Science. 319(5864):810-813.

Huestis MA. (2007) Human cannabinoid pharmacokinetics. Chem Biodivers. 4(8):1770-1804.

Huestis MA, Gorelick DA, Heishman SJ, Preston KL, Nelson RA, Moolchan ET, Frank RA. (2001) Blockade of effects of smoked marijuana by the cb1-selective cannabinoid receptor antagonist sr141716. Arch Gen Psychiatry. 58(4):322-328.

Jung KM, Astarita G, Zhu C, Wallace M, Mackie K, Piomelli D. (2007) A key role for diacylglycerol lipase-alpha in metabotropic glutamate receptor-dependent endocannabinoid mobilization. Mol Pharmacol. 72(3):612-621.

Jung KM, Mangieri R, Stapleton C, Kim J, Fegley D, Wallace M, Mackie K, Piomelli D. (2005) Stimulation of endocannabinoid formation in brain slice cultures through activation of group i metabotropic glutamate receptors. Mol Pharmacol. 68(5):1196-1202.

Jung KM, Sepers M, Henstridge CM, Lassalle O, Neuhofer D, Martin H, Ginger M, Frick A, DiPatrizio NV, Mackie K, Katona I, Piomelli D, Manzoni OJ. (2012) Uncoupling of the endocannabinoid signalling complex in a mouse model of fragile x syndrome. Nat Commun. 3:1080.

Kano M, Ohno-Shosaku T, Hashimotodani Y, Uchigashima M, Watanabe M. (2009) Endocannabinoid-mediated control of synaptic transmission. Physiol Rev. 89(1):309-380.

Karschner EL, Darwin WD, Goodwin RS, Wright S, Huestis MA. (2011) Plasma cannabinoid pharmacokinetics following controlled oral delta9-tetrahydrocannabinol and oromucosal cannabis extract administration. Clin Chem. 57(1):66-75.

Katona I, Freund TF. (2008) Endocannabinoid signaling as a synaptic circuit breaker in neurological disease. Nat Med. 14(9):923-930.

Katona I, Freund TF. (2012) Multiple functions of endocannabinoid signaling in the brain. Annu Rev Neurosci. 35:529-558.

Katona I, Rancz EA, Acsady L, Ledent C, Mackie K, Hajos N, Freund TF. (2001) Distribution of cb1 cannabinoid receptors in the amygdala and their role in the control of gabaergic transmission. J Neurosci. 21(23):9506-9518.

Katona I, Sperlagh B, Sik A, Kafalvi A, Vizi ES, Mackie K, Freund TF. (1999) Presynaptically located cb1 cannabinoid receptors regulate gaba release from axon terminals of specific hippocampal interneurons. J Neurosci. 19(11):4544-4558.

Katona I, Urban GM, Wallace M, Ledent C, Jung KM, Piomelli D, Mackie K, Freund TF. (2006) Molecular composition of the endocannabinoid system at glutamatergic synapses. J Neurosci. 26(21):5628-5637.

Kawaguchi Y, Kubota Y. (1998) Neurochemical features and synaptic connections of large physiologically-identified gabaergic cells in the rat frontal cortex. Neuroscience. 85(3):677-701.

Kawamura Y, Fukaya M, Maejima T, Yoshida T, Miura E, Watanabe M, Ohno-Shosaku T, Kano M. (2006) The cb1 cannabinoid receptor is the major cannabinoid receptor at excitatory presynaptic sites in the hippocampus and cerebellum. J Neurosci. 26(11):2991-3001.

Kim J, Alger BE. (2010) Reduction in endocannabinoid tone is a homeostatic mechanism for specific inhibitory synapses. Nat Neurosci. 13(5):592-600.

Klausberger T, Marton LF, O'Neill J, Huck JH, Dalezios Y, Fuentealba P, Suen WY, Papp E, Kaneko T, Watanabe M, Csicsvari J, Somogyi P. (2005) Complementary roles of cholecystokinin- and parvalbumin-expressing gabaergic neurons in hippocampal network oscillations. J Neurosci. 25(42):9782-9793.

Klausberger T, Somogyi P. (2008) Neuronal diversity and temporal dynamics: The unity of hippocampal circuit operations. Science. 321(5885):53-57.

Kreitzer AC, Malenka RC. (2007) Endocannabinoid-mediated rescue of striatal ltd and motor deficits in parkinson's disease models. Nature. 445(7128):643-647.

Lakadamyali M, Babcock H, Bates M, Zhuang X, Lichtman J. (2012) 3d multicolor super-resolution imaging offers improved accuracy in neuron tracing. PLoS One. 7(1):e30826.

Lampe A, Haucke V, Sigrist SJ, Heilemann M, Schmoranzer J. (2012) Multi-colour direct storm with red emitting carbocyanines. Biol Cell. 104(4):229-237.

Landmann L. (2002) Deconvolution improves colocalization analysis of multiple fluorochromes in 3d confocal data sets more than filtering techniques. J Microsc. 208(Pt 2):134-147.

Lee SH, Földy C, Soltesz I. (2010a) Distinct endocannabinoid control of gaba release at perisomatic and dendritic synapses in the hippocampus. J Neurosci. 30(23):7993-8000.

Lee S, Hjerling-Leffler J, Zagha E, Fishell G, Rudy B. (2010b) The largest group of superficial neocortical gabaergic interneurons expresses ionotropic serotonin receptors. J Neurosci. 30(50):16796-16808.

Lee SH, Ledri M, Tóth B, Marchionni I, Henstridge CM, Dudok B, Kenesei K, Barna L, Szabó SI, Renkecz T, Oberoi M, Watanabe M, Limoli CL, Horvai G, Soltesz I, Katona I. (2015) Multiple forms of endocannabinoid and endovanilloid signaling regulate the tonic control of gaba release. J Neurosci. 35(27):10039-10057.

Lee SH, Marchionni I, Bezaire M, Varga C, Danielson N, Lovett-Barron M, Losonczy A, Soltesz I. (2014) Parvalbumin-positive basket cells differentiate among hippocampal pyramidal cells. Neuron. 82(5):1129-1144.

Lehmann M, Gottschalk B, Puchkov D, Schmieder P, Schwagerus S, Hackenberger CP, Haucke V, Schmoranzer J. (2015a) Multicolor caged dstorm resolves the ultrastructure of synaptic vesicles in the brain. Angew Chem Int Ed Engl. 54(45):13230-13235.

Lehmann M, Lichtner G, Klenz H, Schmoranzer J. (2015b) Novel organic dyes for multicolor localization-based super-resolution microscopy. J Biophotonics. 9(1-2):161-70.

Lenkey N, Kirizs T, Holderith N, Máté Z, Szabó G, Vizi ES, Hájos N, Nusser Z. (2015) Tonic endocannabinoid-mediated modulation of gaba release is independent of the cb1 content of axon terminals. Nat Commun. 6:6557.

Lerner TN, Kreitzer AC. (2012) Rgs4 is required for dopaminergic control of striatal ltd and susceptibility to parkinsonian motor deficits. Neuron. 73(2):347-359.

Leterrier C, Laine J, Darmon M, Boudin H, Rossier J, Lenkei Z. (2006) Constitutive activation drives compartment-selective endocytosis and axonal targeting of type 1 cannabinoid receptors. J Neurosci. 26(12):3141-3153.

Leung D, Saghatelian A, Simon GM, Cravatt BF. (2006) Inactivation of n-acyl phosphatidylethanolamine phospholipase d reveals multiple mechanisms for the biosynthesis of endocannabinoids. Biochemistry. 45(15):4720-4726.

Li Y, Kim J. (2016) Cb2 cannabinoid receptor knockout in mice impairs contextual long-term memory and enhances spatial working memory. Neural Plast. 2016:9817089.

Lichtman JW, Denk W. (2011) The big and the small: Challenges of imaging the brain's circuits. Science. 334(6056):618-623.

Long LE, Chesworth R, Huang XF, McGregor IS, Arnold JC, Karl T. (2013) Transmembrane domain nrg1 mutant mice show altered susceptibility to the neurobehavioural actions of repeated thc exposure in adolescence. Int J Neuropsychopharmacol. 16(1):163-175.

Losonczy A, Biró AA, Nusser Z. (2004) Persistently active cannabinoid receptors mute a subpopulation of hippocampal interneurons. Proc Natl Acad Sci U S A. 101(5):1362-1367.

Lovinger DM. (2007) Endocannabinoid liberation from neurons in transsynaptic signaling. J Mol Neurosci. 33(1):87-93.

Ludanyi A, Eross L, Czirjak S, Vajda J, Halasz P, Watanabe M, Palkovits M, Magloczky Z, Freund TF, Katona I. (2008) Downregulation of the cb1 cannabinoid receptor and related molecular elements of the endocannabinoid system in epileptic human hippocampus. J Neurosci. 28(12):2976-2990.

Lutz B, Marsicano G, Maldonado R, Hillard CJ. (2015) The endocannabinoid system in guarding against fear, anxiety and stress. Nat Rev Neurosci. 16(12):705-718.

Maccarrone M, Dainese E, Oddi S. (2010) Intracellular trafficking of anandamide: New concepts for signaling. Trends Biochem Sci. 35(11):601-608.

MacGillavry HD, Hoogenraad CC. (2015) The internal architecture of dendritic spines revealed by super-resolution imaging: What did we learn so far? Exp Cell Res. 335(2):180-186.

MacGillavry HD, Song Y, Raghavachari S, Blanpied TA. (2013) Nanoscale scaffolding domains within the postsynaptic density concentrate synaptic ampa receptors. Neuron. 78(4):615-622.

Maglione M, Sigrist SJ. (2013) Seeing the forest tree by tree: Super-resolution light microscopy meets the neurosciences. Nat Neurosci. 16(7):790-797.

Markram H, Toledo-Rodriguez M, Wang Y, Gupta A, Silberberg G, Wu C. (2004) Interneurons of the neocortical inhibitory system. Nat Rev Neurosci. 5(10):793-807.

Maroso M, Szabo GG, Kim HK, Alexander A, Bui AD, Lee SH, Lutz B, Soltesz I. (2016) Cannabinoid control of learning and memory through hcn channels. Neuron. 89(5):1059-1073.

Marsicano G, Lutz B. (1999) Expression of the cannabinoid receptor cb1 in distinct neuronal subpopulations in the adult mouse forebrain. Eur J Neurosci. 11(12):4213-4225.

Marsicano G, Wotjak CT, Azad SC, Bisogno T, Rammes G, Cascio MG, Hermann H, Tang J, Hofmann C, Zieglgansberger W, Di Marzo V, Lutz B. (2002) The endogenous cannabinoid system controls extinction of aversive memories. Nature. 418(6897):530-534.

Matsuda LA, Lolait SJ, Brownstein MJ, Young AC, Bonner TI. (1990) Structure of a cannabinoid receptor and functional expression of the cloned cdna. Nature. 346(6284):561-564.

McDonald NA, Henstridge CM, Connolly CN, Irving AJ. (2007) An essential role for constitutive endocytosis, but not activity, in the axonal targeting of the cb1 cannabinoid receptor. Mol Pharmacol. 71(4):976-984.

Mechoulam R, Ben-Shabat S, Hanus L, Ligumsky M, Kaminski NE, Schatz AR, Gopher A, Almog S, Martin BR, Compton DR, Pertwee RG, Griffin G, Bayewitch M, Barg J, Vogel Z. (1995) Identification of an endogenous 2-monoglyceride, present in canine gut, that binds to cannabinoid receptors. Biochem Pharmacol. 50(1):83-90.

Mechoulam R, Shani A, Edery H, Grunfeld Y. (1970) Chemical basis of hashish activity. Science. 169(3945):611-612.

Melis M, Pillolla G, Luchicchi A, Muntoni AL, Yasar S, Goldberg SR, Pistis M. (2008) Endogenous fatty acid ethanolamides suppress nicotine-induced activation of mesolimbic dopamine neurons through nuclear receptors. J Neurosci. 28(51):13985-13994.

Mikasova L, Groc L, Choquet D, Manzoni OJ. (2008) Altered surface trafficking of presynaptic cannabinoid type 1 receptor in and out synaptic terminals parallels receptor desensitization. Proc Natl Acad Sci USA. 105(47):18596-18601.

Min J, Holden SJ, Carlini L, Unser M, Manley S, Ye JC. (2014) 3d high-density localization microscopy using hybrid astigmatic/ biplane imaging and sparse image reconstruction. Biomed Opt Express. 5(11):3935--3948.

Min R, Di Marzo V, Mansvelder HD. (2010) Dag lipase involvement in depolarization-induced suppression of inhibition: Does endocannabinoid biosynthesis always meet the demand? Neuroscientist. 16(6):608-613.

Min R, Nevian T. (2012) Astrocyte signaling controls spike timing-dependent depression at neocortical synapses. Nat Neurosci. 15(5):746-753.

Mizuseki K, Diba K, Pastalkova E, Buzsáki G. (2011) Hippocampal ca1 pyramidal cells form functionally distinct sublayers. Nat Neurosci. 14(9):1174-1181.

Monory K, Blaudzun H, Massa F, Kaiser N, Lemberger T, Schutz G, Wotjak CT, Lutz B, Marsicano G. (2007) Genetic dissection of behavioural and autonomic effects of delta(9)-tetrahydrocannabinol in mice. PLoS Biol. 5(10):e269.

Monory K, Polack M, Remus A, Lutz B, Korte M. (2015) Cannabinoid cb1 receptor calibrates excitatory synaptic balance in the mouse hippocampus. J Neurosci. 35(9):3842-3850.

Moore CA, Milano SK, Benovic JL. (2007) Regulation of receptor trafficking by grks and arrestins. Annu Rev Physiol. 69:451-482.

More SV, Choi DK. (2015) Promising cannabinoid-based therapies for parkinson's disease: Motor symptoms to neuroprotection. Mol Neurodegener. 10:17.

Mortensen K, Larsson LI. (2001) Quantitative and qualitative immunofluorescence studies of neoplastic cells transfected with a construct encoding p53-egfp. J Histochem Cytochem. 49(11):1363-1367.

Moser EI, Kropff E, Moser MB. (2008) Place cells, grid cells, and the brain's spatial representation system. Annu Rev Neurosci. 31:69-89.

Munro S, Thomas KL, Abu-Shaar M. (1993) Molecular characterization of a peripheral receptor for cannabinoids. Nature. 365(6441):61-65.

Nair D, Hosy E, Petersen JD, Constals A, Giannone G, Choquet D, Sibarita JB. (2013) Super-resolution imaging reveals that ampa receptors inside synapses are dynamically organized in nanodomains regulated by psd95. J Neurosci. 33(32):13204-13224.

Neu A, Földy C, Soltesz I. (2007) Postsynaptic origin of cb1-dependent tonic inhibition of gaba release at cholecystokinin-positive basket cell to pyramidal cell synapses in the ca1 region of the rat hippocampus. J Physiol. 578(Pt 1):233-247.

Nicolussi S, Gertsch J. (2015) Endocannabinoid transport revisited. Vitam Horm. 98:441-485.

Niehaus JL, Liu Y, Wallis KT, Egertova M, Bhartur SG, Mukhopadhyay S, Shi S, He H, Selley DE, Howlett AC, Elphick MR, Lewis DL. (2007) Cb1 cannabinoid receptor activity is modulated by the cannabinoid receptor interacting protein crip 1a. Mol Pharmacol. 72(6):1557-1566.

Nieuwenhuizen RP, Lidke KA, Bates M, Puig DL, Grünwald D, Stallinga S, Rieger B. (2013) Measuring image resolution in optical nanoscopy. Nat Methods. 10(6):557-562.

Nishimune H, Numata T, Chen J, Aoki Y, Wang Y, Starr MP, Mori Y, Stanford JA. (2012) Active zone protein bassoon co-localizes with presynaptic calcium channel, modifies channel function, and recovers from aging related loss by exercise. PLoS One. 7(6):e38029.

Nyilas R, Dudok B, Urban GM, Mackie K, Watanabe M, Cravatt BF, Freund TF, Katona I. (2008) Enzymatic machinery for endocannabinoid biosynthesis associated with calcium stores in glutamatergic axon terminals. J Neurosci. 28(5):1058-1063.

Nyiri G, Cserep C, Szabadits E, Mackie K, Freund TF. (2005) Cb1 cannabinoid receptors are enriched in the perisynaptic annulus and on preterminal segments of hippocampal gabaergic axons. Neuroscience. 136(3):811-822.

O'Keefe J, Dostrovsky J. (1971) The hippocampus as a spatial map. Preliminary evidence from unit activity in the freely-moving rat. Brain Res. 34(1):171-175.

O'Rourke NA, Weiler NC, Micheva KD, Smith SJ. (2012) Deep molecular diversity of mammalian synapses: Why it matters and how to measure it. Nat Rev Neurosci. 13(6):365-379.

Oddone A, Vilanova IV, Tam J, Lakadamyali M. (2014) Super-resolution imaging with stochastic single-molecule localization: Concepts, technical developments, and biological applications. Microsc Res Tech. 77(7):502-509.

Ohno-Shosaku T, Maejima T, Kano M. (2001) Endogenous cannabinoids mediate retrograde signals from depolarized postsynaptic neurons to presynaptic terminals. Neuron. 29(3):729-738.

Okamoto Y, Morishita J, Tsuboi K, Tonai T, Ueda N. (2004) Molecular characterization of a phospholipase d generating anandamide and its congeners. J Biol Chem. 279(7):5298-5305.

Okamoto Y, Wang J, Morishita J, Ueda N. (2007) Biosynthetic pathways of the endocannabinoid anandamide. Chem Biodivers. 4(8):1842-1857.

Oviedo A, Glowa J, Herkenham M. (1993) Chronic cannabinoid administration alters cannabinoid receptor binding in rat brain: A quantitative autoradiographic study. Brain Res. 616(1-2):293-302.

Pacher P, Batkai S, Kunos G. (2006) The endocannabinoid system as an emerging target of pharmacotherapy. Pharmacol Rev. 58(3):389-462.

Pan B, Wang W, Zhong P, Blankman JL, Cravatt BF, Liu QS. (2011) Alterations of endocannabinoid signaling, synaptic plasticity, learning, and memory in monoacylglycerol lipase knock-out mice. J Neurosci. 31(38):13420-13430.

Parsons LH, Hurd YL. (2015) Endocannabinoid signalling in reward and addiction. Nat Rev Neurosci. 16(10):579-594.

Pawelzik H, Hughes DI, Thomson AM. (2002) Physiological and morphological diversity of immunocytochemically defined parvalbumin- and cholecystokinin-positive interneurones in ca1 of the adult rat hippocampus. J Comp Neurol. 443(4):346-367.

Pitler TA, Alger BE. (1992) Postsynaptic spike firing reduces synaptic gabaa responses in hippocampal pyramidal cells. J Neurosci. 12(10):4122-4132.

Puente N, Cui Y, Lassalle O, Lafourcade M, Georges F, Venance L, Grandes P, Manzoni OJ. (2011) Polymodal activation of the endocannabinoid system in the extended amygdala. Nat Neurosci. 14(12):1542-1547.

Puighermanal E, Marsicano G, Busquets-Garcia A, Lutz B, Maldonado R, Ozaita A. (2009) Cannabinoid modulation of hippocampal long-term memory is mediated by mtor signaling. Nat Neurosci. 12(9):1152-1158.

Rahman IA, Tsuboi K, Uyama T, Ueda N. (2014) New players in the fatty acyl ethanolamide metabolism. Pharmacol Res. 86:1-10.

Ramikie TS, Nyilas R, Bluett RJ, Gamble-George JC, Hartley ND, Mackie K, Watanabe M, Katona I, Patel S. (2014) Multiple mechanistically distinct modes of endocannabinoid mobilization at central amygdala glutamatergic synapses. Neuron. 81(5):1111-1125.

Reguero L, Puente N, Elezgarai I, Ramos-Uriarte A, Gerrikagoitia I, Bueno-López JL, Doñate F, Grandes P. (2014) Subcellular localization of nape-pld and dagl-α in the ventromedial nucleus of the hypothalamus by a preembedding immunogold method. Histochem Cell Biol. 141(5):543-550.

Requejo-Isidro J. (2013) Fluorescence nanoscopy. Methods and applications. J Chem Biol. 6(3):97-120.

Richter K, Langnaese K, Kreutz MR, Olias G, Zhai R, Scheich H, Garner CC, Gundelfinger ED. (1999) Presynaptic cytomatrix protein bassoon is localized at both excitatory and inhibitory synapses of rat brain. J Comp Neurol. 408(3):437-448.

Rivera P, Arrabal S, Vargas A, Blanco E, Serrano A, Pavón FJ, Rodríguez de Fonseca F, Suárez J. (2014) Localization of peroxisome proliferator-activated receptor alpha (pparα) and n-acyl phosphatidylethanolamine phospholipase d (nape-pld) in cells expressing the ca(2+)-binding proteins calbindin, calretinin, and parvalbumin in the adult rat hippocampus. Front Neuroanat. 8:12.

Roux L, Buzsáki G. (2015) Tasks for inhibitory interneurons in intact brain circuits. Neuropharmacology. 88:10-23.

Rudy B, Fishell G, Lee S, Hjerling-Leffler J. (2011) Three groups of interneurons account for nearly 100% of neocortical gabaergic neurons. Dev Neurobiol. 71(1):45-61.

Rust MJ, Bates M, Zhuang X. (2006) Sub-diffraction-limit imaging by stochastic optical reconstruction microscopy (storm). Nat Methods. 3(10):793-795.

Schlosburg JE, Blankman JL, Long JZ, Nomura DK, Pan B, Kinsey SG, Nguyen PT, Ramesh D, Booker L, Burston JJ, Thomas EA, Selley DE, Sim-Selley LJ, Liu QS, Lichtman AH, Cravatt BF. (2010) Chronic monoacylglycerol lipase blockade causes functional antagonism of the endocannabinoid system. Nat Neurosci. 13(9):1113-1119.

Schmid HH, Schmid PC, Berdyshev EV. (2002) Cell signaling by endocannabinoids and their congeners: Questions of selectivity and other challenges. Chem Phys Lipids. 121(1-2):111-134.

Schneider R, Hosy E, Kohl J, Klueva J, Choquet D, Thomas U, Voigt A, Heine M. (2015) Mobility of calcium channels in the presynaptic membrane. Neuron. 86(3):672-679.

Shroff H, Galbraith CG, Galbraith JA, Betzig E. (2008) Live-cell photoactivated localization microscopy of nanoscale adhesion dynamics. Nat Methods. 5(5):417-423.

Sigal YM, Speer CM, Babcock HP, Zhuang X. (2015) Mapping synaptic input fields of neurons with super-resolution imaging. Cell. 163(2):493-505.

Smith TH, Blume LC, Straiker A, Cox JO, David BG, McVoy JR, Sayers KW, Poklis JL, Abdullah RA, Egertová M, Chen CK, Mackie K, Elphick MR, Howlett AC, Selley DE. (2015) Cannabinoid receptor-interacting protein 1a modulates cb1 receptor signaling and regulation. Mol Pharmacol. 87(4):747-765.

Soltesz I, Alger BE, Kano M, Lee SH, Lovinger DM, Ohno-Shosaku T, Watanabe M. (2015) Weeding out bad waves: Towards selective cannabinoid circuit control in epilepsy. Nat Rev Neurosci. 16(5):264-277.

Somogyi J, Baude A, Omori Y, Shimizu H, El Mestikawy S, Fukaya M, Shigemoto R, Watanabe M, Somogyi P. (2004) Gabaergic basket cells expressing cholecystokinin contain vesicular glutamate transporter type 3 (vglut3) in their synaptic terminals in hippocampus and isocortex of the rat. Eur J Neurosci. 19(3):552-569.

Somogyi P, Klausberger T. (2005) Defined types of cortical interneurone structure space and spike timing in the hippocampus. J Physiol. 562(Pt 1):9-26.

Specht CG, Izeddin I, Rodriguez PC, El Beheiry M, Rostaing P, Darzacq X, Dahan M, Triller A. (2013) Quantitative nanoscopy of inhibitory synapses: Counting gephyrin molecules and receptor binding sites. Neuron. 79(2):308-321.

Squire LR. (2009) The legacy of patient h.M. For neuroscience. Neuron. 61(1):6-9.

Steindel F, Lerner R, Häring M, Ruehle S, Marsicano G, Lutz B, Monory K. (2013) Neuron-type specific cannabinoid-mediated g protein signalling in mouse hippocampus. J Neurochem. 124(6):795-807.

Stempel AV, Stumpf A, Zhang HY, Özdoğan T, Pannasch U, Theis AK, Otte DM, Wojtalla A, Rácz I, Ponomarenko A, Xi ZX, Zimmer A, Schmitz D. (2016) Cannabinoid type 2 receptors mediate a cell type-specific plasticity in the hippocampus. Neuron. 90(4):795-809.

Stott CG, White L, Wright S, Wilbraham D, Guy GW. (2013) A phase i study to assess the single and multiple dose pharmacokinetics of thc/cbd oromucosal spray. Eur J Clin Pharmacol. 69(5):1135-1147.

Sudhof TC, Malenka RC. (2008) Understanding synapses: Past, present, and future. Neuron. 60(3):469-476.

Sugaya Y, Yamazaki M, Uchigashima M, Kobayashi K, Watanabe M, Sakimura K, Kano M. (2016) Crucial roles of the endocannabinoid 2-arachidonoylglycerol in the suppression of epileptic seizures. Cell Rep. 16(5):1405-1415.

Sugiura T, Kondo S, Sukagawa A, Nakane S, Shinoda A, Itoh K, Yamashita A, Waku K. (1995) 2-arachidonoylglycerol: A possible endogenous cannabinoid receptor ligand in brain. Biochem Biophys Res Commun. 215(1):89-97.

Suplita RL, Eisenstein SA, Neely MH, Moise AM, Hohmann AG. (2008) Cross-sensitization and cross-tolerance between exogenous cannabinoid antinociception and endocannabinoid-mediated stress-induced analgesia. Neuropharmacology. 54(1):161-171.

Szabó GG, Lenkey N, Holderith N, Andrási T, Nusser Z, Hájos N. (2014) Presynaptic calcium channel inhibition underlies cb1 cannabinoid receptor-mediated suppression of gaba release. J Neurosci. 34(23):7958-7963.

Südhof TC. (2008) Neuroligins and neurexins link synaptic function to cognitive disease. Nature. 455(7215):903-911.

Südhof TC. (2012) The presynaptic active zone. Neuron. 75(1):11-25.

Takács VT, Szőnyi A, Freund TF, Nyiri G, Gulyás AI. (2014) Quantitative ultrastructural analysis of basket and axo-axonic cell terminals in the mouse hippocampus. Brain Struct Funct. 220(2):919-40.

Tam J, Merino D. (2015) Storm in comparison with sted and other imaging methods. J Neurochem. 135(4):643-58.

Tanaka J, Matsuzaki M, Tarusawa E, Momiyama A, Molnar E, Kasai H, Shigemoto R. (2005) Number and density of ampa receptors in single synapses in immature cerebellum. J Neurosci. 25(4):799-807.

Tang AH, Chen H, Li TP, Metzbower SR, MacGillavry HD, Blanpied TA. (2016) A trans-synaptic nanocolumn aligns neurotransmitter release to receptors. Nature. 536(7615):210-4.

Tanimura A, Yamazaki M, Hashimotodani Y, Uchigashima M, Kawata S, Abe M, Kita Y, Hashimoto K, Shimizu T, Watanabe M, Sakimura K, Kano M. (2010) The endocannabinoid 2-arachidonoylglycerol produced by diacylglycerol lipase alpha mediates retrograde suppression of synaptic transmission. Neuron. 65(3):320-327.

Tappe-Theodor A, Agarwal N, Katona I, Rubino T, Martini L, Swiercz J, Mackie K, Monyer H, Parolaro D, Whistler J, Kuner T, Kuner R. (2007) A molecular basis of analgesic tolerance to cannabinoids. J Neurosci. 27(15):4165-4177.

Taschler U, Radner FP, Heier C, Schreiber R, Schweiger M, Schoiswohl G, Preiss-Landl K, Jaeger D, Reiter B, Koefeler HC, Wojciechowski J, Theussl C, Penninger JM, Lass A, Haemmerle G, Zechner R, Zimmermann R. (2011) Monoglyceride lipase deficiency in mice impairs lipolysis and attenuates diet-induced insulin resistance. J Biol Chem. 286(20):17467-17477.

Tasic B, Menon V, Nguyen TN, Kim TK, Jarsky T, Yao Z, Levi B, Gray LT, Sorensen SA, Dolbeare T, Bertagnolli D, Goldy J, Shapovalova N, Parry S, Lee C, Smith K, Bernard A, Madisen L, Sunkin SM, Hawrylycz M, Koch C, Zeng H. (2016) Adult mouse cortical cell taxonomy revealed by single cell transcriptomics. Nat Neurosci. 19(2):335-346.

Telley L, Govindan S, Prados J, Stevant I, Nef S, Dermitzakis E, Dayer A, Jabaudon D. (2016) Sequential transcriptional waves direct the differentiation of newborn neurons in the mouse neocortex. Science. 351(6280):1443-1446.

Thibault K, Carrel D, Bonnard D, Gallatz K, Simon A, Biard M, Pezet S, Palkovits M, Lenkei Z. (2013) Activation-dependent subcellular distribution patterns of cb1 cannabinoid receptors in the rat forebrain. Cereb Cortex. 23(11):2581-2591.

Thompson RE, Larson DR, Webb WW. (2002) Precise nanometer localization analysis for individual fluorescent probes. Biophys J. 82(5):2775-2783.

tom Dieck S, Sanmartí-Vila L, Langnaese K, Richter K, Kindler S, Soyke A, Wex H, Smalla KH, Kämpf U, Fränzer JT, Stumm M, Garner CC, Gundelfinger ED. (1998) Bassoon, a novel zinc-finger cag/glutamine-repeat protein selectively localized at the active zone of presynaptic nerve terminals. J Cell Biol. 142(2):499-509.

Tsou K, Mackie K, Sanudo-Pena MC, Walker JM. (1999) Cannabinoid cb1 receptors are localized primarily on cholecystokinin-containing gabaergic interneurons in the rat hippocampal formation. Neuroscience. 93(3):969-975.

Tønnesen J, Nägerl UV. (2013) Superresolution imaging for neuroscience. Exp Neurol. 242:33-40.

Uchigashima M, Narushima M, Fukaya M, Katona I, Kano M, Watanabe M. (2007) Subcellular arrangement of molecules for 2-arachidonoyl-glycerol-mediated retrograde signaling and its physiological contribution to synaptic modulation in the striatum. J Neurosci. 27(14):3663-3676.

Uchigashima M, Yamazaki M, Yamasaki M, Tanimura A, Sakimura K, Kano M, Watanabe M. (2011) Molecular and morphological configuration for 2-arachidonoylglycerol-mediated retrograde signaling at mossy cell-granule cell synapses in the dentate gyrus. J Neurosci. 31(21):7700-7714.

Ueda N, Tsuboi K, Uyama T. (2013) Metabolism of endocannabinoids and related n-acylethanolamines: Canonical and alternative pathways. FEBS J. 280(9):1874-1894.

van de Linde S, Löschberger A, Klein T, Heidbreder M, Wolter S, Heilemann M, Sauer M. (2011) Direct stochastic optical reconstruction microscopy with standard fluorescent probes. Nat Protoc. 6(7):991-1009.

van der Stelt M, Trevisani M, Vellani V, De Petrocellis L, Schiano Moriello A, Campi B, McNaughton P, Geppetti P, Di Marzo V. (2005) Anandamide acts as an intracellular messenger amplifying ca2+ influx via trpv1 channels. Embo J. 24(17):3026-3037.

van Strien NM, Cappaert NL, Witter MP. (2009) The anatomy of memory: An interactive overview of the parahippocampal-hippocampal network. Nat Rev Neurosci. 10(4):272-282.

Varvel SA, Bridgen DT, Tao Q, Thomas BF, Martin BR, Lichtman AH. (2005) Delta9-tetrahydrocannbinol accounts for the antinociceptive, hypothermic, and cataleptic effects of marijuana in mice. J Pharmacol Exp Ther. 314(1):329-337.

Verdaasdonk JS, Lawrimore J, Bloom K. (2014) Determining absolute protein numbers by quantitative fluorescence microscopy. Methods Cell Biol. 123:347-365.

Volk DW, Lewis DA. (2015) The role of endocannabinoid signaling in cortical inhibitory neuron dysfunction in schizophrenia. Biol Psychiatry. 79(7):595-603.

Volkow ND, Baler RD, Compton WM, Weiss SR. (2014) Adverse health effects of marijuana use. N Engl J Med. 370(23):2219-2227.

Wijetunge LS, Angibaud J, Frick A, Kind PC, Nägerl UV. (2014) Stimulated emission depletion (sted) microscopy reveals nanoscale defects in the developmental trajectory of dendritic spine morphogenesis in a mouse model of fragile x syndrome. J Neurosci. 34(18):6405-6412.

Wilhelm BG, Mandad S, Truckenbrodt S, Kröhnert K, Schäfer C, Rammner B, Koo SJ, Claßen GA, Krauss M, Haucke V, Urlaub H, Rizzoli SO. (2014) Composition of isolated synaptic boutons reveals the amounts of vesicle trafficking proteins. Science. 344(6187):1023-1028.

Williams EJ, Walsh FS, Doherty P. (2003) The fgf receptor uses the endocannabinoid signaling system to couple to an axonal growth response. J Cell Biol. 160(4):481-486.

Wilson RI, Kunos G, Nicoll RA. (2001) Presynaptic specificity of endocannabinoid signaling in the hippocampus. Neuron. 31(3):453-462.

Wilson RI, Nicoll RA. (2001) Endogenous cannabinoids mediate retrograde signalling at hippocampal synapses. Nature. 410(6828):588-592.

Wonders CP, Anderson SA. (2006) The origin and specification of cortical interneurons. Nature reviews Neuroscience. 7(9):687-696.

Xu K, Zhong G, Zhuang X. (2013) Actin, spectrin, and associated proteins form a periodic cytoskeletal structure in axons. Science. 339(6118):452-456.

Yamanaka M, Smith NI, Fujita K. (2014) Introduction to super-resolution microscopy. Microscopy (Oxf). 63(3):177-192.

Zeisel A, Muñoz-Manchado AB, Codeluppi S, Lönnerberg P, La Manno G, Juréus A, Marques S, Munguba H, He L, Betsholtz C, Rolny C, Castelo-Branco G, Hjerling-Leffler J, Linnarsson S. (2015) Brain structure. Cell types in the mouse cortex and hippocampus revealed by single-cell rna-seq. Science. 347(6226):1138-1142.

Zhang L, Wang M, Bisogno T, Di Marzo V, Alger BE. (2011) Endocannabinoids generated by ca2+ or by metabotropic glutamate receptors appear to arise from different pools of diacylglycerol lipase. PLoS One. 6(1):e16305.

Zhang Z, Kenny SJ, Hauser M, Li W, Xu K. (2015) Ultrahigh-throughput single-molecule spectroscopy and spectrally resolved super-resolution microscopy. Nat Methods. 12(10):935-938.

Zimmer A, Zimmer AM, Hohmann AG, Herkenham M, Bonner TI. (1999) Increased mortality, hypoactivity, and hypoalgesia in cannabinoid cb1 receptor knockout mice. Proc Natl Acad Sci USA. 96(10):5780-5785.

DOI:10.14753/SE.2017.1972

10. List of publications

Publications related to this thesis

Dudok B[1], Barna L[1], Ledri M[1], Szabó SZI, Szabadits E, Pintér B, Woodhams SG, Henstridge CM, Balla GY, Nyilas R, Varga C, Lee SH, Matolcsi M, Cervenak J, Kacskovics I, Watanabe M, Shaggedu C, Melis M, Pistis M, Soltesz I, Katona I (2015) *Cell type-specific STORM super-resolution imaging reveals nanoscale organization of cannabinoid signalling at hippocampal GABAergic synapses.* **Nature Neuroscience** 18:75-86.

Lee SH, Ledri M, Tóth B, Marchionni I, Henstridge CM, Dudok B, Kenesei K, Barna L, Szabó SZI, Renkecz T, Oberoi MK, Watanabe M, Limoli C, Horvai G, Soltesz I, Katona I (2015) *Multiple Forms of Endocannabinoid and Endovanilloid Signaling Regulate the Tonic Control of GABA Release*. **Jornal of Neuroscience** 35:10039-10057.

Other publications

Barna L[1], Dudok B[1], Miczán V, Horváth A, László ZSI, Katona I (2016) *Correlated confocal and super-resolution imaging by VividSTORM.* **Nature Protocols** 11:163-183.

Neuhofer D, Henstridge CM, Dudok B, Sepers M, Lassalle O, Katona I, Manzoni OJJ (2015) *Functional and structural deficits at accumbens synapses in a mouse model of Fragile X.* **Frontiers in Cellular Neuroscience** 9:100.

Nyilas R, Dudok B, Urbán GM, Mackie K, Watanabe M, Cravatt BF, Freund TF, Katona I (2008) *Enzymatic machinery for endocannabinoid biosynthesis associated with calcium stores in glutamatergic axon terminals.* **Journal of Neuroscience** 28:1058-1063.

[1]equal contribution

DOI:10.14753/SE.2017.1972

11. Acknowledgements

I'm most grateful to István Katona, who has been not only my supervisor and PI, but also my true mentor. Through his enthusiasm, scientific insight, and personal integrity, he taught me technically and conceptually how to conduct research, and also showed me the model of a scientist, and a decent person. I thank him for all the marine mammal species I've ever seen, and I wish him many more birds. I also thank the present and past members of the Laboratory of Molecular Neurobiology, for being an inspiring and productive community through all the many years of my training. I feel fortunate that I had the opportunity to be part of this group, and of KOKI in general. I will miss them, and I sincerely hope they will find a less grumpy replacement for me.

I'm thankful to all the scientists who contributed to the research that provided the basis of this thesis, providing essential reagents, samples and data, but also invaluable and motivating help, advice and feedback. I'm especially grateful to László Barna, for being a wonderful friend and an expert colleague, without him introducing me into microscopy and programing, and without sharing lunch and cocktails, I would've definitely failed in this project.

I would like to thank my parents, my sister, and my friends for being part of my life and making me myself (for better or worse), for keeping me going through hard times, and for the joy of the rare occasions we still met during my PhD. Maybe soon I will have a bit more time. I dedicate this thesis to Péter Gerőcs, to return the favor.

Finally, I'm filled with gratitude and love for my wife, Szandi, who has not only been my best friend and soul mate throughout the years of the research, but also the major motivating force to finalize this thesis.